



Vrije  
Universiteit  
Brussel

# MODELING, CONTROL DESIGN AND TECHNICAL GRID ANALYSIS OF V2G AND G2V SYSTEMS

---

**MARÍA GARCÉS QUÍLEZ**

Master thesis submitted under the supervision of  
Prof. Dr. Ir. Joeri Van Mierlo

The co-supervision of  
Dr. Ir. Omar Hegazy

Academic year  
2015-2016

In order to be awarded the Master's Degree in  
Electromechanical Engineering

## Acknowledgments

First and foremost, I would like to begin expressing my gratitude to my promotors, Prof. Joeri Van Mierlo and Dr. Omar Hegazy, for providing me with the chance to work on this thesis, for the time and guidance that they have offered me throughout these months. In addition, I would like to thank all the members in the ETEC department of the VUB for their welcoming treatment.

To all the professors that I have met during these six years, for all the knowledge and advice they have given me, for helping me become an engineer, and to the Public University of Navarra for making it possible.

I would also like to express my gratitude to the Erasmus+ Programme, which has been the most enriching experience of my life.

Finally, a special thanks to the Van Orley Student House and their international students, the place I have called home during my time in Belgium. Thank you to Joseba, Gabri, Bea, Maca, Alba, Edurne and Eli, my special family in this special period of my life. Moreover, I would like to express my gratitude to my parents, brother, boyfriend and friends, who have always supported me and have shown their love and encouragement despite the distance.

María Garcés Quílez

Brussels, June 2016

# Abstract

The integration of renewable energies as power generators in the electricity grid is necessary to overcome the dependence and pollution linked to fossil fuels. Nevertheless, the variability of these renewable resources limits their quantity in the system. In addition, there exists a trend to change the transport sector by means of the electrification of the existing conventional vehicles based on internal combustion engine (ICE).

A solution to mitigate the mentioned variability and to enable a higher integration is the use of energy storage systems, such as batteries and supercapacitors (SCs). Nonetheless, batteries are nowadays very expensive, so using them only for this back-up function is unviable. Electric Vehicles' batteries could be used for this purpose and be consequently repaid sooner. In order to provide this support service, the chargers of the electric vehicles (EVs) should work with a bidirectional power flow, in two modes: as dynamic loads, when they are charging, which corresponds to Grid-to-Vehicle (G2V) mode; or as generators, when they are discharging, which corresponds to Vehicle-to-Grid (V2G) or Vehicle-to-Home (V2H) modes. Even if this first mode is broadly deployed, the V2G and V2H modes are still in developing process and they are not commercialized yet.

This thesis is mainly focused on designing, modeling and simulating two different chargers that connect a battery pack to either a single-phase grid for low power applications or to a three-phase grid for high power applications, in which both G2V and V2G/V2H modes are implemented. An assessment of the most typical AC/DC and DC/DC converters' topologies is carried out, and their benefits and drawbacks are highlighted. Different control strategies are employed and tested, and a harmonics study of the grid current and voltage is performed.

# Nomenclature

<b><u>Symbol</u></b>	<b><u>Description</u></b>	<b><u>Unit</u></b>
$\alpha_1, \alpha_2, \alpha_3$	Duty cycle of the 3-phase Full Bridge	
$\Delta I$	Current ripple	A
$\Delta V$	Voltage ripple	V
$C_{bus}$	DC-Bus capacitor	F
$C_{bat}$	Battery side capacitor	F
$C_{cell}$	Capacity of a battery cell	Ah
$C_r$	Capacitor of a resonant converter	F
$C_{r,p}$	Parallel capacitor of a resonant converter	F
$C_{r,s}$	Series capacitor of a resonant converter	F
$\zeta$	Damping ratio of a Second Order system	
$\delta$	Magnitude control's variable for the grid current DQ control	
$D, d$	Duty cycle of the DC/DC converter	
$D_i$	Diode number i	
$E_{Doff}$	Energy loss in the switch-off of a diode	J
$E_{Ton}$	Energy loss in the switch-on of a transistor	J
$E_{Toff}$	Energy loss in the switch-off of a transistor	J
$f_1, f_2, f_3$	Control signals of the 3-Phase Full Bridge	
$F$	Switching orders of the 1-Phase Full Bridge	
$f_c$	Commutation frequency of the converters	Hz
$f_{grid}$	Grid's frequency	Hz
$f_{sam}$	Sampling frequency of the digital control	Hz
$f_{si}$	Frequency of the current sensor	Hz
$f_{sv}$	Frequency of the voltage sensor	Hz
$i_m$	Average grid's phase current	A
$I_{bat}$	Battery current	A
$I_{Cbat}$	Battery side capacitor's current	A
$I_{DC}$	DC current, in the Battery side	A
$I_d, I_q$	DQ Grid currents	A
$I_{grid}$	Grid current	A
$I_{Lbat}$	Battery side inductor's current	A
$I_r, I_s, I_t$	Grid's phase currents for 3-Phase systems	A
$K_i$	Integral constant of the PI and PR controllers	
$K_p$	Proportional constant of the PI and PR controllers	
$K_{si}$	Sensing constant of the current sensor	
$K_{sv}$	Sensing constant of the voltage sensor	
$L_{bat}$	Battery side inductor	H
$L_{grid}$	Grid side inductor	H
$L_r$	Inductor of a resonant converter	H
$M_{max}$	Maximum modulation index of the Full Bridge	%
$N_p$	Number of strings in parallel in the battery	
$N_s$	Number of cells in series in each string of the battery	

$\pi$	Pi constant	
$\Phi_m$	Phase control's variable for the grid current DQ control	
$P_{AC}$	AC power, in the grid side	W
$P_{bat}$	Power of the battery	W
$P_{DC}$	DC power, in the DC-Bus side	W
$P_{grid}$	Power taken from or given to the grid	W
$P_{max}$	Maximum power permitted in the system	W
$R_c$	Resistor of a resonant converter	$\Omega$
$R_{bus}$	Resistor in parallel to the Cbus to make a voltage divider	$\Omega$
$s$	Frequency domain complex variable	
$\tau_{si}$	Time constant of the current sensor	seconds
$\tau_{sv}$	Time constant of the voltage sensor	seconds
$t$	Time	seconds
$T_c$	Commutation period	seconds
$T_{dc,i}$	Transistor number i of the DC/DC converter	
$T_i$	Transistor number i of the Full Bridge	
$T_n$	Time constant of the PI controller	seconds
$T_{on}$	Commutation period's part when the transistor is switched-on	seconds
$T_s, T_{sam}$	Sampling period of the digital control	seconds
$V_{12}, V_{23}, V_{31}$	AC line voltage before being filtered, in the Full Bridge's output	V
$V_{1n}, V_{2n}, V_{3n}$	AC phase voltage before being filtered, in the Full Bridge's output	V
$V_{AC}$	AC voltage, in the grid side	V
$V_{bat}$	Battery voltage	V
$V_{bus}$	DC-Bus voltage	V
$V_{cell}$	Voltage of one cell of the battery	V
$V_{con}$	Control voltage for the PWM	V
$V_{DC}$	DC voltage, in the DC-Bus or battery side	V
$V_{DC,mf}$	Measured and filtered DC voltage, in the DC-Bus or battery side	V
$V_{grid}$	Grid voltage	V
$V_{Lbat}$	Voltage drop in the battery side inductor	V
$V_{max}$	Maximum voltage permitted in the DC-Bus	V
$V_r, V_s, V_t$	Grid's phase voltages for 3-Phase systems	V
$V_{rms}$	RMS value of the grid voltage	V
$V_{tri}$	Triangular wave for the PWM	V
$V_{Tdc,i}$	Voltage in the DC/DC converter's transistor number i	V
$\omega_{ci}$	Current sensor's filtering frequency	Rad/s
$\omega_{cv}$	Voltage sensor's filtering frequency	Rad/s
$\omega_{filterLC}$	AC output LC filter's frequency	Rad/s
$\omega_{grid}$	Grid's frequency	Rad/s
$\omega_n$	Undamped Natural Frequency of a Second Order system	Rad/s
$\omega_r$	Resonance frequency of the PR controller	Rad/s
$\omega_s$	Synchronism frequency	Rad/s
$x_1, x_2, x_3$	Transform functions of the 3-Phase Full Bridge	

# Table of Contents

- Acknowledgments ..... i**
- Abstract... .. ii**
- Nomenclature..... iii**
- Table of Contents..... v**
- List of Figures.....viii**
- List of Tables.....xi**
  
- 1. INTRODUCTION ..... 1**
  - 1.1. Context ..... 1
  - 1.2. Electric Vehicles ..... 1
  - 1.3. Vehicle-to-Grid Application ..... 2
  - 1.4. Main Challenges ..... 2
  - 1.5. Thesis Objectives ..... 3
  - 1.6. Thesis Layout ..... 4
  
- 2. STATE OF ART: ANALYSIS OF THE TRENDS IN V2G AND G2V TECHNOLOGIES ..... 5**
  - 2.1. Chargers Technologies ..... 5
    - 2.1.1. Unidirectional vs. Bidirectional Chargers ..... 5
    - 2.1.2. On-Board vs. Off-Board Chargers ..... 6
    - 2.1.3. Conductive vs. Inductive Chargers ..... 8
  - 2.2. Assessment of V2G and G2V Converter Topologies..... 11
    - 2.2.1. AC/DC Converters for High Voltage Batteries ..... 11
    - 2.2.2. AC/DC and DC/DC Converters for Low Voltage Batteries ..... 14
    - 2.2.3. Isolated and Resonant Structures ..... 18
      - 2.2.3.1. AC/DC Converter with Galvanic Isolation ..... 20
  - 2.3. Review of Control Methodologies for V2G and G2V Systems ..... 21
    - 2.3.1. Battery Charging Methodologies ..... 22
    - 2.3.2. Control Techniques..... 26
      - 2.3.2.1. Hysteresis Current Control (HCC) ..... 26
      - 2.3.2.2. Proportional-Integral Control (PIC)..... 27
      - 2.3.2.3. Proportional-Resonant Controller (PRC) ..... 29

2.3.2.4. Comparison of the Control Techniques .....	30
<b>3. DESIGN AND MODELING OF V2G AND G2V SYSTEMS AT DIFFERENT POWER LEVELS.....</b>	<b>31</b>
3.1. Topology 1: Full Bridge converter for Low Power applications .....	31
3.2. Topology 2: Full Bridge and DC/DC converter for Low Power applications .....	33
3.3. Topology 3: Full Bridge converter for High Power applications.....	34
3.4. Topology 4: Full Bridge and DC/DC converter for High Power applications .....	36
<b>4. CONTROL DESIGN.....</b>	<b>37</b>
4.1. Grid Current Control.....	39
4.1.1. Stability and Velocity Study .....	41
4.1.2. Modeling of the Grid Current control .....	45
4.1.3. PI Parameters Calculation .....	46
4.2. DC-Bus Voltage Control .....	47
4.2.1. Stability and Velocity Study .....	48
4.2.2. Modeling of the DC-Bus Voltage control.....	50
4.2.3. PI Parameters Calculation .....	50
4.3. Grid Power Control.....	51
4.4. Battery Current Control.....	52
4.4.1. Modeling of the Battery Current control .....	53
4.4.2. PI Parameters Calculation .....	54
4.5. Battery Voltage Control.....	55
4.5.1. Modeling of the Battery Voltage control .....	55
4.5.2. PI Parameters Calculation .....	56
4.6. Battery Power Control.....	56
<b>5. VERIFICATION AND SIMULATION RESULTS.....</b>	<b>57</b>
5.1. Topology 1: Full Bridge converter for Low Power applications .....	57
5.2. Topology 2: Full Bridge and DC/DC converter for Low Power applications.....	64
5.3. Topology 3: Full Bridge converter for High Power applications.....	67
5.4. Topology 4: Full Bridge and DC/DC converter for High Power applications .....	70
5.5. Experimental Analysis of Commercial Vehicle Charger.....	73

<b>6. CONCLUSION .....</b>	<b>75</b>
<b>7. FUTURE PERSPECTIVE.....</b>	<b>77</b>
<b>8. REFERENCES.....</b>	<b>79</b>
<b>APPENDIX.....</b>	<b>i</b>
<b>A. Elements Calculation.....</b>	<b>i</b>
1. Topology 1: Full Bridge converter for Low Power applications.....	i
2. Topology 2: Full Bridge and DC/DC converter for Low Power applications .....	ii
3. Topology 3: Full Bridge converter for High Power applications .....	iii
4. Topology 4: Full Bridge and DC/DC converter for High Power applications .....	vi
<b>B. Modeling of V2G and G2V systems.....</b>	<b>vi</b>
Topology 1: Modeling of Full Bridge converter for Low Power applications .....	vii
Topology 2: Modeling of Full Bridge and DC/DC converter for Low Power applications.....	ix
Topology 3: Modeling of Full Bridge converter for High Power applications .....	xiii
Topology 4: Modeling of Full Bridge and DC/DC converter for High Power applications.....	xv



# List of Figures

- Figure 1. Diagram of an EV with V2G application ..... 2
- Figure 2. Power flow in a general charger’s structure..... 5
- Figure 3. Structure of integrated chargers..... 7
- Figure 4. Comparison between On-Board, Off-Board and Integrated chargers..... 8
- Figure 5. Example of the structure of an Inductive Charger..... 9
- Figure 6. Comparison between conductive and inductive chargers ..... 10
- Figure 7. Typical structure of an EV with its control scheme..... 11
- Figure 8. Converter with a LF Transformer ..... 18
- Figure 9. Converter with a HF Transformer ..... 18
- Figure 10. Series resonant converter ..... 19
- Figure 11. Parallel resonant converter ..... 19
- Figure 12. Series-Parallel resonant converter ..... 20
- Figure 13. Isolated bidirectional single stage AC/DC converter ..... 20
- Figure 14. Battery current and voltage during CV Charging..... 23
- Figure 15. CV Charging block diagram..... 23
- Figure 16. Battery current and voltage during CC Charging..... 23
- Figure 17. CC Charging block diagram ..... 24
- Figure 18. Battery current and voltage during CC-CV Charging ..... 24
- Figure 19. CC-CV Charging block diagram ..... 24
- Figure 20. Battery current and voltage during Pulsing Charging ..... 25
- Figure 21. Battery current during Reflex™ Charging ..... 25
- Figure 22. Diagram of the control and power flow in an on-board battery charger ..... 26
- Figure 23. Block diagram of the HCC..... 26
- Figure 24. Block diagram of the PIC ..... 27
- Figure 25. Block diagram of the DQ Control..... 28
- Figure 26. Grid current and voltage when DQ Control is applied ..... 28
- Figure 27. Block diagram of the PRC ..... 29
- Figure 28. Bode Plot of the PR controller ..... 30
- Figure 29. Comparison of the control strategies..... 30
- Figure 30. Single-Phase Full-Bridge converter..... 31
- Figure 31. Simulink model of the Full Bridge for Low Power Applications ..... 33
- Figure 32. Two quadrant Converter and its power flow ..... 33

Figure 33. Simulink model of the Full Bridge and the Two-quadrant converter for Low Power Applications.....	34
Figure 34. Three-Phase Full-Bridge converter.....	35
Figure 35. Control signals, switching orders, grid current and commutated voltage when the grid voltage crosses zero .....	35
Figure 36. Simulink model of the Full Bridge for High Power Applications.....	35
Figure 37. Simulink model of the Full Bridge and the Two-quadrant converter for High Power Applications.....	36
Figure 38. Bode plot with the PM, GM, Cross-over frequency and Band Width .....	38
Figure 39. Block diagram of the Grid Current Control Loop.....	39
Figure 40. Model of the digitalization in S Domain.....	40
Figure 41. Block diagrams of the phase current control loops for 3-phase systems .....	41
Figure 42. Step response, Root Locus and Bode Plots of the Grid Current control system for a PM of 45° and cross-over frequencies of 1200, 1000 and 500 Hz.....	42
Figure 43. Step response, Root Locus and Bode Plots of the Grid Current control system for a PM of 45° and cross-over frequencies from 500 to 1000 Hz.....	43
Figure 44. Step response, Root Locus and Bode Plots of the Grid Current control system for different PM and a $F_c=1000$ Hz .....	44
Figure 45. Step response of the Grid Current control system for $f_c=1000$ Hz and different PM.....	45
Figure 46. Simulink model of the grid current control for Low Power Applications.....	46
Figure 47. Simulink model of the Grid Current control loops for High Power Applications .....	46
Figure 48. Block diagram of the DC-Bus Voltage Control Loop.....	47
Figure 49. Step response, Root Locus and Bode Plots of the DC-Bus control system for a PM of 45° and cross-over frequencies from 1 to 100 Hz .....	49
Figure 50. Simulink model of the DC-Bus Voltage Control for Low Power Applications.....	50
Figure 51. Simulink model of the DC-Bus Voltage Control for High Power Applications.....	50
Figure 52. Simulink model for the Grid Power control for Low Power Applications .....	51
Figure 53. Simulink model for the Grid Power control for High Power Applications.....	51
Figure 54. Block diagram of the Battery Current Control Loop.....	52
Figure 55. Simulink model of the battery current control during charging mode .....	54
Figure 56. Simulink model of the battery current control during discharging mode .....	54
Figure 57. Block diagram of the Battery Voltage Control Loop.....	55
Figure 58. Simulink model of the Battery Voltage Control .....	56
Figure 59. Simulink model of the battery power control.....	56
Figure 60. Grid Current and Voltage at maximum power for Bipolar Modulation .....	57

Figure 61. Harmonic content of the grid current for Bipolar Modulation .....	58
Figure 62. Harmonic content of the grid current in charging mode for Unipolar Modulation.....	58
Figure 63. Grid Voltage before and after being filtered for bipolar modulation .....	59
Figure 64. Harmonic content of the AC Voltage V12 for bipolar modulation.....	59
Figure 65. Grid and AC voltage characteristics for Unipolar Modulation .....	60
Figure 66. PWM and sitching patterns, at 20 kHz .....	60
Figure 67. Grid and battery power at charging mode.....	61
Figure 68. Battery's voltage evolution for CV Charging .....	61
Figure 69. Battery's SoC, current, voltage and power for CV Charging .....	62
Figure 70. Transition between charging and discharging modes.....	63
Figure 71. Change in the reference current during CP Charging.....	64
Figure 72. Grid current and voltage for CV methodology .....	65
Figure 73. DC-Bus Voltage and its reference for CV Charging.....	65
Figure 74. PWM and switching orders for the Two-quadrant converter.....	66
Figure 75. Behaviour of the Two-Quadrant converter's control loops for CV charging mode .....	67
Figure 76. Battery's SoC, current, voltage and power adding a Two-Quadrant converter for CVC.....	67
Figure 77. PWM and switching patterns of the 3-phase Full Bridge.....	68
Figure 78. Behaviour of the Full Bridge's control loops for charging mode.....	68
Figure 79. Grid's currents and voltages for CV methodology .....	69
Figure 80. Battery's SoC, current, voltage and power for the 3-phase system for CVC .....	69
Figure 81. Grid voltages and currents for CC methodology .....	70
Figure 82. Harmonics content of the grid's phase currents for CC charging mode .....	71
Figure 83. Phase and Line AC Voltages for 3-Phase systems .....	72
Figure 84. Current and voltage supplied to the Nissan Leaf .....	74
Figure 85. Harmonic content of the grid voltage and current for all the designed topologies.....	75

## List of Tables

Table 1. Comparison between unidirectional and bidirectional chargers .....	6
Table 2. Standard charging levels.....	6
Table 3. Comparison between On-Board, Off-Board and Integrated chargers.....	8
Table 4. Comparison between conductive and inductive chargers .....	10
Table 5. Comparison of AC-DC Converters for HV-Battery connection.....	14
Table 6. Comparison of DC-DC Converters for LV-Battery connection .....	17
Table 7. Commutation states of the FB.....	31
Table 8. Comparison of the main modulation techniques for a FB converter .....	32
Table 9. Main characteristics of the Low Power system connected to HV-Batteries .....	33
Table 10. Main characteristics of the Low Power system connected to LV-Batteries.....	34
Table 11. Main characteristics of the High Power system connected to HV-Batteries .....	36
Table 12. Main characteristics of the Low Power system connected to LV-Batteries.....	36
Table 13. Information of the Step response of the Grid Current control system for a PM of 45° .....	45
Table 14. Information of the Step response of the Grid Current control system for a cross-over frequency of 1000 Hz .....	45
Table 15. Parameters of the Grid Current PI controller.....	47
Table 16. Information of the Step response of the DC-Bus control system for a PM of 45° .....	48
Table 17. Parameters of the DC-Bus Voltage PI controller .....	51
Table 18. Parameters of the Battery Current PI controller .....	54
Table 19. Parameters of the Battery Voltage PI controller.....	56
Table 20. FFT Analysis of Igrid and V12 before and after adding a Two-Quadrant converter .....	65
Table 21. FFT Analysis of the grid currents and AC Voltages for CV methodology.....	70
Table 22. FFT Analysis of the grid currents and AC Voltages for CV when adding the Two-Quadrant Converter .....	73
Table 23. Measured data from a Nissan Leaf while charging .....	73

# 1. INTRODUCTION

## 1.1. Context

In the present days, there exist a lot of concerns related to the pollution of the air, the reliance on fossil fuels, energy dependence, climate change and the increase of the energy cost. Thus, many research activities are being done to develop new energy technologies in order to minimize reliance on conventional energy resources. The major efforts are centered in the electricity generation sector and in transportation, since they are main consumers of fossil fuels [1], [2], [3].

One key point is the deployment of renewable energies since they are clean and free resources. Nevertheless, their inherent variability restrains their installation. To overcome this drawback, energy storage systems are essential and in particular, as recent studies have shown [4], Electric Vehicles (EVs) are definitively advantageous over other traditional energy-storage technologies thanks to its easy implementation and being environmentally friendly.

## 1.2. Electric Vehicles

The main characteristic of an Electric Vehicle (EV) is that it uses an electric motor rather than an internal-combustion engine for propulsion. They can be split in three groups: vehicles connected continuously to an off-board electric supply, vehicles with an on-board generator or vehicles including an on-board rechargeable storage system (such as batteries, flywheels or double-layer capacitors) [5]. Inside this last group, the plug-in electric vehicles (PEVs) can be recharged from an external source of electricity. PEVs include battery electric vehicles (BEVs), plug-in hybrid vehicles (PHEVs) and conversions of conventional vehicles [6].

The main advantages of using EVs are the following [6], [7]:

- Reduction of air pollution and CO<sub>2</sub> emissions;
- Less dependence on fossil-fuel energy;
- Higher installation of renewable resources;
- Better price of energy;
- Flattening the demand curve;
- Provision of ancillary services;
- Vehicle-to-Grid application.

On the other hand, the use of these systems also carries disadvantages [6], [7]:

- Higher cost;
- Need of availability of charging infrastructure;
- Overload of the transmission and transportation networks;
- Safety risks associated with noise reduction and battery fire.

### 1.3. Vehicle-to-Grid Application

In particular, the BEVs are going to be analyzed in this paper, since they are part of the Vehicle-to-Grid (V2G) application, which consists on having direct power flow between the vehicle and the grid. To develop this concept it is required to implement two connections, as explained in [8]: the power connection to transmit the electricity, and the logic and control connections to assure this system is useful and harmless to the grid [4]. Both these connections are depicted in Figure 1.

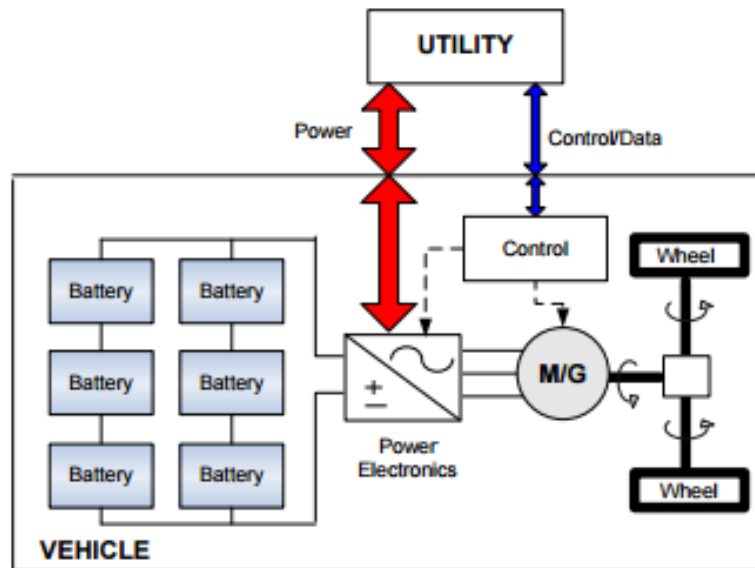


Figure 1. Diagram of an EV with V2G application [8]

If effectively used and introduced in a smart grid, the V2G application can increase the supply grid efficiency, reliability, stability and generation dispatch [4]. It can offer the following services [4], [9], [10]:

1. Ancillary services: voltage regulation (reactive power) and frequency regulation (active power), load management to flatten the demand curve (charge at valley hours and discharge at peak hours) and support to renewable energies;
2. Improvement of load factors;
3. Current harmonics reduction;
4. Faster repaid of the storage systems.

### 1.4. Main Challenges

Vehicle-to-grid (V2G) application is still in development process, so despite its numerous contributions to the electricity grid, as mentioned in the previous section, it has to surpass some challenges before becoming a widespread reality.

First of all, this technology has to assure convenience for the user, in means of not finding the vehicles uncharged whenever they need to be utilized. This fear discourages a lot of people from

buying an electric vehicle [11]. On the other hand, it is essential that the electricity grid is not perturbed by the V2G application. If the power supplied by the EV does not satisfy the quality requirements imposed by the grid, it cannot be delivered. Related to this aspect, special attention must be paid to the Power Factor Correction (PFC); it is important to maintain it as close as possible to the unity so that all the power produced can be utilized. The delivered current must contain a low amount of harmonics in order to respect the EMC regulations. In addition, the DC currents must be eliminated to avoid the saturation of the grid's transformers [12]. A reduction of efficiency and voltage deviations may also be present, produced by the overload of transformers, cables, and feeders [9]. The battery's degradation should be considered as well, since the increase of charging and discharging cycles can reduce its lifespan or life cycle [4]. Furthermore, the bigger is the amount of PEVs connected to the grid, the more severe are the previous problems in the power distribution system [4].

The aforementioned drawbacks are also present in renewable generation systems, for which a lot of topologies and different solutions are already being investigated [12]. Some of these solutions may as well be applied to the Electric Vehicle technology. Another challenge that not only the V2G application, but the EV technology in general must overcome is their high cost [4], [13]. Finally, this application is intended to be used in a Smart Grid [4], so this last concept needs to be developed too.

## 1.5. Thesis Objectives

The main objective of this thesis consists of showing how both the Grid-to-Vehicle and Vehicle-to-Grid applications can be implemented. Four different topologies have been developed and simulated using Matlab/Simulink Platform; two of them correspond to a low power application of 3.3 kW (with /without DC/DC converters), while the other two are for Fast Charging and high power applications of 22 kW (with /without DC/DC converters):

- Topology 1: Full Bridge converter for Low Power applications;
- Topology 2: Full Bridge and DC/DC converter for Low Power applications;
- Topology 3: Full Bridge converter for High Power applications;
- Topology 4: Full Bridge and DC/DC converter for High Power applications.

Various control strategies have been implemented for each kind of the charger's topology, and their stability and dynamic response have been analyzed. Afterwards, their results have been presented and assessed in order to see the perturbations and disturbances that these applications can cause on the electricity grid. In particular, current and voltage harmonics have been performed to study their impact of the grid stability and performance.

On the other hand, another important objective of this thesis consists on presenting a State of Art of the main kind of chargers and power electronic topologies that can be used to implement the V2G and G2V modes, as well as the charging methodologies and control strategies needed for that purpose.

## 1.6. Thesis Layout

This master thesis is organized as follows:

**Chapter 1** presents one context in which Electric Vehicles could be very advantageous, emphasizing their main strengths and possible applications. Afterwards, Vehicle-to-Grid and Grid-to-Vehicle concepts are introduced and explained.

**Chapter 2** provides a state of art of the trends in V2G and G2V technologies. First of all, different kinds of chargers are presented and compared. The results of these comparisons are shown in tables and graphs. Thereafter, the most used power electronic topologies are presented, starting from the simplest structures to more complex ones, integrating more than one converter and even a transformer. Finally, the existing charging strategies are introduced while their different control methodologies are explained.

**Chapter 3** presents the design stage of the topologies mentioned in the previous section. The values of their elements are provided, although their calculation is explained in detail in the Appendix.

**Chapter 4** covers the implementation of the control strategies presented in the state of art. The calculation of the control parameters is explained and an analysis of the optimal cross-over frequency and Phase Margin is made for each control loop.

**Chapter 5** presents the results of the simulation of all the developed models. Especial attention is provided in showing plots of the grid current and voltage, their harmonic content and the correct operation of the control strategies. Furthermore, these results are compared to real measurements taken from a Nissan Leaf during G2V mode.

The **Appendix** provides an overall view of the topologies implemented in Matlab/Simulink Platform and the calculation of the converter's elements. For this calculation, some formulas and algorithms are taken from literature.



# 2. STATE OF ART: ANALYSIS OF THE TRENDS IN V2G AND G2V TECHNOLOGIES

## 2.1. Chargers Technologies

### 2.1.1. Unidirectional vs. Bidirectional Chargers

A battery charger is a device comprising one or more power electronics circuits that are used to convert electrical energy. These power converters are different depending on the direction of the power flow between the grid and the battery, the charging and discharging requirements of the battery and the grid parameters [14].

As explained in [14], the power flow in a charger can be unidirectional (the batteries are only charged and the vehicle is considered as a load) or bidirectional (the batteries charge and discharge, so they can be seen as loads and generators, respectively). In the first case, only G2V mode is implemented, whereas in the second, both G2V and V2G modes can be operated. The power flow in a general charger’s structure is seen in Figure 2.

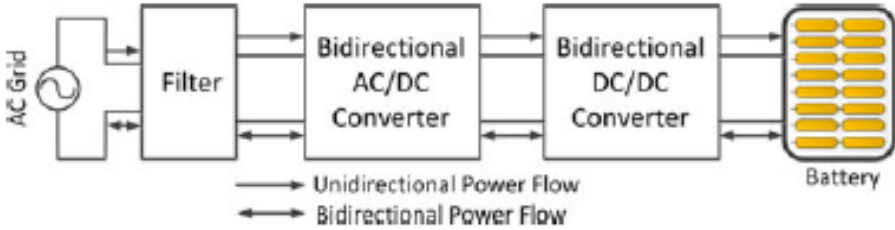


Figure 2. Power flow in a general charger’s structure [14]

The unidirectional charger is the first one considered because of its simplicity, less hardware and interconnection requirements and less battery degradation [15]. However, as the power flows only from the grid to the vehicle, the services that the V2G application could provide are limited. The typical configuration comprises a diode bridge rectifier, a filter and a DC/DC converter. Normally, to reduce cost, weight, volume and power losses, these converters are implemented in a single stage [16].

On the other hand, a bidirectional charger, even if more complicated, can provide further benefits to the electricity grid and higher quality ancillary services. When the battery is being charged, the charger has to take from the grid a sinusoidal current with a certain phase angle, depending on the active and reactive power desired. On the contrary, in discharge mode, the charger can deliver a controlled sinusoidal current to the grid [15]. The typical configuration comprises two stages. Firstly, a bidirectional AC/DC converter is installed in the grid side in order to control the current wave form and PF. Afterwards, a bidirectional DC/DC converter is used in the battery side with the purpose of controlling the battery’s voltage, current or power, depending on its operation requirements [17], [18].

The main differences between the two charger's options are included in the following Table 1, as in [15], [19]:

UNIDIRECTIONAL	BIDIRECTIONAL
Simple control	Complex control
Less cost (less hardware)	More cost and investment
No extra investment needed	More information exchange required; Need of distribution system upgrade
Safer	Need of safety measures, anti-islanding protection
Less battery degradation	Degradation due to frequent cycling
Available for Level 1, 2 and 3	Expected for Level 2
Lower efficiency	Higher efficiency
Voltage (reactive power) and frequency (active power in one way) control	Better services; voltage and frequency regulation (down-up), spinning reserves, energy balance, load following, harmonics filtering

Table 1. Comparison between unidirectional and bidirectional chargers [15], [19]

### 2.1.2. On-Board vs. Off-Board Chargers

The charger's structure can be included or not in the vehicle, and these chargers receive the name of On-Board and Off-Board chargers, respectively. Depending on where it is placed, different charging levels can be achieved. The standardized charging levels, as in [4], [14], [15], can be seen in Table 2:

Level	Type	Voltage	Phase	Power	$I_{max}$	Time	Location	Use	Cost
1	Opportunity charger	$V_{AC}$ 230V	1 phase	1.4 kW 1.9 kW	12 A 20 A	4-11 h 11-36 h	On-Board	Home or office	500-880 \$
2	Primary dedicated charger	$V_{AC}$ 400V	1 or 3 phase	4 kW 8 kW 19.2 kW	17 A 32 A 80 A	1-4 h 2-6 h 2-3 h	On-Board	Private or public outlets	1000-3000 \$
3	Fast charging	$V_{AC}, V_{DC}$ 208-600 V	3 phase	<100 kW	400 A	0.2-1 h	Off-board	Commercial	30000-160000 \$

Table 2. Standard charging levels [4], [14], [15]

As it can be seen in the previous Table 2, On-Board chargers are limited to level 1 and 2 (slow charging) because of cost, weight and space constraints (inductors, capacitors, cooling system and possible isolating transformer are voluminous). In fact, less than 5 kg chargers are needed, thus they have to be very compact [1].

The main advantage of On-Board chargers is their capability to charge the batteries wherever a suitable power source is available. In fact, On-Board chargers can use any household outlet [20],

whose high availability would increase the acceptance of Plug-in Electric Vehicles, especially in the case of those dedicated to urban mobility [11], [14].

On-Board chargers used at home usually charge during the night, which has minimal impact on the supply grid [4], and they can facilitate the load level control of power utilities as the electricity demand at night is relatively low [1].

Another considered option for On-Board chargers consists of integrating the battery charger into the electric drive system of the PEV, as in [4]. This configuration is depicted in Figure 3. This integration can be possible if traction and charging are not simultaneous. In this case, the motor windings serve as filter inductors or as isolated transformer, and the motor inverter is used as a bidirectional AC/DC converter. Consequently, weigh, volume and cost are minimized while faster charging (level 2 and 3) can be achieved [14], [20]. In addition, these chargers are bi-directional by design [20], [21].

However, since integrated chargers use the motor’s inductance as the input inductance of the inverter, the value of this inductor may not be the optimal one for the inverter’s operation [14]. Furthermore, this topology has more copper losses in the motor’s windings [22]. For marketing purposes, the control complexity and extra hardware needed are challenges to overcome [14], [15].

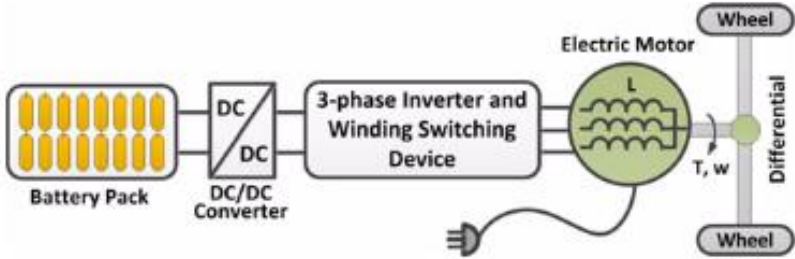


Figure 3. Structure of integrated chargers [4]

Off-Board chargers do not have space or weight constraints, and that is why they are capable to operate with higher power levels with which fast charging can be achieved (although they can also be used for Level 1 and 2). This kind of fast chargers take AC power from the grid and transform it to DC power that is then delivered to the vehicle [11], [21].

Since the EV must inevitably include some power electronics for the traction, having an Off-Board charger entails redundant power electronics and thus an extra cost. In addition, fast charging can overload the distribution network because of its high power demand, typically larger than double of a household load [1], [23]. Further disadvantages involve the risk of vandalism and extra clutter in an urban environment [4], [15].

On the other hand, fast charging along the roads can reduce the battery size and weight, as well as the average energy needed [4]. Thus, the overall system’s efficiency can reach higher values. Moreover, a hast growth of the EV market may occur thanks to the confidence that fast chargers transmit to the drivers about not being stranded [21].

The main advantages and disadvantages of the previous types of chargers, as presented in [1], [4], [14], [15], [20], [21] and [22], can be seen in Table 3. Figure 4 shows the scores of these chargers in

different aspects, being 0 the worst punctuation and 10 the best. It must be noted that integrated chargers can be a good option since they have the main advantages of On-Board chargers plus the higher power capability of Off-Board chargers. In addition, these chargers are bi-directional and can be both conductive and inductive. Nevertheless, because of their control difficulties and hardware requirements, regular Level 2 single-phase On-Board chargers are the most commonly used instead [15].

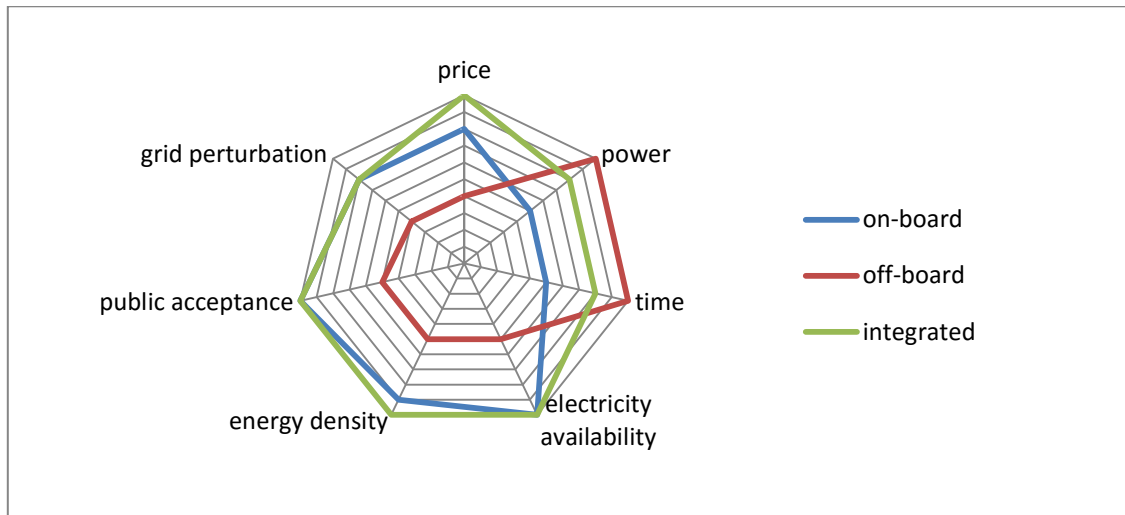


Figure 4. Comparison between On-Board, Off-Board and Integrated chargers

	ADVANTAGES	DISADVANTAGES
<b>ON-BOARD</b>	Lower price (500-3000 €) [15] Small size and compact (less than 5 kg) [1] Charging availability [14] [15][20] Minimal impact to the grid [4][15]	Slow charging (6-8 h) [14][21] Power limitation [14] Weight and size constraints [1][14][15]
<b>OFF-BOARD</b>	Faster charging (less than 1 hour) [15] No size or weigh constraints [14] [15][20] Enables long distance travelling [21]	Higher price (30000-160000€) [15] Redundant power electronics [15] More impact to grid [1][4][15][21] Risk of vandalism to charging stations [4][15] Cluttering in an urban environment [4][15]
<b>INTEGRATED</b>	Fast charging (less than 1 hour) [14][15] Charging availability [14] Minimize weigh, volume and cost [14][20] Bi-directional by design [20][21]	More copper losses of the motor windings [14][22] Not optimal inductance for the inverter [14] Control complexity [14][15] Extra hardware[14][15]

Table 3. Comparison between On-Board, Off-Board and Integrated chargers

### 2.1.3. Conductive vs. Inductive Chargers

The connection between the grid and the vehicle can be either conductive or inductive. On the one hand, Off-Board chargers (for fast charging) are conductive since the power they transmit to the EV is

DC. On the other hand, On-Board chargers delivering AC current can be both inductive and conductive.

Conductive chargers connect the charge inlet to the connector of the EV using a cable, which can be fed with the three power levels. The main disadvantage of this technology is the necessity of the driver to manually plug in this cable [15]. Additionally, there exist safety risks in wet and damp conditions, and an easy automation cannot be achieved [24].

There are some standards that define the types of connectors. In particular, the IEC 62196 Type 2 connector is the standard for deployment in Europe. This type of connector, also known as Mennekes, can charge the battery within the power range from 3 to 70 kW, provided as single-phase or three-phase, AC or DC [25].

On the contrary, the power transfer in an inductive charger is magnetically. This kind of charger comprises two different parts: the grid side in which AC current is taken, rectified and converted to a high frequency [26]; and the secondary side, situated in the vehicle, which consists on an AC/DC converter connected to the battery. At the end of each side, a winding is located forming a transformer through which the power is transmitted. As both sides of the charger are electrically separated, they can be moved with respect to the other, entailing charging while moving. As in [27], an example of this topology is shown in Figure 5.

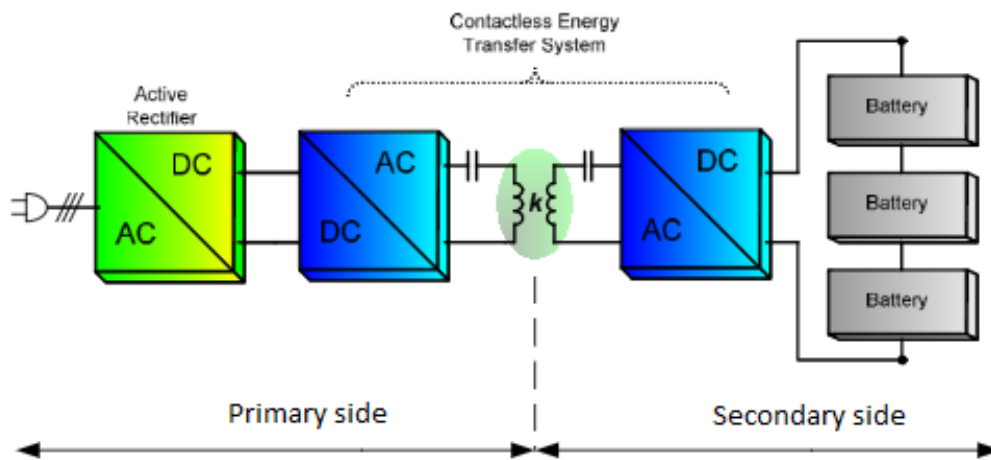


Figure 5. Example of the structure of an Inductive Charger [27]

The main strength of this technology lies in the user's convenience, since they do not have to connect anything for charging the EV. Thus, there is low risk of electric shock and it is weather-proof. Provided that the energy transmission is done via inductors, there exists galvanic isolation between the charger and the vehicle, which grants safety advantages. Moreover, this technology may have a potential use with ultracaps [28]. Another remarkable quality of this sort of charger is the possibility to reduce the battery size and extend the vehicle range, as more frequent charging is enabled [24].

The major drawback of this technology lies on its lower efficiency compared to conductive chargers [15][26][28]. The mutual inductance of the transformer is very small due to the big air gap between

the two windings, whereas leakage inductances are larger than in a conventional transformer. Consequently, there exist high conducting losses and winding losses [27]. For this main reason, only slow charging (Level 1 and 2) is used. Other disadvantages of these chargers are low power density, manufacturing complexity, necessity of specific equipment (no exchangeability), more size and higher cost [15].

The major advantages and disadvantages of these systems, as presented in [15], [24], [26], [27] and [28], are compared in the following Table 4. Figure 6 shows the scores of these chargers in different aspects, being 0 the worst punctuation and 10 the best one.

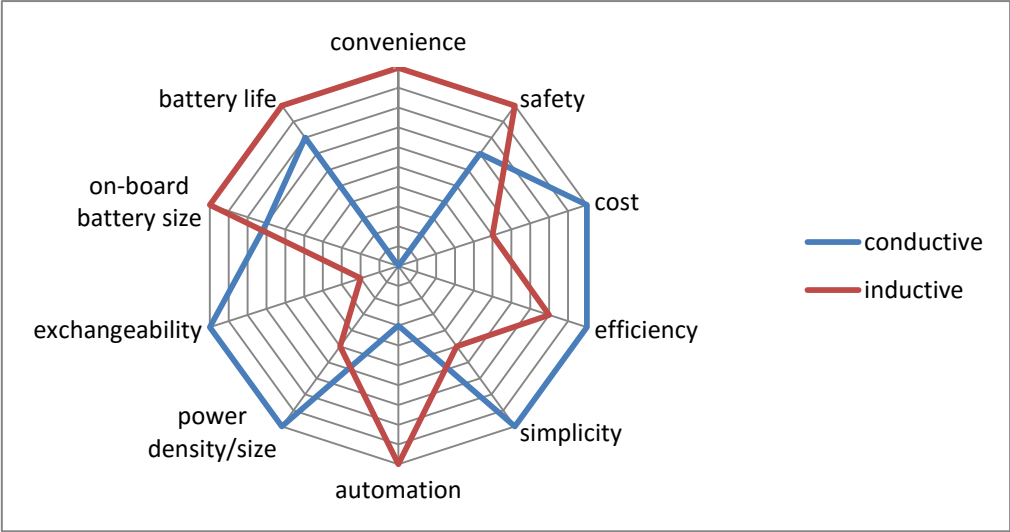


Figure 6. Comparison between conductive and inductive chargers

	ADVANTAGES	DISADVANTAGES
<b>CONDUCTIVE</b>	<ul style="list-style-type: none"> <li>All power levels (slow and fast charging) [15]</li> <li>Simplicity [15][26]</li> <li>Higher Efficiency [26]</li> <li>Better price</li> <li>Standardization [30]</li> </ul>	<ul style="list-style-type: none"> <li>Manual plug-in [15][24]</li> <li>Safety risks in wet conditions [24]</li> <li>Difficult automation [24]</li> </ul>
<b>INDUCTIVE</b>	<ul style="list-style-type: none"> <li>Convenience for user [15][24]</li> <li>Weather proof [26][27][28]</li> <li>Increase in safety [24][27][28]</li> <li>Galvanic isolation [15][27]</li> <li>More frequent charging is enabled [15][24]</li> <li>Charging while driving [15][26]</li> <li>Easier automation [24][27]</li> </ul>	<ul style="list-style-type: none"> <li>Lower efficiency [15][26][28]</li> <li>Slow charging (Level 1 &amp; 2) [15]</li> <li>Low power density [15]</li> <li>More manufacturing complexity [15][28]</li> <li>More size and cost [15][26][28]</li> <li>Specific equipment (no exchangeability) [28]</li> </ul>

Table 4. Comparison between conductive and inductive chargers

In the last years, the main trend is to focus on lower power ratings for inductive charging (because of weight, cost, safety, etc.); and higher power for conductive charging [28]. However, this would mean using two different chargers for a single vehicle, which currently is economically unviable.

## 2.2. Assessment of V2G and G2V Converter Topologies

In general, the powertrain of an Electric Vehicle comprises a battery pack, a three-phase DC/AC inverter connected to the electric motor, a single-phase AC/DC on-board battery charger and the transmission systems, as explained in [29]. All these elements are shown in Figure 7.

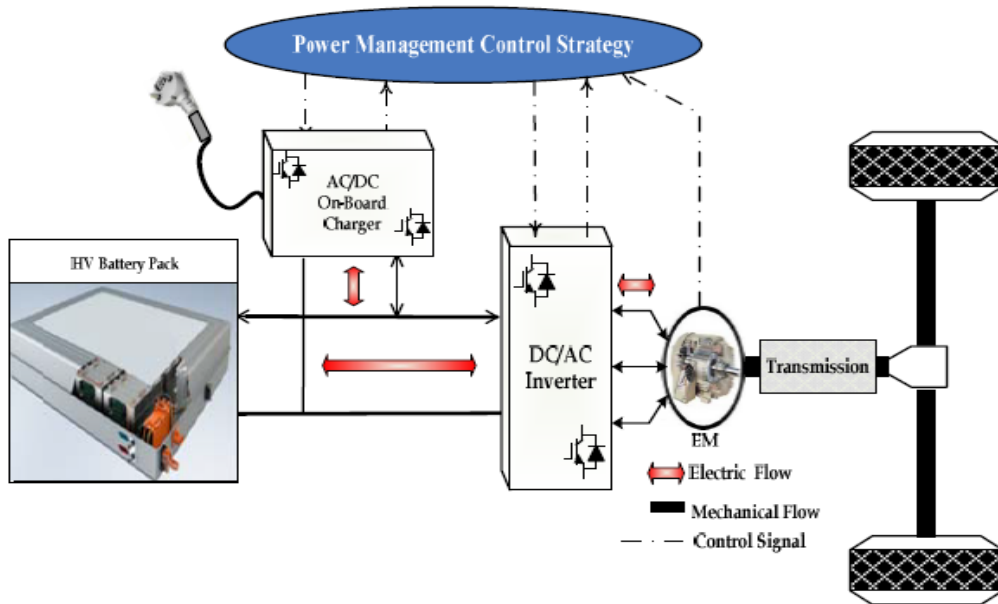


Figure 7. Typical structure of an EV with its control scheme [29]

As mentioned previously, bidirectional On-Board conductive chargers have recently drawn attention thanks to their advantages in charging accessibility, easy use and high efficiency.

Depending on the battery pack's voltage, the charger can comprise different topologies. When a High Voltage (HV) battery pack is used, only an AC/DC converter might be utilized to connect it to the grid. On the contrary, when Low Voltage (LV) batteries are used, there must be an intermediate DC/DC converter to boost the voltage to the needed value in the DC-Bus [29]. The main advantage of this last configuration relies on the ability of LV Batteries to recuperate more energy from the DC-Bus during the regenerative braking mode [30]. Different topologies for these converters are presented and compared in the following section.

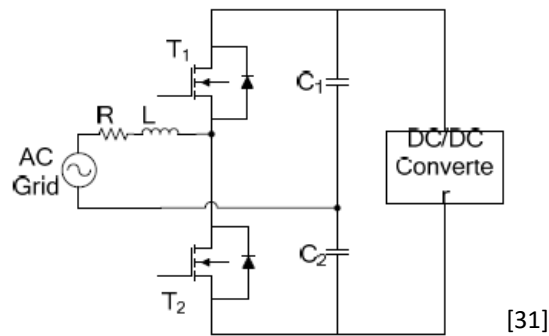
### 2.2.1. AC/DC Converters for High Voltage Batteries

To begin with, the simplest configuration consisting on just one AC/DC converter and a HV battery pack has been analyzed. There exist different topologies, as the ones presented in [12], [15], [17], [31], [32] and [33], that can be used; some of them are stored and compared in Table 5.

It must be noted that only single-phase bidirectional structures have been considered, but having in mind that they could be adapted to three-phase structures for high power applications. On the other hand, MOSFETs are employed for low power, IGBTs for medium power and GTOs for high power applications [17].

## AC/DC BIDIRECTIONAL TOPOLOGIES

### HALF-BRIDGE (HB)



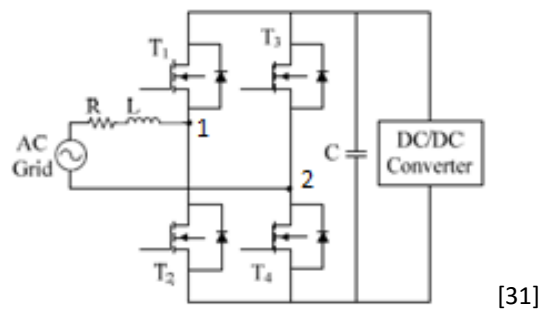
#### Advantages

Fewer components [15][31]  
 Lower cost [15][31]  
 Control simplicity [15]  
 Design simplicity [31]  
 Assures zero  $I_{bc}$  to grid [12]  
 Common mode Voltage constant with one L in the output [12][15]

#### Disadvantages

High components stress (may require more transistors in series or parallel) [15][31]  
 Many harmonic currents (need of big and expensive filter) [31]  
 Two big capacitors [15]  
 Not suitable for high power levels [31]  
 Need of twice the  $V_{dc}$  value (compared to the FB) [31]

### FULL BRIDGE (FB)



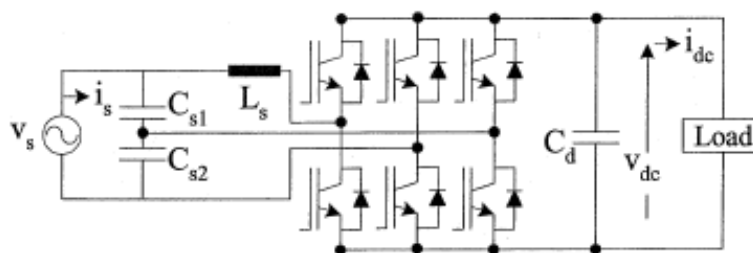
#### Advantages

Lower component stress (cheaper ones) [15][31]  
 One capacitor [31]  
 High conversion ratio and power level [15]

#### Disadvantages

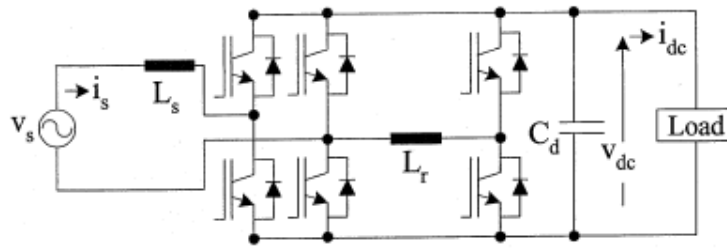
More components and PWM inputs [15][31]  
 Control complexity and cost [15][31]  
 Need a filter for harmonics [31]  
 Cannot assure zero  $I_{bc}$  to grid [12]

### FULL BRIDGE WITH DC RIPPLE COMPENSATION



(a) Using AC midpoint capacitors and third leg [17]

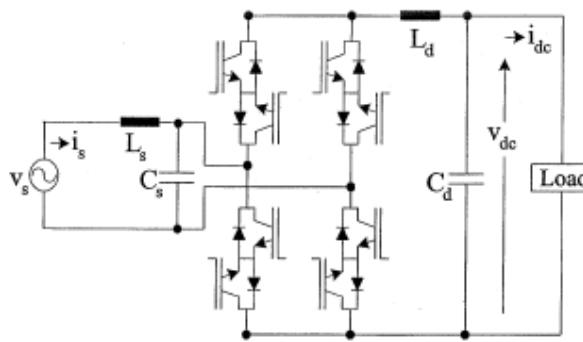




(b) Using an inductor and third leg [17]

Advantages	Disadvantages
DC-link ripple reduction (smaller capacitor) [17] Fast and wide-bandwidth control of dc output [17]	50% more switches than a conventional FB

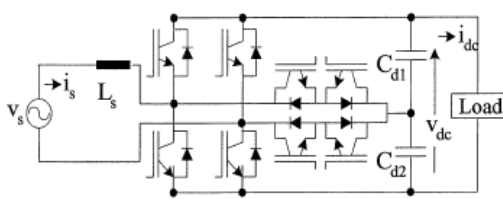
### BUCK-BOOST CONVERTER



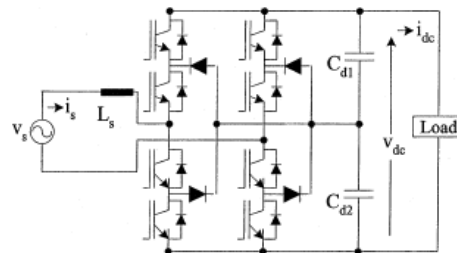
[17]

Advantages	Disadvantages
Versatility (buck and boost, current-source or voltage-source rectifier and inverter) [17] Reduced energy storage elements for fast response [17]	High amount of switches compared to the conventional HB and FB

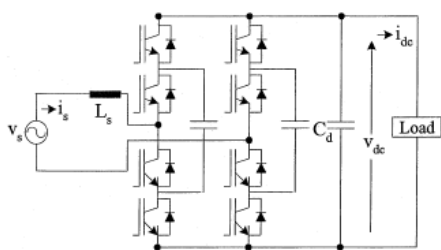
### MULTI-LEVEL



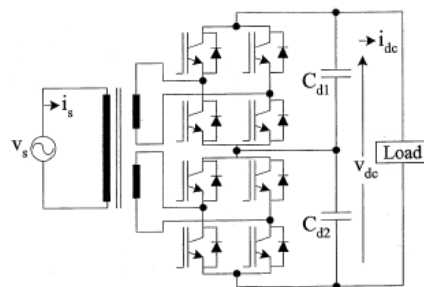
(a) 3-Level using 2 bidirectional switches [17]



(b) Diode clamped 3-level [17]



(c) Flying Capacitor clamped 3-level [17]



(d) Cascaded 5-level [17]

Advantages	Disadvantages
Lower component stress (Voltage clamped to half DC bus voltage) [15] [17][31][32] Lower losses and high efficiency [15] [17] Reduced size [15] Small and cheap filter [15] [31] Clean sinusoidal current with nearly unity PF [17][32] Reduced EMI and acoustic noise [31] DC-bus ripple-free voltage regulation [32]	Additional elements and control circuitry [15][31] More cost and complexity [15][31]
<b>MATRIX CONVERTER</b>	
Advantages	Disadvantages
Sinusoidal waveforms [15] Minimal harmonics [15] Inherent bidirectional energy flow [15] Input PF fully controlled [15] Minimal energy storage requirements (no big and expensive capacitors) [15]	Input/output voltage transfer ratio limited to 87% [15] More semiconductors [15] [33] Very sensitive to disturbances of the input voltage system [15]

Table 5. Comparison of AC/DC Converters for HV Battery connection

There exist further techniques that could be implemented on the previous topologies in order to increase their efficiency and improve their functionality [15]:

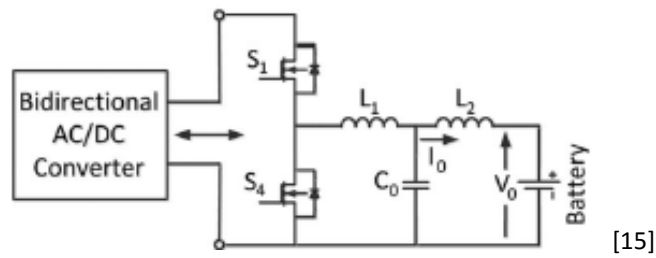
- A. Interleaving: using more than one converter in parallel reduces the battery charging current, inductor size and stress on the output capacitor;
- B. Multilevel converters: reduction of harmonics as the wave is obtained using more levels;
- C. Addition of a resonant circuit: reduction of switching stress and losses, enabling a higher efficiency;
- D. Soft switching (ZVS or ZCS): reduction of switching losses.

### 2.2.2. AC/DC and DC/DC Converters for Low Voltage Batteries

The second configuration considered consists on using Low Voltage Batteries and a DC/DC Converter to connect them to the DC-Bus. This DC-Bus is in turn connected to the grid through one of the AC/DC Converters presented before. The most used DC/DC topologies, as described in [15], [31], [34], [35], [36] and [37], are stored in Table 6. It can be noted that these topologies may include a transformer in order to provide galvanic isolation.

## DC/DC BIDIRECTIONAL TOPOLOGIES

### TWO-QUADRANT (BUCK-BOOST) CONVERTER



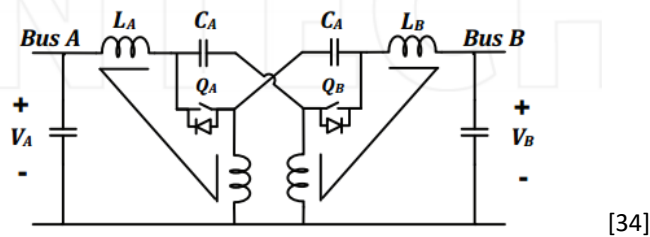
#### Advantages

Simplicity [15]  
 Few components [31] [31]  
 Simple control circuitry [31]  
 Low current ripple [34]

#### Disadvantages

Two high current inductors (bulky and expensive) [15][31]  
 Buck in one direction and boost in the other [15][31][34]  
 Impractical for high voltage ratio [34]  
 No galvanic isolation [34]

### VARIANT OF NIDC CONVERTER



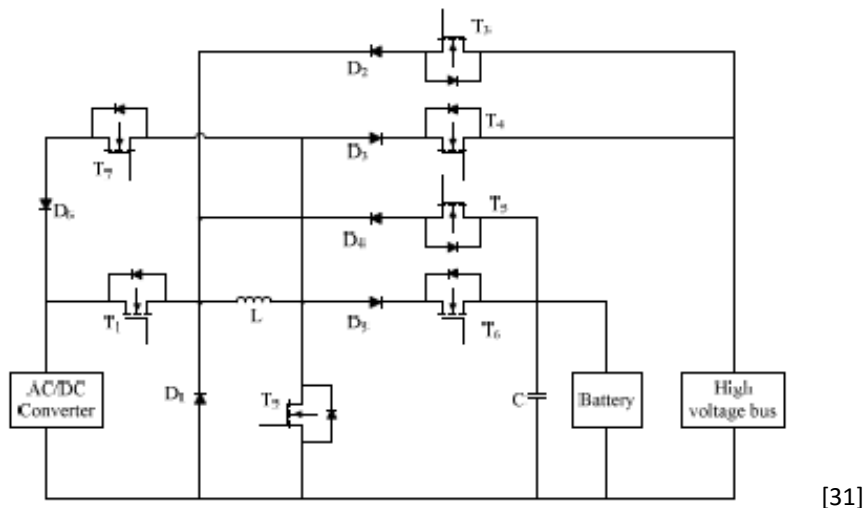
#### Advantages

Symmetrical structure [34]  
 Inherent low ripple current on both sides [34]  
 Only two switches (simple driver and control circuitry) [34]  
 Wide voltage range and voltage ratios [34]  
 Intrinsic protection against short circuit [34]

#### Disadvantages

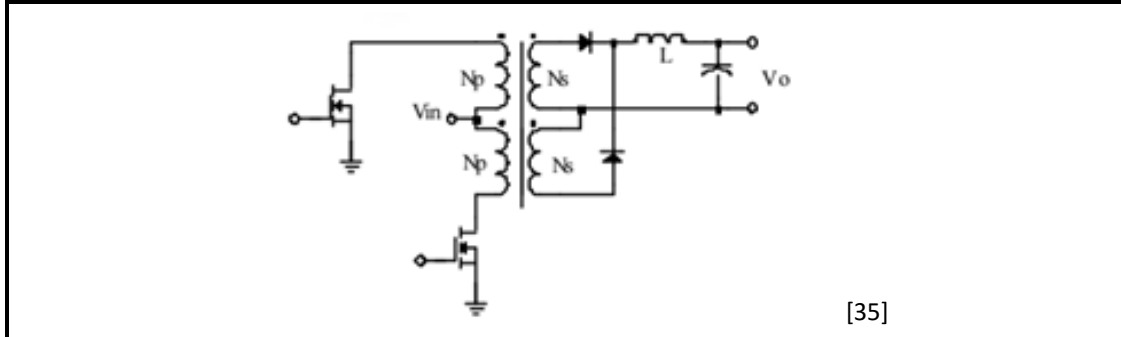
No galvanic isolation

### MODIFIED INTEGRATED BUCK-BOOST CONVERTER



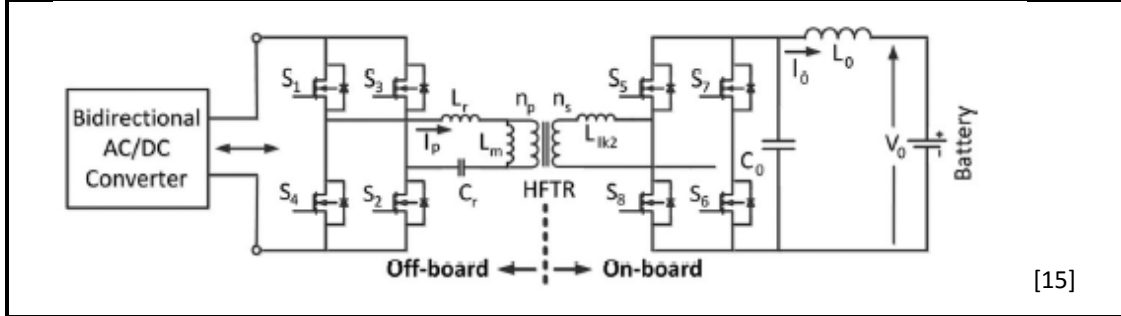
Advantages	Disadvantages
Less high current inductors [31] Added functionality [31]	Complexity [31] Additional switches (higher losses) [31] No galvanic isolation

**PUSH-PULL**



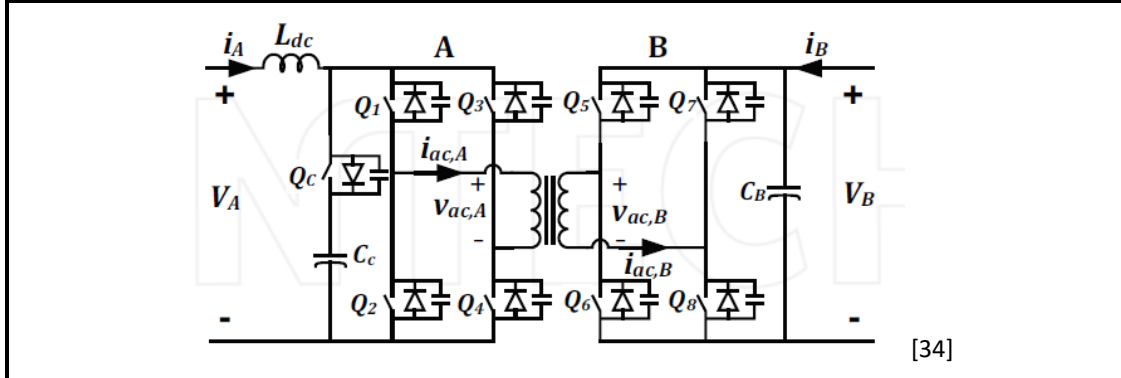
Advantages	Disadvantages
Galvanic isolation [35] Voltage Step-down or Step-up [35] Large Achievable Duty Cycle Range [35] Multiple Outputs Possible [35] Low Ripple Current [35]	Voltage Stress of the Primary Switches is $2 \cdot V_{in}$ [35] Smallest power capability [35] Few switches (less losses) [35]

**ISOLATED DUAL ACTIVE FULL BRIDGE (DAB)**



Advantages	Disadvantages
High power density [15][31] Fast and flexible control [15][31][36] Galvanic isolation [15] Use of transformer ratio [15] Fast dynamic behavior [34] No additional elements needed for soft switching [34]	A lot of components [15][31][34] More switching losses [31] Cost [15][31][34] High stress for voltage range bigger than 2:1 [31] Not for high voltage applications [36] High current ripple in dc bus; filtering necessary [34] No inherent dc current blocking capability [34]

**DAB WITH ACTIVE CLAMP**



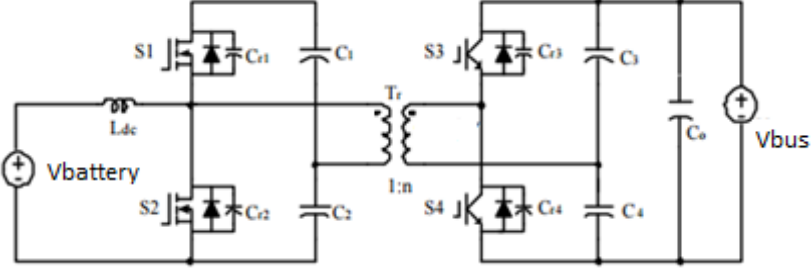
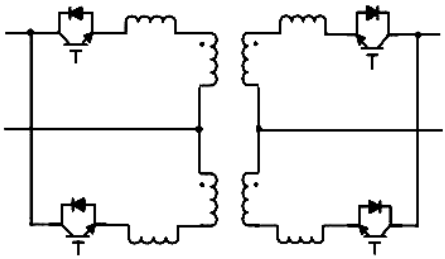
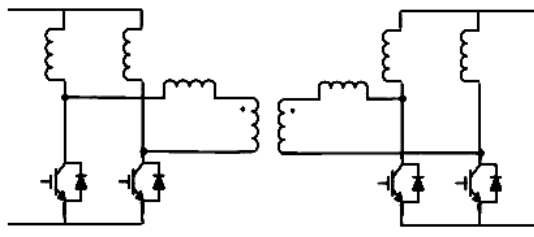
Advantages	Disadvantages
Limit the overshoots caused by transformer leakage inductance during current commutation [34] Inherent protection against over-current and short-circuit [34] Insensitive to transformer saturation [34] Relatively low-ripple current suitable for batteries [34]	Difficult start-up [34] High losses in high frequency due to transformer leakage inductance [34] Bulky input inductor [34] Need of high quality capacitors [34] Switches Voltage capability higher than $V_{bus}$ [34] Susceptibility to loss of gate drive which could lead to current interruption and large voltage spikes [34]
<b>ISOLATED DUAL HALF BRIDGE (DHB)</b>	
 <div style="text-align: right;">[37]</div>	
Advantages	Disadvantages
Half number of devices than DFB [34][37] High power density, efficient power conversion and compact packaging [37] Soft-switched (ZVS) with no elements addition [34][37] Less accessory power needs [37] Simple control [34] Low ripple current at the LV side desirable for the batteries [36]	Switches with double current stress than FB [36] LV side is subject to twice the dc input voltage than FB [37] Large ripple current in the splitting capacitors [34] Unbalanced current stress between two switches in the LV side [34]
<b>OTHER ISOLATED TOPOLOGIES</b>	
 <div style="display: flex; justify-content: space-around;"> <div style="text-align: center;">Push-pull</div> <div style="text-align: center;">Center-tapped</div> </div> <div style="text-align: center;">[36]</div>	 <div style="display: flex; justify-content: space-around;"> <div style="text-align: center;">L-type HB (V-fed only)</div> <div style="text-align: center;">Current Doubler</div> </div> <div style="text-align: center;">[36]</div>
<p style="text-align: center;">Galvanic isolation</p> <p style="text-align: center;">For low voltage high current applications due to the low current stress and high voltage stress of switches [36]</p> <p style="text-align: center;">Low amount of switches</p>	

Table 6. Comparison of DC-DC Converters for LV-Battery connection

### 2.2.3. Isolated and Resonant Structures

Nowadays, European Committees like CENELEC recommend the installation of a galvanic isolation between the grid and the local sources that use power converters, such as renewable generators or electric vehicles [38]. Normally this galvanic isolation is provided by a magnetic transformer [34], as seen in Figure 8, whose main characteristics are the following [12]:

- Advantages:
  - Provides galvanic isolation, which increases the personnel safety;
  - Ensures zero DC current, which prevents the saturation of the grid transformers;
  - Limits common mode currents, important for EMC regulation;
  - Enables a correct operation of the protection systems;
  - Provides voltage matching, needed to design and optimize the voltage rating of different stages in a system.
  
- Disadvantages
  - Large size and weigh;
  - High cost (the converter is 20% more expensive compared to non-isolated [12]).

Nonetheless, because of size and weight restrictions, regular Low Frequency (LF) transformers cannot be used for electric vehicle applications. Thus, High Frequency (HF) transformers are utilized instead, since the size of the transformer is inversely proportional to the operation frequency [12]. In addition, the electromagnetic interferences (EMI) are reduced [12].

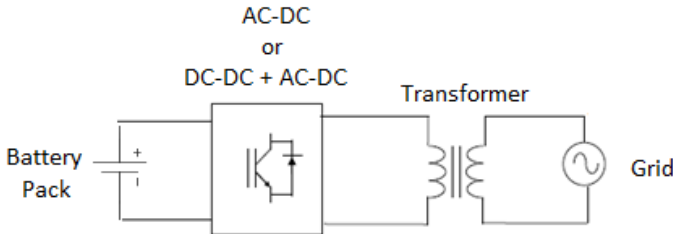


Figure 8. Converter with a LF Transformer [12]

On the other hand, even if this kind of transformers maintain the galvanic isolation, they cannot assure that the DC current delivered to the grid is zero. Besides, the final topology of the converter is more complicated, as described in [12], which can be seen in the example of Figure 9.

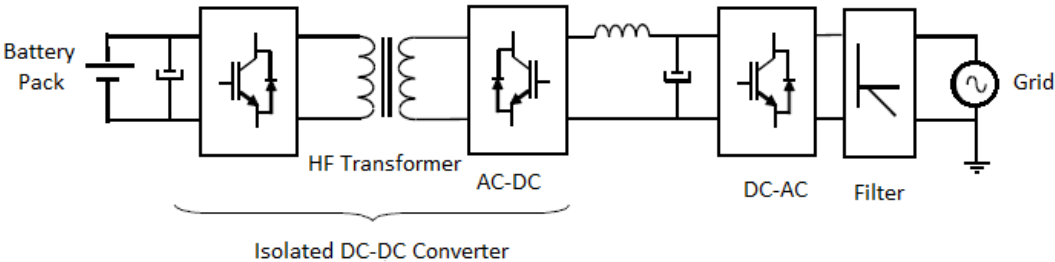


Figure 9. Converter with a HF Transformer [12]

An important disadvantage of having a high frequency system is that the commutation losses are very high. With the installation of a resonant structure, adding inductances and capacitors, these losses can be reduced. A certain resonant frequency, higher than the commutation frequency, can be obtained by choosing the values of the resonant tank's elements properly. This resonance enables the soft-switching of the transistors, since the commutation can be done with minimum losses when the current is zero (ZCS) or when the voltage is zero (ZVC). Depending on the resonant elements, there exist three different configurations [39]:

**1. Series Resonant Converter (SRC)**

The resonant tank of this configuration, as presented in [39], comprises a capacitor  $C_r$  and an inductor  $L_r$ , series connected to a resistor  $R_c$ , pictured in Figure 10.

This system is a Buck, given that a positive voltage drop is provoked by the resonant elements. The capacitive filter located at the output of this configuration produces a ripple than can be increased by high currents. Consequently, this structure is especially convenient for high voltages and low currents.

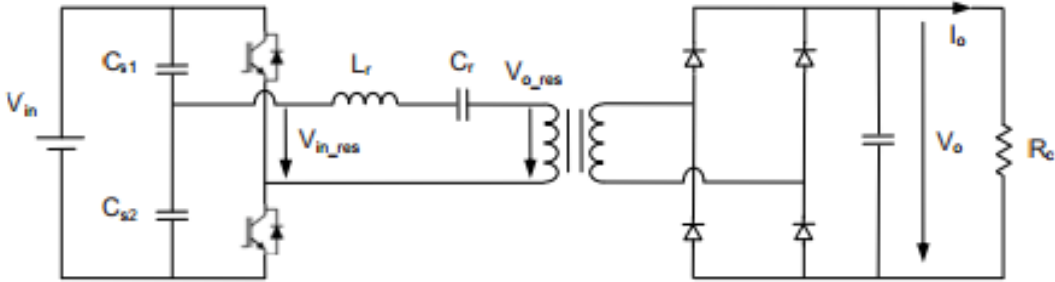


Figure 10. Series resonant converter [39]

**2. Parallel Resonant Converter (PRS)**

The resonant tank of this second structure, as described in [39], is composed by a resonant capacitor  $C_r$  and a resistor  $R_c$  connected in parallel, as seen in Figure 11:

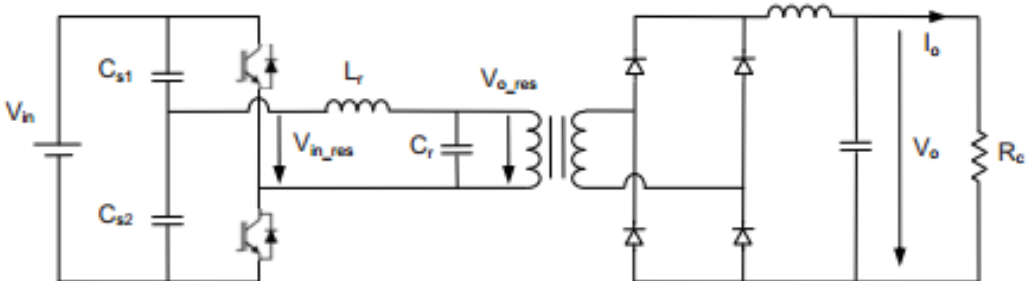


Figure 11. Parallel resonant converter [39]

This converter can be used as a Boost and as a Buck. Provided that the inductive filter is capable of reducing the current ripple, it is utilized for low voltages and high currents.

### 3. Series-Parallel Resonant Converter (SPRC)

The last configuration explained in [39] is built combining the previous ones. The resonant tank includes two resonant capacitors,  $C_{rs}$  and  $C_{rp}$ , one connected in series to the resistor  $R_c$  and the other connected in parallel, as depicted in Figure 12.

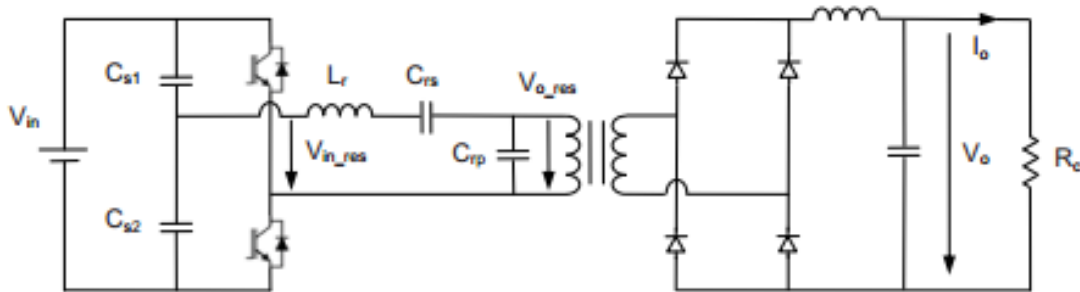


Figure 12. Series-Parallel resonant converter [39]

This structure can be utilized as a Boost or a Buck. In addition, its operation is more similar to the series or to the parallel configuration depending on the values given to the resonant elements. This flexibility makes the Series-Parallel structure be the most used resonant topology [39].

#### 2.2.3.1. AC/DC Converter with Galvanic Isolation

As mentioned before, one of the main disadvantages of using an AC/DC plus a DC/DC converters with HF transformer for galvanic isolation is the complexity of the final structure and the high amount of components used. In order to avoid this drawback, in [40] an isolated bidirectional single stage AC/DC converter is presented. As pictured in Figure 13, this structure comprises two Half Bridge circuits and a series resonant LC circuit. Only 6 switches are needed, gaining compactness and efficiency, as well as reducing the price compared to a conventional topology. Furthermore, ZVS is guaranteed using an adequate control method.

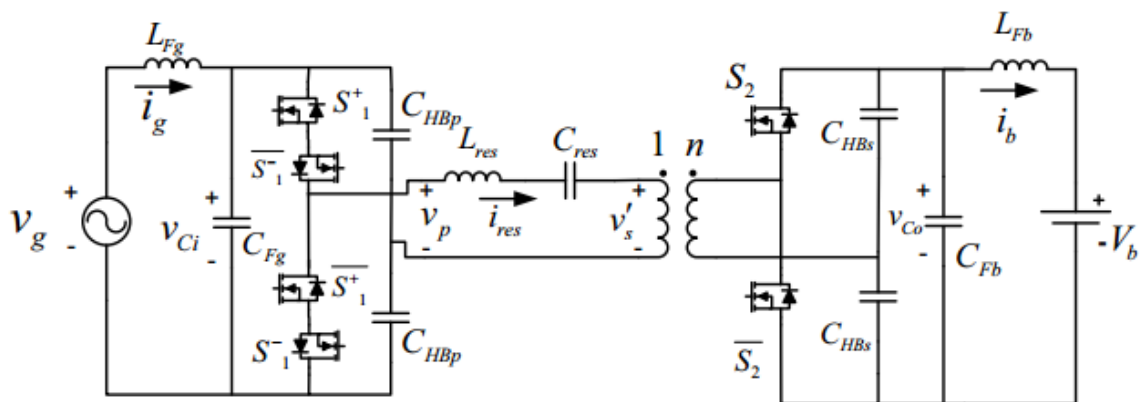


Figure 13. Isolated bidirectional single stage AC/DC converter [40]



### 2.3. Review of Control Methodologies for V2G and G2V Systems

The V2G technology can provide numerous benefits to the electricity grid as long as a good control is implemented, especially if a large number of Plug-in Electric Vehicles (PEVs) are connected. The charging management strategies reported in the literature are the following [41]:

- Dumb charging: the PEV is fully charged, at rated power, whenever it is plugged-in.
- Delayed charging: with the purpose of reducing electricity costs, there exists a time delay between the plug-in of the vehicle and the start of the recharge.
- Smart charging: the PEV is recharged based on the needs of both the owner and the grid operator with the aim of optimizing the charging process.

When dumb charging is implemented, the users can charge their PEVs at any moment, so this type of strategy can be considered as uncontrolled. In fact, it would be unviable to have a big amount of uncontrolled EVs connected to the grid, since they could be seen as a lot of generators and loads with an unknown and unexpected production and demand. Among others, the main impacts of this situation on the electricity grid's parties would be the following [7]:

- Generation and markets:
  - Increase of the use of peaking plants;
  - Increase of the reserve requirements;
  - Higher electricity prices;
  - Increase output of high CO<sub>2</sub> emissions plants.
- Transmission:
  - Congestions and overloads in the network.
- Distribution:
  - High risk of local constraints and overloads;
  - Need to reinforce the network;
  - Problems with harmonics.
- Consumer
  - Need for increasing the contracted power;
  - Possible need for reinforcement of the connection to the network;
  - Increase of electricity prices.

On the other hand, the delayed charging and the smart charging strategies can be performed either manually or automatically. In the first case, each owner can decide, based on reduced price electricity tariffs, when to recharge the batteries. In the second case, which mostly corresponds to smart charging operation, an active management system determines the charging profile to maximize both the economic and technical benefits for the electricity grid and the owners [41].

For this last intelligent charging, communication between the grid operator and the EV is essential so that the vehicle's battery is charged or discharged at the most convenient moment. Using smart grid technology and an intelligent battery recharging system managed by a computer, the V2G technology is able to monitor the status and needs of the grid at any moment [42].

Furthermore, a good control would bring the following opportunities to the system parties [7]:

- Generation and markets:
  - Shaping demand to reduce marginal cost of generation;
  - Reduction of price volatility;
  - Integration of intermittent generation;
  - Increase output of low CO<sub>2</sub> emissions plants.
  
- Transmission:
  - Support the Transmission System Operator (TSO) with congestion management;
  - Provide frequency regulation services.
  
- Distribution:
  - Management of Low and Medium Voltage networks constraints;
  - Reactive power support;
  - Decrease of the necessity of network reinforcement.
  
- Consumer
  - Reduction of their mobility cost by selling flexibility services;
  - Possibility of using EVs batteries to provide V2G services.

### **2.3.1. Battery Charging Methodologies**

When the battery charging process is being controlled, different charging and discharging methodologies can be considered. With the aim of optimizing the battery and converter performances, the most suitable method should be employed for each application [30]. Some charging methodologies are presented below. Among these techniques, the first three are the most utilized [43].

#### **1. Constant Voltage Charging (CV)**

This technique uses the value of the highest voltage (corresponding to the totally charged battery) during the whole charging process. The current is unconstrained, so at the beginning, its value is high and it decreases as the battery is charging. Using this technique the charging process is fast but it may provoke too high currents, as happened in [43]. These voltage and current can be seen in the following Figure 14.

The control of this methodology, as presented in [30], consists on a battery voltage control loop, in which a PI Controller maintains the battery voltage equal to the reference voltage (totally charged voltage). This loop generates the grid current reference for an internal and faster grid current control loop that establishes the switching patterns for the converter's switches. This reference current is synchronized to the grid voltage using a Phase Locked Loop (PLL). The block diagram of this control is depicted in Figure 15.

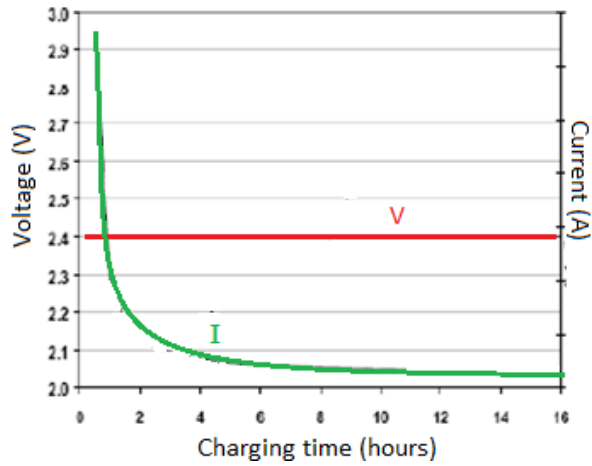


Figure 14. Battery current and voltage during CV Charging [43]

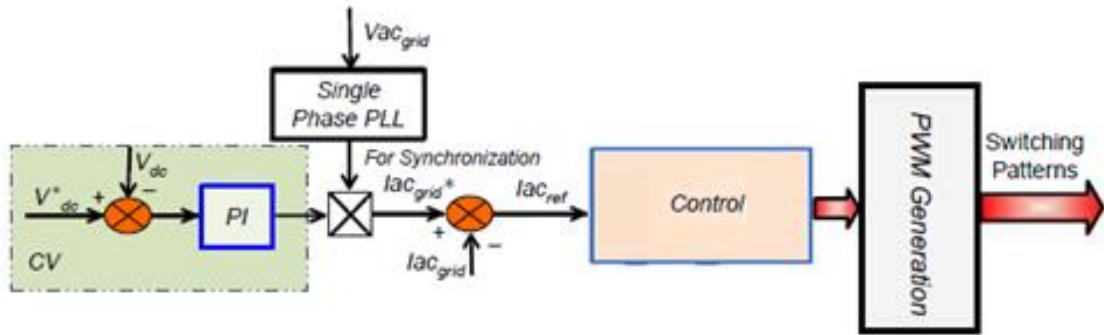


Figure 15. CV Charging block diagram [30]

## 2. Constant Current Charging (CC)

With this methodology, as explained in [43], the current applied is constant and the voltage increases while the battery charges, as pictured in Figure 16. If the battery's impedance is not zero, the battery does not totally charge.

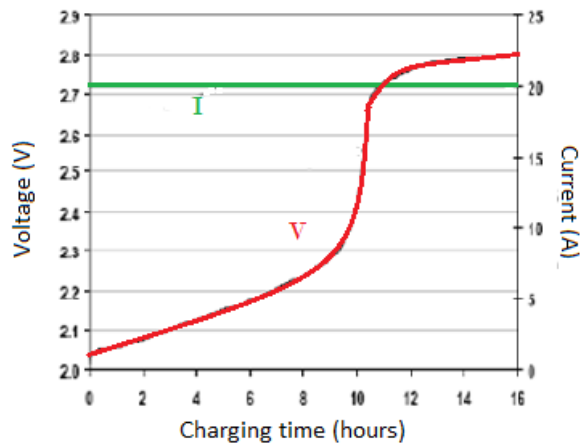


Figure 16. Battery current and voltage during CC Charging [43]

In [30], the control consists on a battery current control loop in which a PI Controller maintains the battery current equal to the reference current. As in the previous case, this outer loop generates the grid current reference for the inner grid current control loop that establishes the switching patterns. As before, the reference current is synchronized to the grid voltage using a PLL. The block diagram of this control is shown in Figure 17.

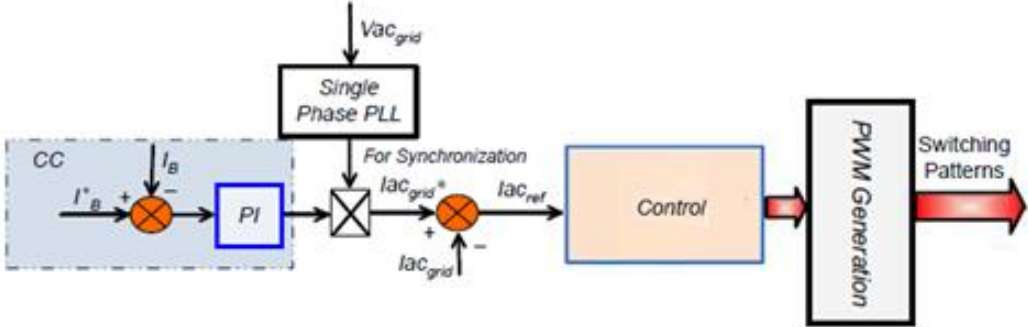


Figure 17. CC Charging block diagram [30]

**3. Combined charging CC-CV**

The combined CC-CV charging is the method commonly used for lithium batteries since it enables a complete charging without any overcharge [30].

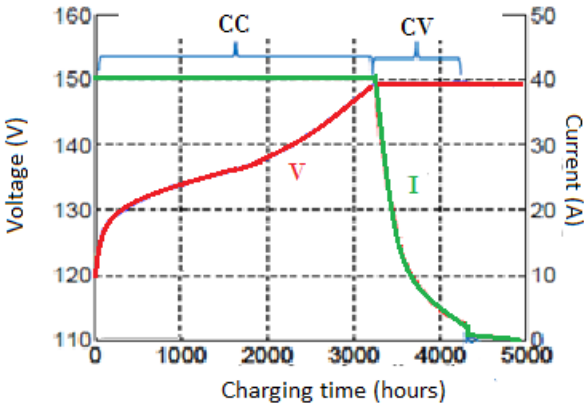


Figure 18. Battery current and voltage during CC-CV Charging [43]

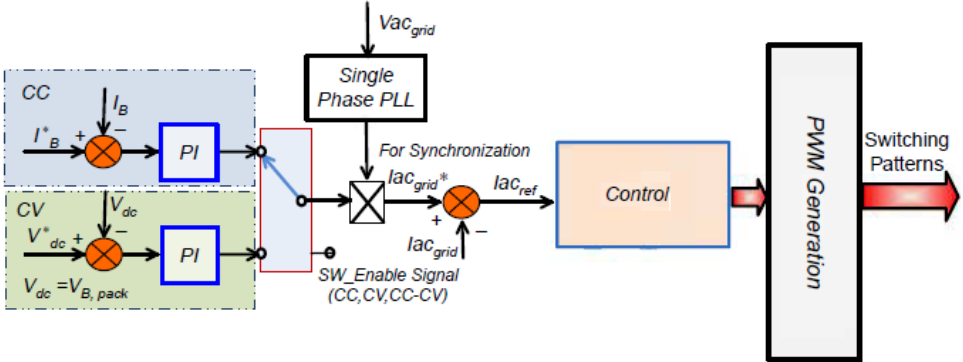


Figure 19. CC-CV Charging block diagram [30]

The first stage of this method, as described in [43], consists on CC charging until the voltage achieves its highest value. Once this value is reached, CV charging is done, maintaining the voltage at its maximum value while the current starts to reduce until it reaches a certain value for which the battery is considered totally charged. The battery current and voltage during this methodology are shown in Figure 18.

In [30], the control of this methodology consists on switching between the two previously introduced control loops depending on the charging mode desired at each moment. The block diagram of this control can be seen in Figure 19.

**4. Pulsing charging**

The Pulsing charging methodology, presented in [43], consists of charging the battery using short pulses of current. It is utilized for the simplicity of the rectifier converter of connection to the grid and for its fastness. However, it is not clear if this charging method decreases the life spam of the battery. The battery current and voltage during this kind of charging are shown in Figure 20.

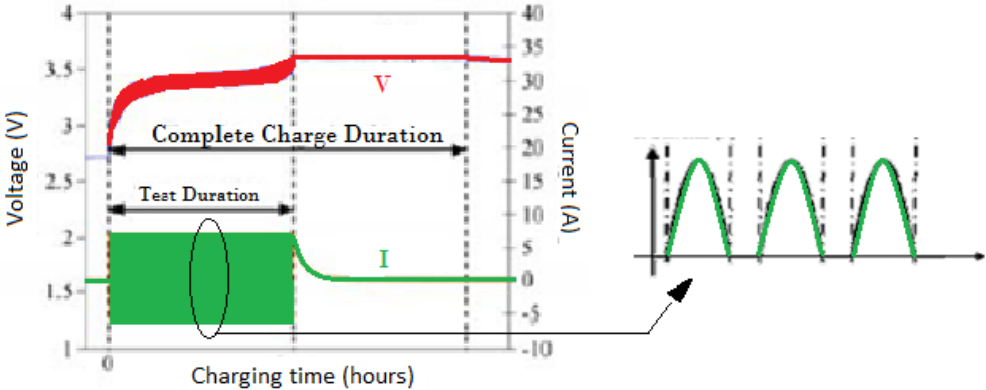


Figure 20. Battery current and voltage during Pulsing Charging [43]

**5. Reflex™ charging**

The Reflex™ charging method, explained in [44], is an improvement of the Pulsing charging in which a charging period consists on a positive pulse, a negative pulse and a relax interval. The current waveform of this kind of charging is plotted in Figure 21.

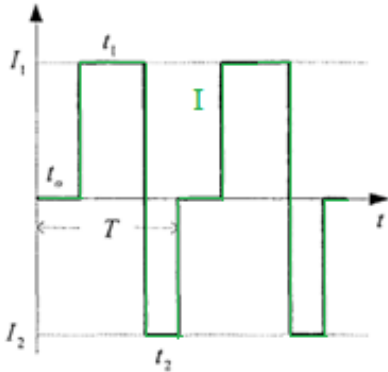


Figure 21. Battery current during Reflex™ Charging [44]

### 2.3.2. Control Techniques

The control of the previously described charging methodologies can be performed using different control techniques. These techniques are known as Vehicle-to-Grid control strategies, and as seen in Figure 22, they are responsible for the power flow management for charging (G2V) or discharging (V2G) operating modes, so it is important to choose the most adequate strategy for each application in order to achieve the converter’s best performance [29].

Three different strategies to control the grid current are going to be studied below: hysteresis current control (HCC), Proportional-Integral Control (PIC) and Proportional-Resonant Control (PRC). In all these cases, the reference RMS grid current for the loop is given by a previous voltage or current loop, depending on the charging methodology implemented.

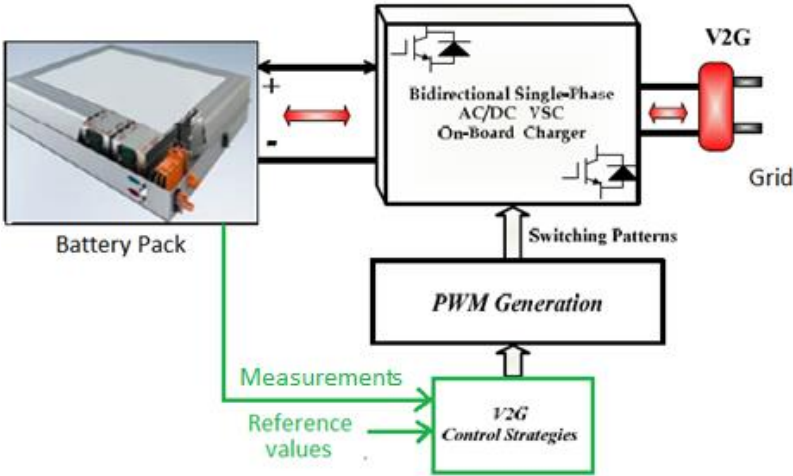


Figure 22. Diagram of the control and power flow in an on-board battery charger [29]

#### 2.3.2.1. Hysteresis Current Control (HCC)

The first control considered in [29] and [30] is the hysteresis-band current control. It is an instantaneous feedback current technique where the switching patterns are generated using a hysteresis band, whose input is the difference between the actual grid current and the reference grid current. This HCC block diagram can be seen in Figure 23.

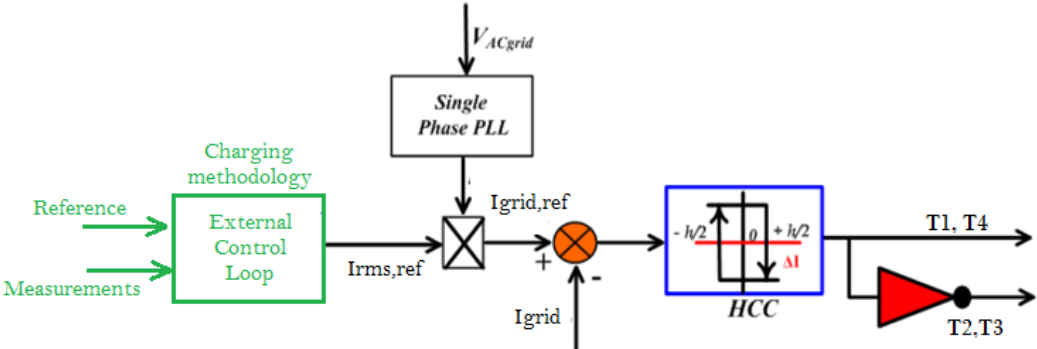


Figure 23. Block diagram of the HCC [29], [30]

As proved in [45], low frequency harmonics are satisfactory eliminated. Nevertheless, this strategy has variable switching frequency, which produces higher losses [30], [45].

A way of improving this strategy consists on implementing a variable hysteresis-band, dependent to the instantaneous reference current. Thus, high frequency harmonics are reduced and EMI Compatibility is more easily achieved [45].

### 2.3.2.2. Proportional-Integral Control (PIC)

The second control studied in [29] and [30] is the Proportional-Integral Control, which uses a PI Controller instead of the hysteresis-band controller. As this controller acts continuously, providing a control signal depending on the difference between the reference and the actual grid current, it is more accurate than the previous method. Furthermore, the switching frequency is constant and equal to the frequency of the triangular signal used for the Pulse-Width-Modulation (PWM). This fact improves the efficiency of the charger.

The block diagram of this control strategy is presented in Figure 24. The transfer function of the PI controller can be expressed as in equation (1), where  $K_p$  and  $K_i$  are the proportional and integral gains of the loop.

$$PI(s) = K_p + \frac{K_i}{s} \quad (1)$$

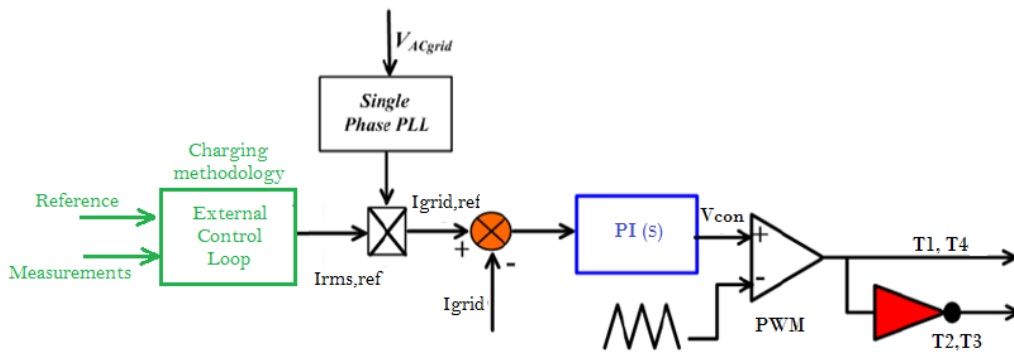


Figure 24. Block diagram of the PIC [29], [30]

The main problem of this controller is that it cannot do a perfect tracking of the reference. This is mainly due to both the delay introduced in the measurement and filtering of the actual signals and the incapability of the PI to eliminate a sinusoidal error, so it is not able to follow a sinusoidal reference accurately [46].

There exist two alternatives to overcome this drawback:

1. Controlling the grid current in d and q with a PI controller for each component (using Park and Clarke Transform) [46], [47].
  - When the reference frame of dq rotates with the grid frequency, the error is seen constant and the integral part can achieve a steady-state error equal to zero.

- In order to apply the Park Transform to a single-phase application, the d axis is orientated with a fictitious grid voltage (Voltage Orientated Control (VOC)).
- Its main disadvantage lies on its high computational cost.

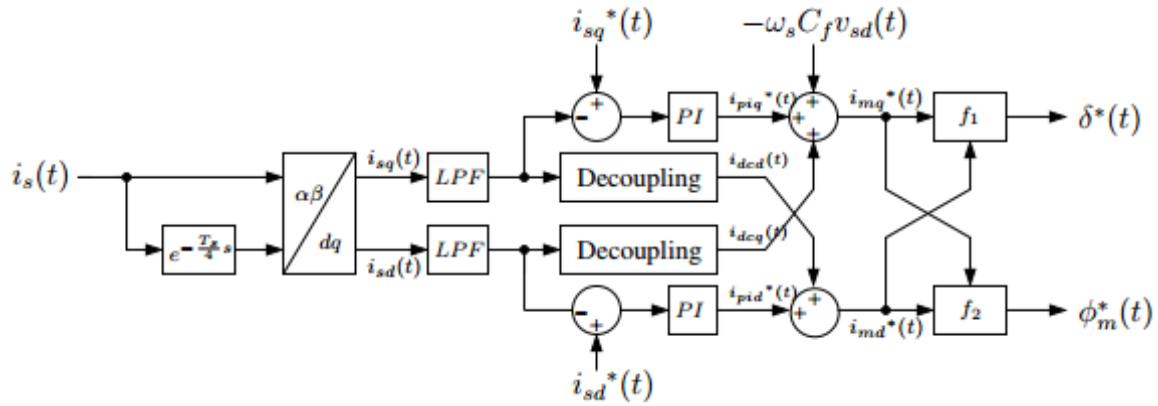


Figure 25. Block diagram of the DQ Control [47]

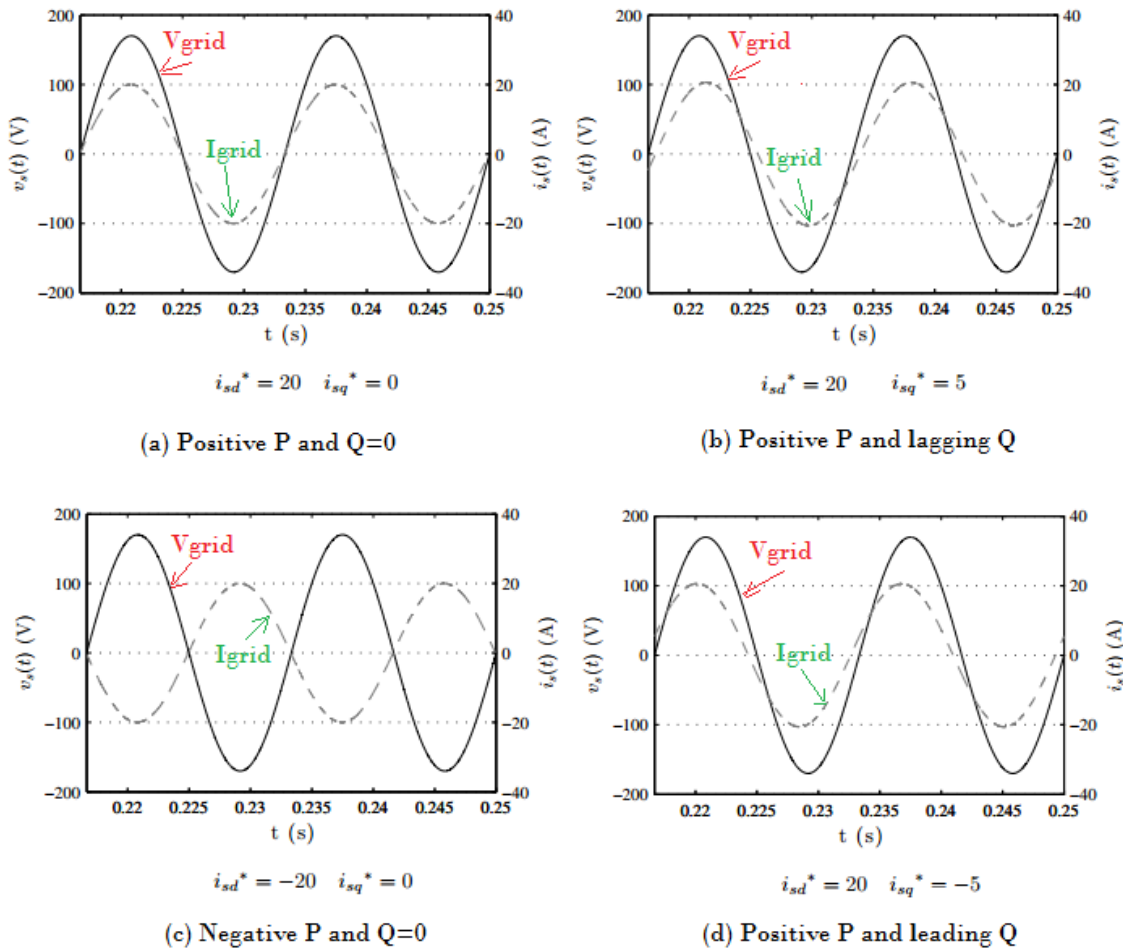


Figure 26. Grid current and voltage when DQ Control is applied [47]

A block diagram of this kind of control, proposed in [47], is seen in Figure 25. It is appreciated that the grid current is divided in two components:  $i_q$  and a fictitious  $i_d$ . Those currents are compared to



the reference currents and the respective errors are introduced in PI Controllers. The variables  $\delta$  and  $\phi_m$  control the magnitude and phase of the average current  $i_m(t)$ , following equation (2). This average current is proportional to the duty ratio. Furthermore, active and reactive power can be controlled with the reference d and q currents, respectively, as demonstrated in [47]. This is shown in Figure 26.

$$i_m(t) = K \cdot \delta \cdot \cos(\omega_s t + \phi_m) \quad (2)$$

2. Using a Proportional-Resonant Controller [46]: this is the last control strategy analyzed in the following lines.

### 2.3.2.3. Proportional-Resonant Controller (PRC)

The last strategy proposed in [29], [30] and [48] is a Proportional-Resonant Controller (PRC), whose block diagram is depicted in Figure 27. This controller is similar to a conventional PI, but with a theoretical infinite gain at a given resonant frequency, so that it can make the error at that frequency equal to zero, enhancing a good reference tracking. Furthermore, it is not necessary to compensate the grid voltage, so its implementation is really easy, as presented in [48].

The transfer function of the PR controller is expressed in equation (3), where  $K_p$  determines the dynamic response of the system,  $K_i$  adjusts the phase shift between the output and the reference signals and  $\omega_r$  is the resonant frequency [29], [30], [48].

$$PR(s) = K_p + \frac{2K_i s}{s^2 + \omega_r^2} \quad (3)$$

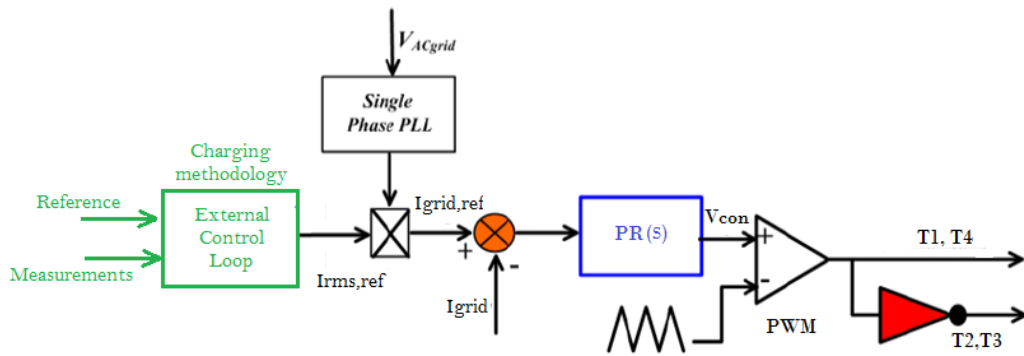


Figure 27. Block diagram of the PRC [29], [30], [48]

The Bode Plot of this controller was presented in [46], with a resonant frequency equal to the grid frequency (50 Hz), as shown in Figure 28. It can be seen that the gain at that frequency is infinite, while for the rest of frequencies the gain is unitary and the phase lag equal to zero.

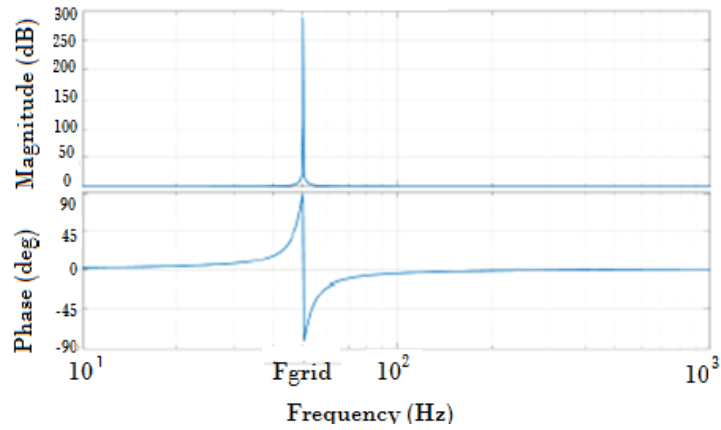


Figure 28. Bode Plot of the PR controller [46]

### 2.3.2.4. Comparison of the Control Techniques

In [29] and [30], a comparative study of the three control strategies has been performed. As seen in Figure 29, the PR controller is the most efficient, closely followed by the PI Controller. They also provide the grid current with less harmonic distortion than the HB Controller.

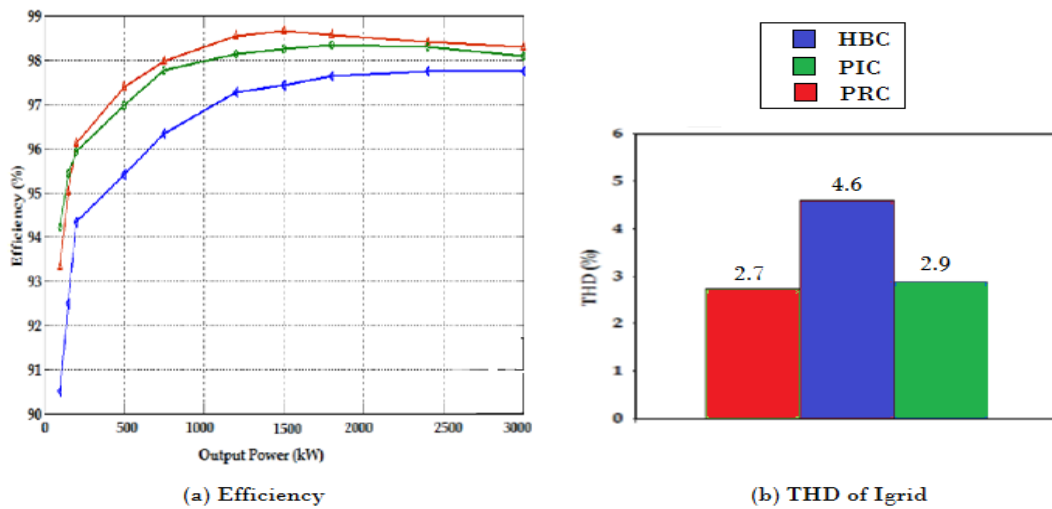


Figure 29. Comparison of the control strategies [29], [30]

### 3. DESIGN AND MODELING OF V2G AND G2V SYSTEMS AT DIFFERENT POWER LEVELS

Different Simulink models have been developed in order to evaluate the impact of the V2G and G2V operations on the electricity grid. In particular, a harmonics analysis has been performed based on the Total Harmonic Distortion (THD) of the AC current and voltage.

First of all, a low power application is analyzed. Two bidirectional single-phase 3.3kW chargers have been modeled: the first one consisting only on an AC/DC converter connected to High Voltage (HV) Batteries, and a second one counting with the addition of a DC/DC converter to connect to Low Voltage (LV) Batteries.

Afterwards, a high power application is studied, where two bidirectional three-phase 22 kW chargers are modeled. As in the previous case, the first topology consists on an AC/DC converter, while the second one counts also with a DC /DC converter.

#### 3.1. Topology 1: Full Bridge converter for Low Power applications

A bidirectional single-phase charger has been designed and modeled in the following lines. The choice of the topology utilized has been based on the topologies comparison stored in Table 5. After considering its benefits and drawbacks, a Full Bridge (FB) converter has been chosen thanks to its simplicity and good operation. As reported in [12], this converter is composed by two commutation branches, each comprising two complementary switches, T1-T2 and T3-T4. The distribution of these switches can be seen in Figure 30. This configuration has 4 different commutation states, stored in Table 7, whose combination will provide the desired output voltage wave form.

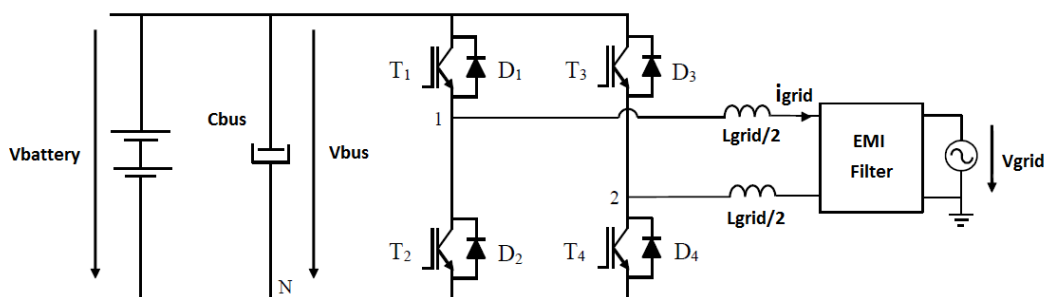


Figure 30. Single-phase FB converter [12]

State	T <sub>1</sub>	T <sub>3</sub>	v <sub>12</sub>
1	1	0	V <sub>bus</sub>
2	0	0	0
3	1	1	0
4	0	1	- V <sub>bus</sub>

Table 7. Commutation states of the FB [12]

Depending on the modulation technique used, different combinations of these states are achieved. The explanation of the main techniques is conducted in [12], whose main conclusions are stored in Table 8.

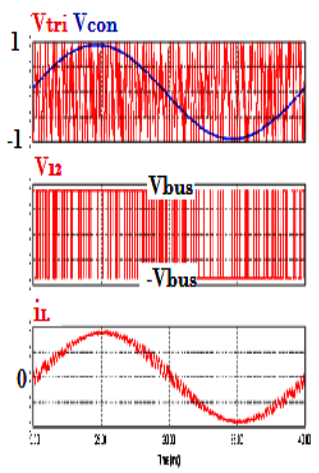
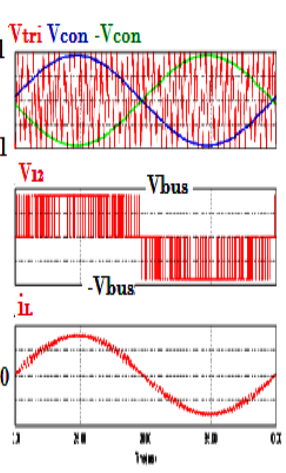
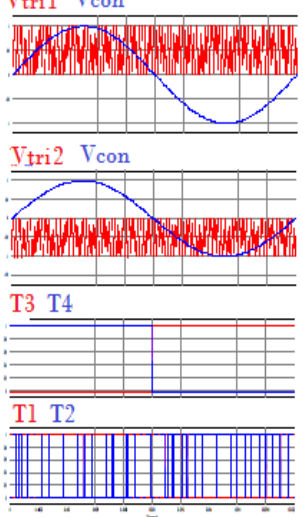
		BIPOLAR	UNIPOLAR	MODIFIED UNIPOLAR
PWM				
Differential mode		L	L/4	L/2
Vcm	One L	Vbus, Fc	Vbus, Fc	Vbus, Fgrid
	Divided L in two	Vbus/2, constant	Vbus, Fc	Vbus/2, fc
Losses	Conduction	ton	2 T	2 T
		toff	2 D	1 T, 1 D
	Commutation	2ETon, 2EToff, 2EDoff	2ETon, 2EToff, 2EDoff	1ETon, 1EToff, 1EDoff

Table 8. Comparison of the main modulation techniques for a FB converter [12]

The modulation used in these simulations is the bipolar for its simplicity, lower losses and constant common mode voltage when dividing the inductor in two. Nevertheless, the unipolar modulation was simulated also for the first developed model consisting on a FB for low power applications. The results of the different modulations are shown in Chapter 5.

The grid side's inductor is divided in two, since for bipolar modulation the common mode voltage is constant except for an oscillation at the grid frequency. Therefore the common mode currents are not very big and their ripple can be easily eliminated using a filter [12].

The model of this first system, implemented in this thesis, is shown in the following Figure 31. The parameters of the topology are calculated in the Appendix. The main results are stored in Table 9.

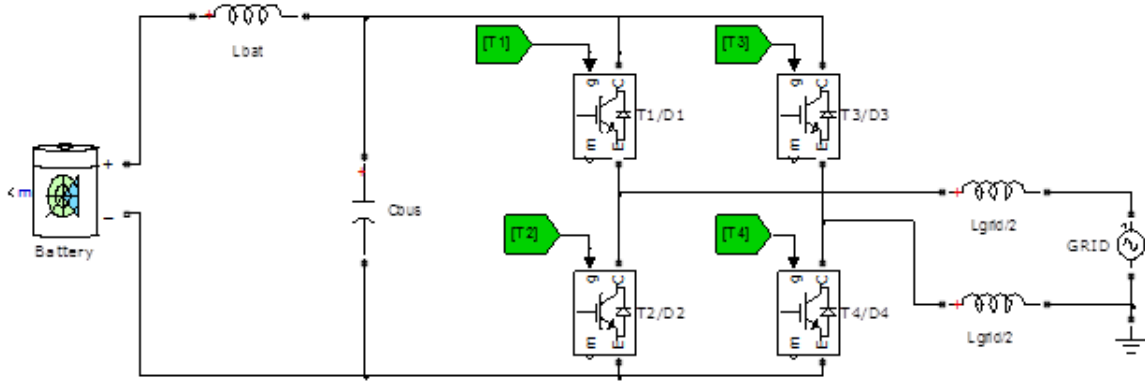


Figure 31. Simulink model of the FB for Low Power Applications

Converter		Battery		Grid	
Pmax	3.3 kW	Vcell	3.6 V	Vrms	230 V
Modulation	Bipolar	Ccell	10 Ah	Phase	Single
Vbus	400 V	Ns	102 cells	Fgrid	50 Hz
Lbat	10 mH	Np	1 string	$\Delta I_{max}$	10%
Cbus	42.3 mF			Lgrid	4.93 mH

Table 9. Main characteristics of the Low Power system connected to HV Batteries

### 3.2. Topology 2: Full Bridge and DC/DC converter for Low Power applications

The second topology studied consists on adding a Two-Quadrant converter to the Full Bridge (FB) in order to use Low Voltage (LV) Batteries. This kind of converter has been chosen because of its simplicity and easy control. The main characteristics of this converter are stored in Table 6.

In fact, the Two-Quadrant converter consists on having a unidirectional Boost or Buck converter in which the switches are bidirectional, composed by a transistor with a diode in antiparallel, as in [49]. The working elements, according to the direction of the power flow, are depicted in Figure 32. The two switches are complementary in order to avoid short circuits.

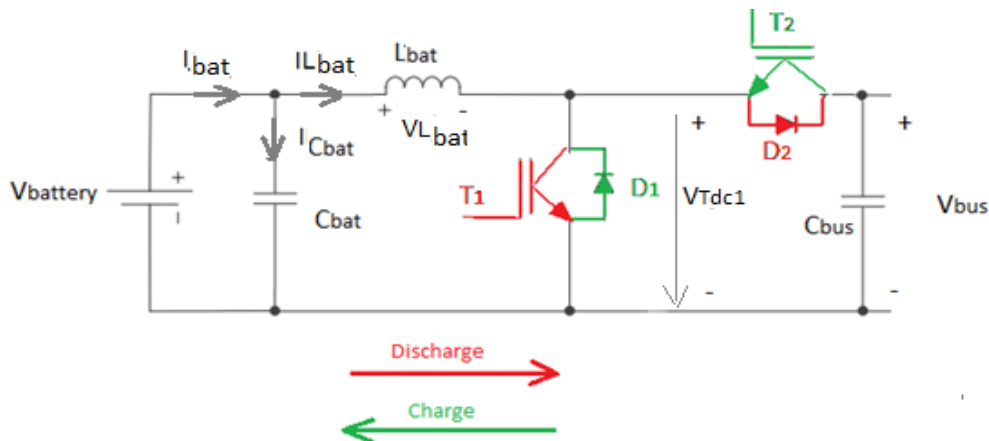


Figure 32. Two-Quadrant converter and its power flow [49]

During Discharge Mode the converter is a Boost, so T1 is being controlled while T2 is kept switched off; on the contrary, during Charge Mode the converter is a Buck, so T2 is being controlled and T1 is off.

In order to control the current of the battery, an inductor is needed. That way, lower current ripple is achieved, which is advantageous to charge/discharge batteries with higher efficiency and to maintain them in a good quality for a longer time [49].

On the other hand, only continuous conduction mode has been considered.

In the following Figure 33, the modeling of this second topology developed during this thesis, is depicted. This topology's main parameters are stored in Table 10. Their calculation is presented in detail in the Appendix.

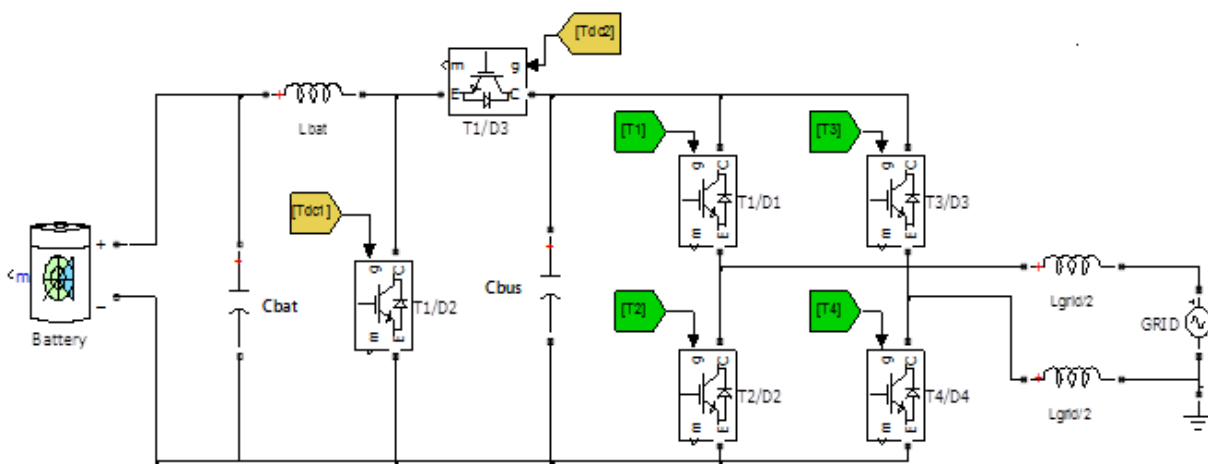


Figure 33. Simulink model of the FB and the Two-Quadrant converter for Low Power Applications

AC/DC Converter		DC/DC Converter		Battery		Grid	
Pmax	3.3 kW	Pmax	3.3 kW	Vcell	3.6 V	Vrms	230 V
Modulation	Bipolar	Vbat	150 V	Ccell	10 Ah	Phase	Single
Vbus	400 V	$\Delta V_{max}$	0.5 V	Ns	38 cells	Fgrid	50 Hz
$\Delta V_{max}$	2%	Cbat	0.557 mF	Np	3	$\Delta I_{max}$	10%
Cbus	3.28 mF	Lbat	1.136 mH			Lgrid	4.93 mH

Table 10. Main characteristics of the Low Power system connected to LV Batteries

### 3.3. Topology 3: Full Bridge converter for High Power applications

The system for high power applications comprises a battery charger of 22 kW. Therefore, the grid in this case has three phases. Again, the topology utilized is a Full Bridge (FB). However, as developed in [50], now the converter is composed by three commutation branches, whose respective complementary switches are: T1-T2, T3-T4 and T5-T6. The distribution of these switches, as well as the rest of the elements included in this system, are depicted in Figure 34.

The modulation is obtained in [50] using three different control signals, lagged 120°, and a common triangular wave, as seen in Figure 35. This method provides the minimum harmonic distortion.

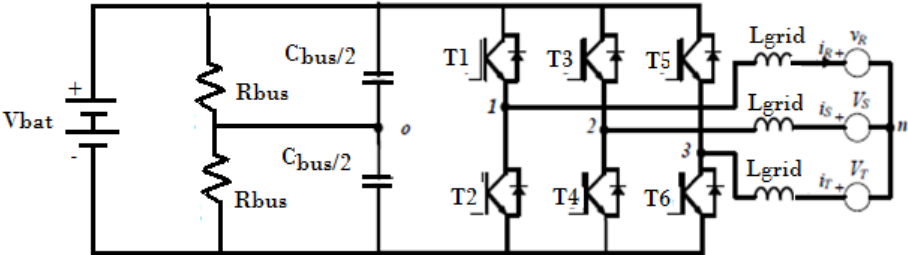


Figure 34. Three-Phase FB converter [50]

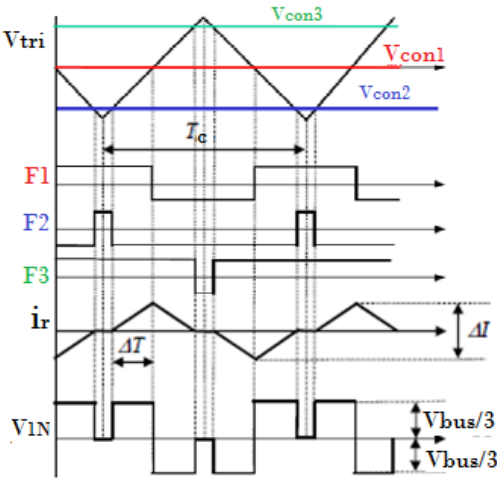


Figure 35. Control signals, switching orders, grid current and commutated voltage when the grid voltage crosses zero [50]

The previously introduced system was modeled during this thesis as shown in Figure 36. The parameters of this topology are calculated in the Appendix. The main results are stored in Table 11.

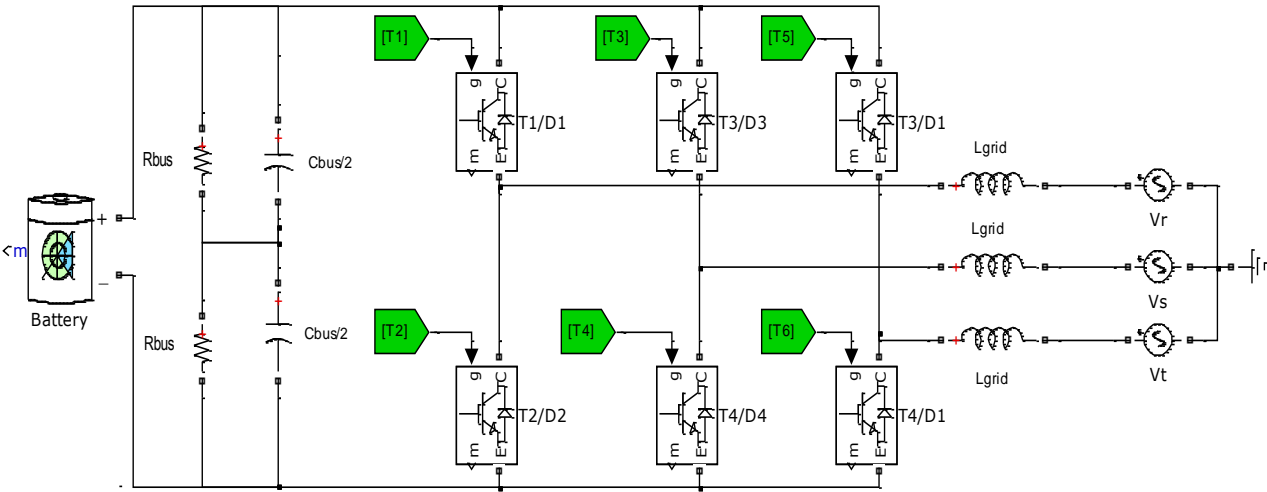


Figure 36. Simulink model of the FB for High Power Applications

Converter		Battery		Grid	
Pmax	22 kW	Vcell	3.6 V	Vrms,phase	230 V
Modulation	Unipolar	Ccell	10 Ah	Phase	Three
Vbus	700 V	Ns	178 cells	Fgrid	50 Hz
$\Delta V_{max}$	2%	Np	4 strings	$\Delta I_{max}$	10%
Cbus	2.494mF			Lgrid	1.1 mH
Rbus	286.4 k $\Omega$				

Table 11. Main characteristics of the High Power system connected to HV Batteries

### 3.4. Topology 4: Full Bridge and DC/DC converter for High Power applications

For using Low Voltage (LV) Batteries, the DC-Bus of 700 V has been connected to a Two-Quadrant converter, equal to the one introduced in Topology 3. The difference in this case lies on the values of the elements, which have to be resized to respect the actual constraints of the system. In the following Figure 37, the model developed in this thesis for the final converter is shown. The parameters of this topology are calculated in detail in the Appendix. The main results are stored in Table 12.

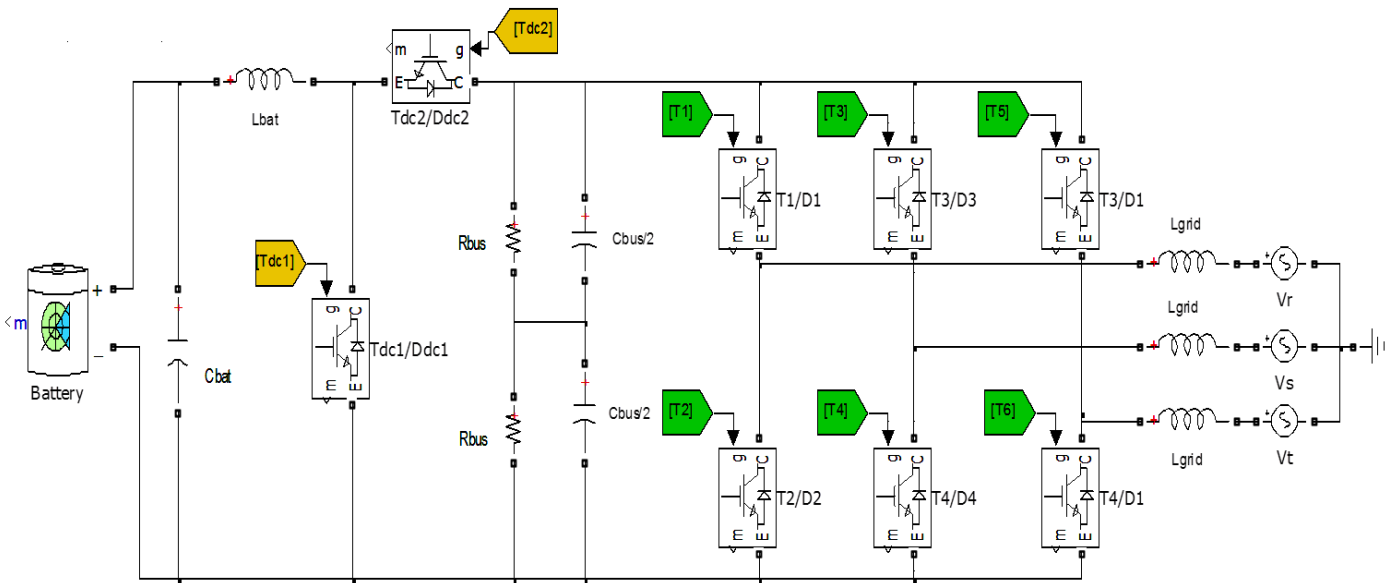


Figure 37. Simulink model of the FB and the Two-Quadrant converter for High Power Applications

AC/DC Converter		DC/DC Converter		Battery		Grid	
Pmax	22 kW	Pmax	22 kW	Vcell	3.6 V	Vrms,phase	230 V
Modulation	Unipolar	Vbat	150 V	Ccell	10 Ah	Phase	Three
Vbus	700 V	$\Delta V_{max}$	0,5 V	Ns	38 cells	Fgrid	50 Hz
$\Delta V_{max}$	2%	Cbat	0.133 mF	Np	17	$\Delta I_{max}$	10%
Cbus	2.494 mF	$\Delta I_{max}$	5%			Lgrid	1.1 mH
Rbus	286.4 k $\Omega$	Lbat	1.186 mH				

Table 12. Main characteristics of the Low Power system connected to LV Batteries



## 4. CONTROL DESIGN

It is essential to implement a good control strategy to achieve a correct behavior of the previously presented models developed in Matlab/Simulink Platform. The switches of the Full Bridge (FB) are controlled with a grid current loop, while the ones of the DC/DC converter are controlled using a battery current loop.

The grid current control loop is the one which orders how much current the system takes from or gives to the electricity grid. This control also establishes the lag between the grid voltage and current, depending on the power factor desired, which actually will be 1.

In the presented topologies, the reference current for this loop can be given using three different charging methodologies:

- Constant Current Charging: the user introduces the reference grid current manually. The direction of the power flow is decided depending on the sign introduced for the current. The current is measured positive when it exits the battery. Thus, a positive current is introduced to enable discharging mode, while a negative current enables charging mode.
- Constant Power Charging: given a desired reference power, the reference grid current is obtained:
  - Dividing the power by the grid RMS voltage for single-phase systems
  - Dividing the power by three times the grid phase RMS voltage for three-phase systems

For discharging mode, a positive value has to be introduced, whereas charging mode is enabled with a negative power.

- Constant Voltage Charging: a slower DC-Bus Voltage loop generates the reference current. This control loop is used to keep the DC-Bus Voltage at a value high enough so that the requested AC voltage can be supplied to the grid.

The battery current loop establishes the switching patterns for the Two-Quadrant converter, and that way it controls the current given to or taken from the battery. This control ensures that the battery current has no peaks and low ripple, which are beneficial for the battery's state of health (SoH) and efficiency [49]. In these models, the reference current for this loop can be given using three different charging methodologies:

- Constant Current Charging: the user introduces the reference current manually. As before, a positive current is used for discharging mode and a negative for charging mode.
- Constant Power Charging: given a certain power reference introduced by the user, the reference current is obtained dividing the reference by the battery voltage. Again, a negative power leads to charging mode while a positive power leads to discharging mode.

- Constant Voltage Charging: a battery voltage loop generates the reference for the current loop. That way, both the current and the voltage of the battery are controlled and constrained between safe values. The user decides the reference voltage of this loop. For charging mode, the reference introduced has to be higher than the battery voltage for the actual SoC, while for discharging the battery, this value has to be lower.

The first step in the design of a control strategy consists on simplifying the real systems to simple linear systems, to which the Classical Control Theory can be applied [46]. Afterwards, different tools can be utilized to analyse their stability and choose the parameters of the controllers. The main analysis techniques are the following [46]:

- Bode Plot of the open loop transfer function ;
- Root Locus of the poles of the closed loop transfer function;
- Nyquist diagram of the open loop transfer function.

The Bode Plot is the easiest and most often implemented technique. Thus, it has been used for the desing of the control models throughout this thesis.

As explained in [46], the Classical Control Theory defines two magnitudes to evaluate the stability of a system: the Phase Margin (PM) and the Gain Margin (GM). The PM is the difference between the phase of the system and  $-180^\circ$  at the cross-over frequency, which is defined as the frequency when the gain crosses the 0 dB value. The Band Width (BW) is the span of frequencies at which the control can operate correctly. On the other hand, the GM is the value of the gain at the frequency when the phase crosses the line of  $-180^\circ$ . It can be seen in Figure 38, where the Bode Plot of the open loop of a system is depicted, that a system is stable if both the PM and the GM are positive.

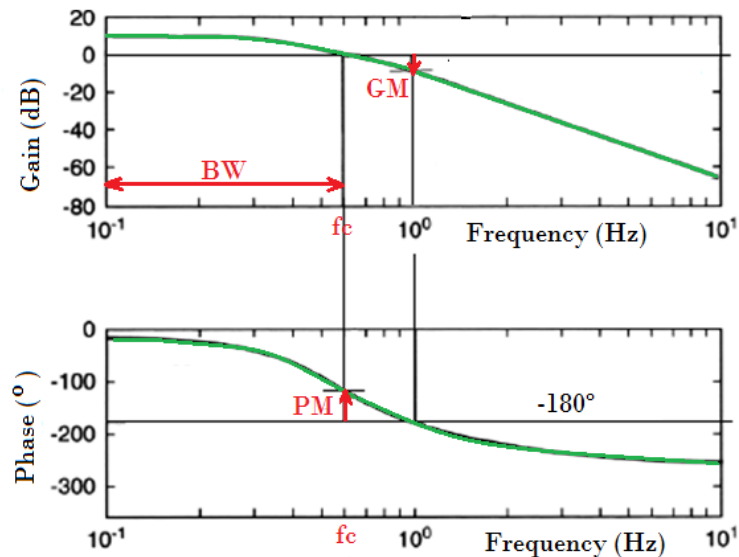


Figure 38. Bode plot with the PM, GM, Cross-over frequency and Band Width [46]

A controller must be added to every system in order to achieve the desired BW and PM. These parameters are inversely proportional, so it is important to find a compromise between velocity (BW) and stability (PM) [51].

## 4.1. Grid Current Control

In the State of Art Chapter (Chapter 2), different control strategies have been introduced in order to control the grid current of the system. Among them, the PI controller has been chosen thanks to its robustness, flexible implementation and easy design [46].

The block diagram of this control is pictured in Figure 39, as done in [46]; the digital part, where the control is implemented, is colored in red; the real part is in green. This loop operates as follows:

1. Given a certain grid current reference which is compared to the measured and filtered actual one, the PI controller provides the inductor voltage.
2. The grid voltage is going to be added. This is a way to compensate the grid voltage entering in the Plant of the converter. With this compensation, a better response and tracking is achieved.
3. The AC voltage  $V_{12}$  is obtained, and it is divided by the bus voltage to achieve the control voltage for the PWM. The advantage of dividing this signal by the DC-Bus voltage is that the loop is not affected by its changing value because it does not appear in the final transfer function.

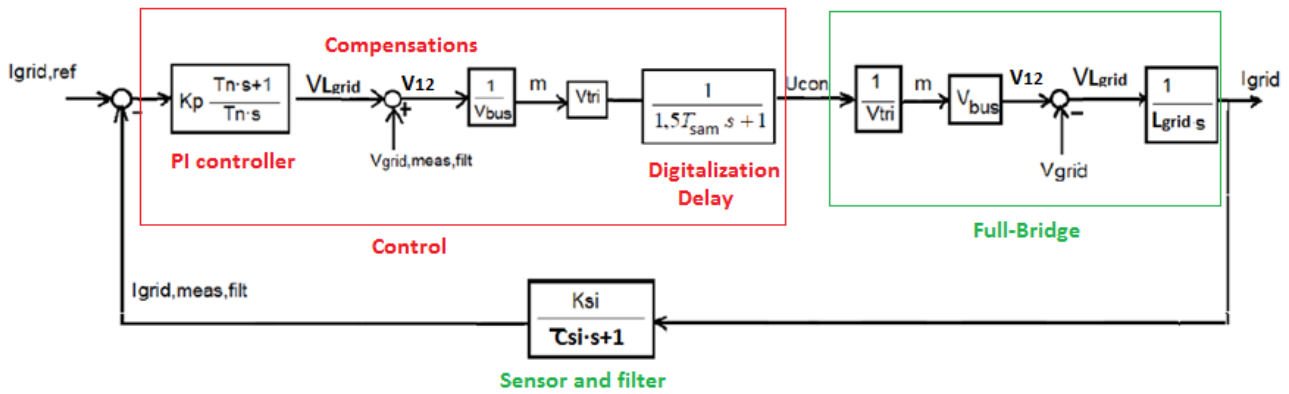


Figure 39. Block diagram of the Grid Current Control Loop [46]

In [46], the transfer function used to model the PI controller is presented in equation (4). The grid current is measured and filtered before being compared to the reference current. The transfer function of the sensor is shown in equation (5).

$$PI(s) = K_p + \frac{K_i}{s} = K_p \cdot \frac{T_n \cdot s + 1}{T_n \cdot s} \quad (4)$$

Where:

$K_p$  is the proportional constant. Its value affects to both the proportional and integral time.

$K_i$  is the integral part, which enables the reference tracking and zero error.

$T_n$  is the integral action time. It is the ratio of  $K_p/K_i$ , and its value settles the velocity of the control.

$$S(s) = \frac{K_{si}}{\tau_{si} \cdot s + 1} \quad (5)$$

Where:

$K_{si}$  is the current sensing constant, which is 1

$\tau_{si}$  is the current sensing time constant

The filter's frequency  $F_{si}$  established in the simulations is 3000 Hz. Consequently, the sensing time constant can be obtained using equation (6):

$$\tau_{si} = \frac{1}{2\pi \cdot F_{si}} = 53 \mu s \quad (6)$$

The plant of the system is the FB converter, whose transfer function was obtained in [46]. It is shown in equation (7). In these models, the Triangular wave for the PWM has a height of  $\pm 1$  V, and consequently the control voltage is limited between 1 and -1 V. The frequency of this triangular wave settles the commutation frequency, which in this case is 20 kHz.

$$B(s) = \frac{V_{bus}}{V_{tri}} \cdot \frac{1}{L_{grid} \cdot s} \quad (7)$$

The control has been implemented digitally, in Z domain. Nonetheless, in order to calculate the parameters of the controller, it is transformed to Laplace domain. In [52], the digitalization effect is modeled with a delay, a sampler and a Zero Order Holder (ZOH), as the ones shown in Figure 40. If the cross-over frequency of the loop is at least 20 times smaller than the sampling frequency [52], the transfer function of the digitalization can be reduced to equation (8). As decided based on the Stability and Velocity Study performed below, the cross-over frequency of the current loop is 1000 Hz. The sampling frequency chosen is 20 kHz, so this simplification can be applied. The transfer function of the whole system, in open loop, is expressed in equation (9).

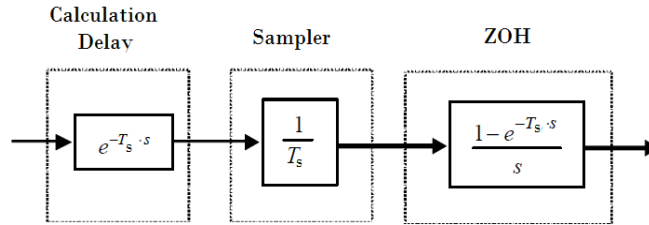


Figure 40. Model of the digitalization in S Domain [52]

$$D(s) = \frac{1}{1.5 \cdot T_s \cdot s + 1} \quad (8)$$

$$L(s) = K_p \frac{T_n \cdot s + 1}{T_n \cdot s} \cdot \frac{1}{L_{grid} \cdot s} \cdot \frac{K_{si}}{\tau_{si} \cdot s + 1} \cdot \frac{1}{1.5 \cdot T_s \cdot s + 1} \quad (9)$$

The previous control loop corresponds to the single-phase system used in low power applications. When high power is required and the system used comprises three phases, each phase must be controlled separately. In fact, when the neutral point is isolated, as assumed in [50], the three phases are coupled and the commutation of one branch affects to the current of the three phases. That is why the voltage of one phase, as in equation (10), is expressed as a function of three control signals  $f_1$ ,  $f_2$  and  $f_3$ , obtained using equation (11) [50].

$$\langle v_{1n} \rangle = \frac{V_{bus}}{6}(2f_1 - f_2 - f_3) = V_{bus} \cdot x_1 ; \quad \langle v_{2n} \rangle = \frac{V_{bus}}{6}(2f_2 - f_1 - f_3) = V_{bus} \cdot x_2 ; \quad \langle v_{3n} \rangle = \frac{V_{bus}}{6}(2f_3 - f_1 - f_2) = V_{bus} \cdot x_3 \quad (10)$$

$$f_i = \frac{v_{coni}}{V_{tri}} \quad (11)$$

For the purpose of using an independent control variable for each phase, the transform functions  $x_1$ ,  $x_2$  and  $x_3$  are defined in [50], as shown in equation (12). Actually, only two of the phase currents can be controlled independently, while the third one is constrained and obtained using the transform functions of the other two, as in equation 13. The loops of the two controlled currents are shown in Figure 41.

$$x_1 = \frac{(2f_1 - f_2 - f_3)}{6} ; \quad x_2 = \frac{(2f_2 - f_1 - f_3)}{6} ; \quad x_3 = \frac{(2f_3 - f_1 - f_2)}{6} \quad (12)$$

$$x_3 = -(x_1 + x_2) \quad (13)$$

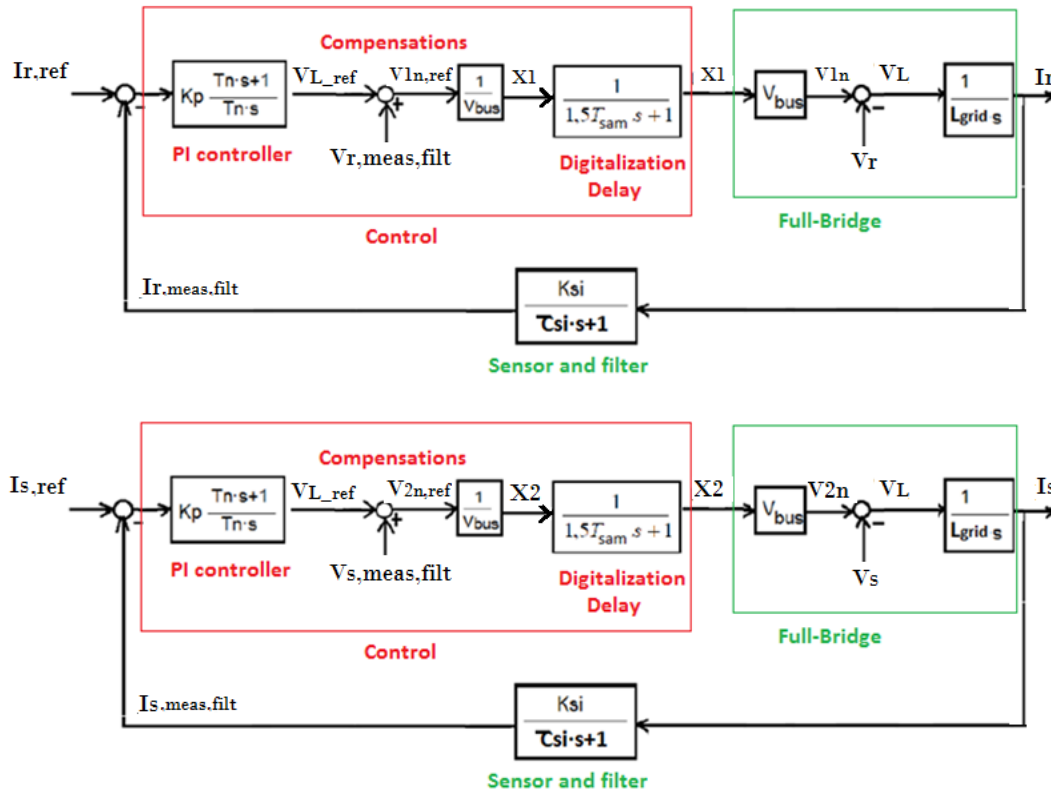


Figure 41. Block diagrams of the phase current control loops for 3-phase systems [50]

Once the transform functions are obtained, the control signals must be calculated. There exist infinite solutions, so in this case the following equation (14) has been used, as proposed in [50]. The maximum phase voltage obtained with this technique is  $V_{bus}/2$  and consequently the values of the transform functions must be constrained between  $\pm 0,5$ .

$$f_i = 2 \cdot x_i \quad (14)$$

#### 4.1.1. Stability and Velocity Study

For the purpose of deciding the optimal values for the PI controller, the Bode Plots, Step responses and Root Locus of the system for different cross-over frequencies and PMs have been realized.

Firstly, the system has been evaluated for a PM equal to  $45^\circ$  and three different frequencies: 1200 Hz, 1000Hz and 500 Hz. In Figure 42, it is proved that for higher frequencies than 1000 Hz the loop becomes unstable because it has one pole in the right hand plane. On the other hand, comparing the Bode Plots of the two stable systems, it can be seen that the area below the phase and  $-180^\circ$  is bigger for 1000 Hz. Thus, using this cross-over frequency, it is more certain that the system will be stable even if its values change slightly over time.

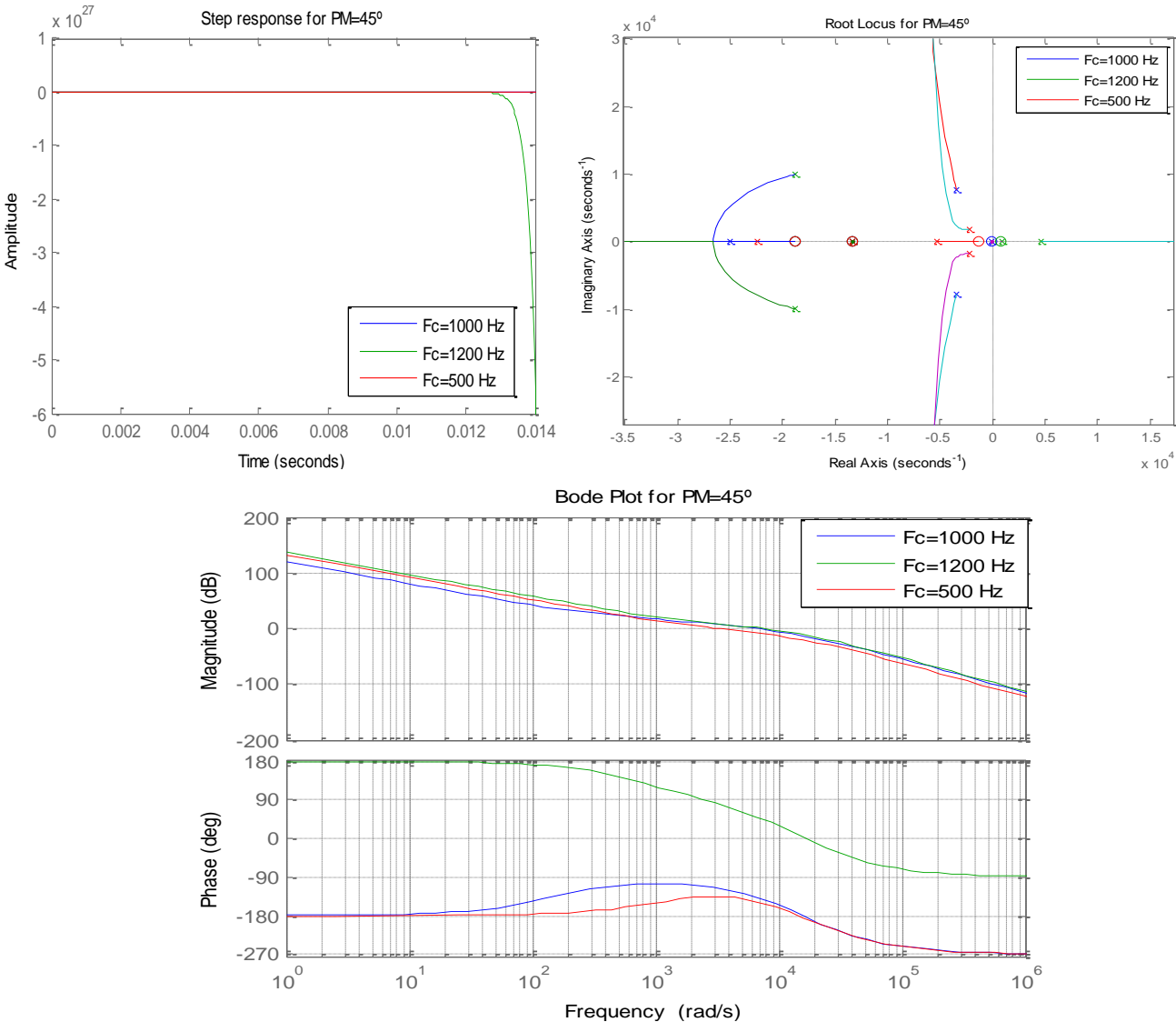


Figure 42. Step response, Root Locus and Bode Plots of the Grid Current control system for a PM of  $45^\circ$  and cross-over frequencies of 1200, 1000 and 500 Hz

Afterwards, the system has been tested for frequencies lower than 1000 Hz. The resulting plots can be seen in Figure 43. The data taken from the step responses is stored in Table 13. The fastest response and lowest overshoot is obtained for a cross-over frequency of 1000 Hz. Thus, it has been the chosen one for the developed models in this thesis.

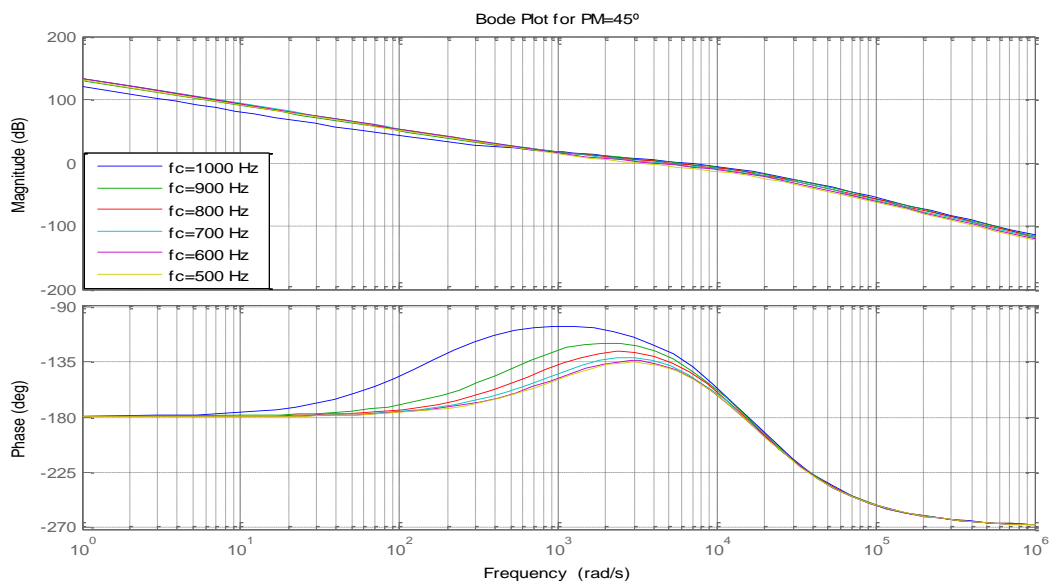
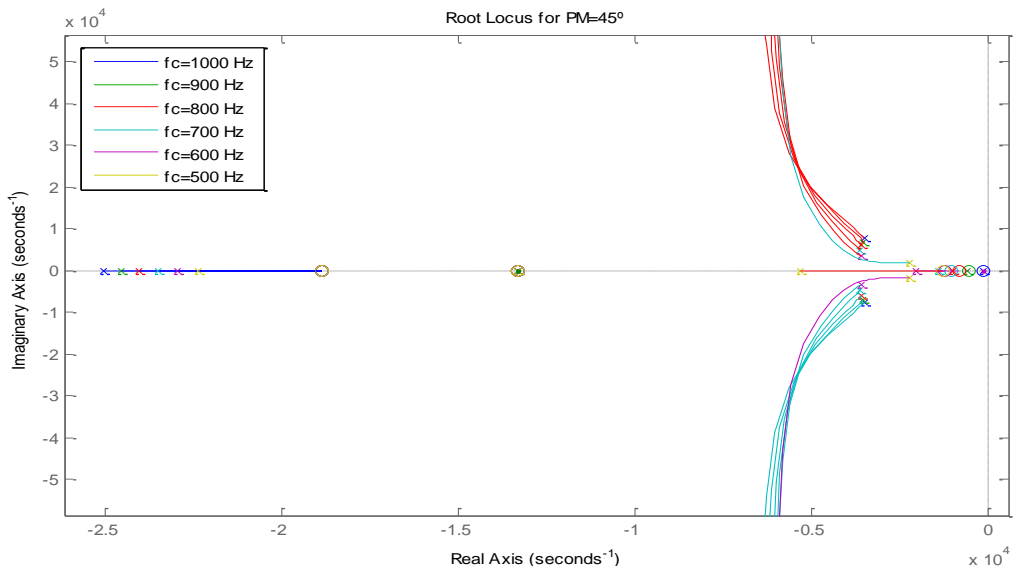
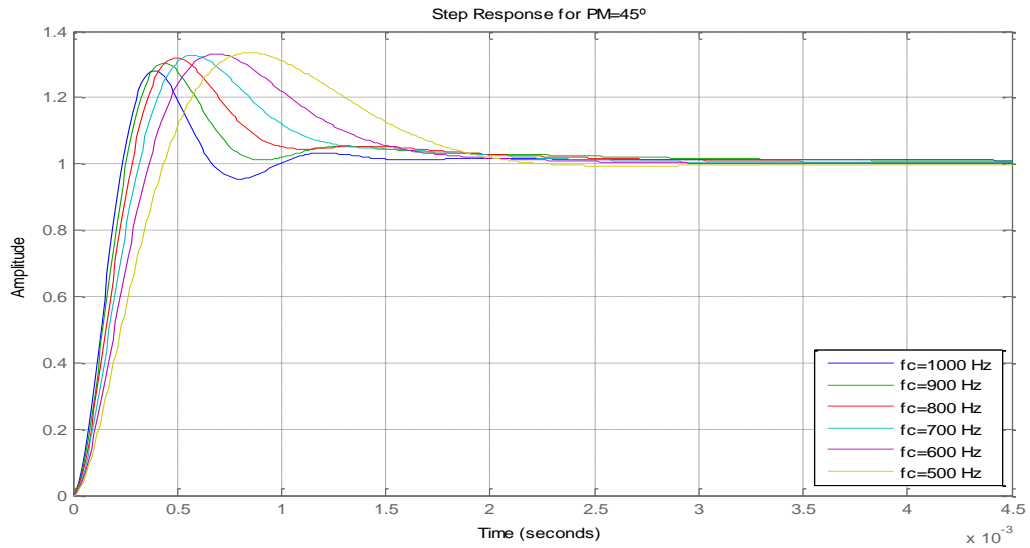


Figure 43. Step response, Root Locus and Bode Plots of the Grid Current control system for a  $PM$  of  $45^\circ$  and cross-over frequencies from 500 to 1000 Hz

Once the cross-over frequency has been chosen, different PMs have been tested. First of all, the values chosen are 40°, 45° and 50°. The plots resulting from this analysis are shown in Figure 44. The maximum PM which can be used is 45°, because for higher PMs the system has a pole in the right hand plane and becomes unstable. Afterwards, some PMs that make the system stable have been tested in order to choose the most suitable one. The results of this second test are depicted in Figure 45. Table 14 includes the values of the step responses for these PMs. From these results, it is deduced that the highest is the PM, the better response is achieved. Thus, the chosen PM for the models is 45°.

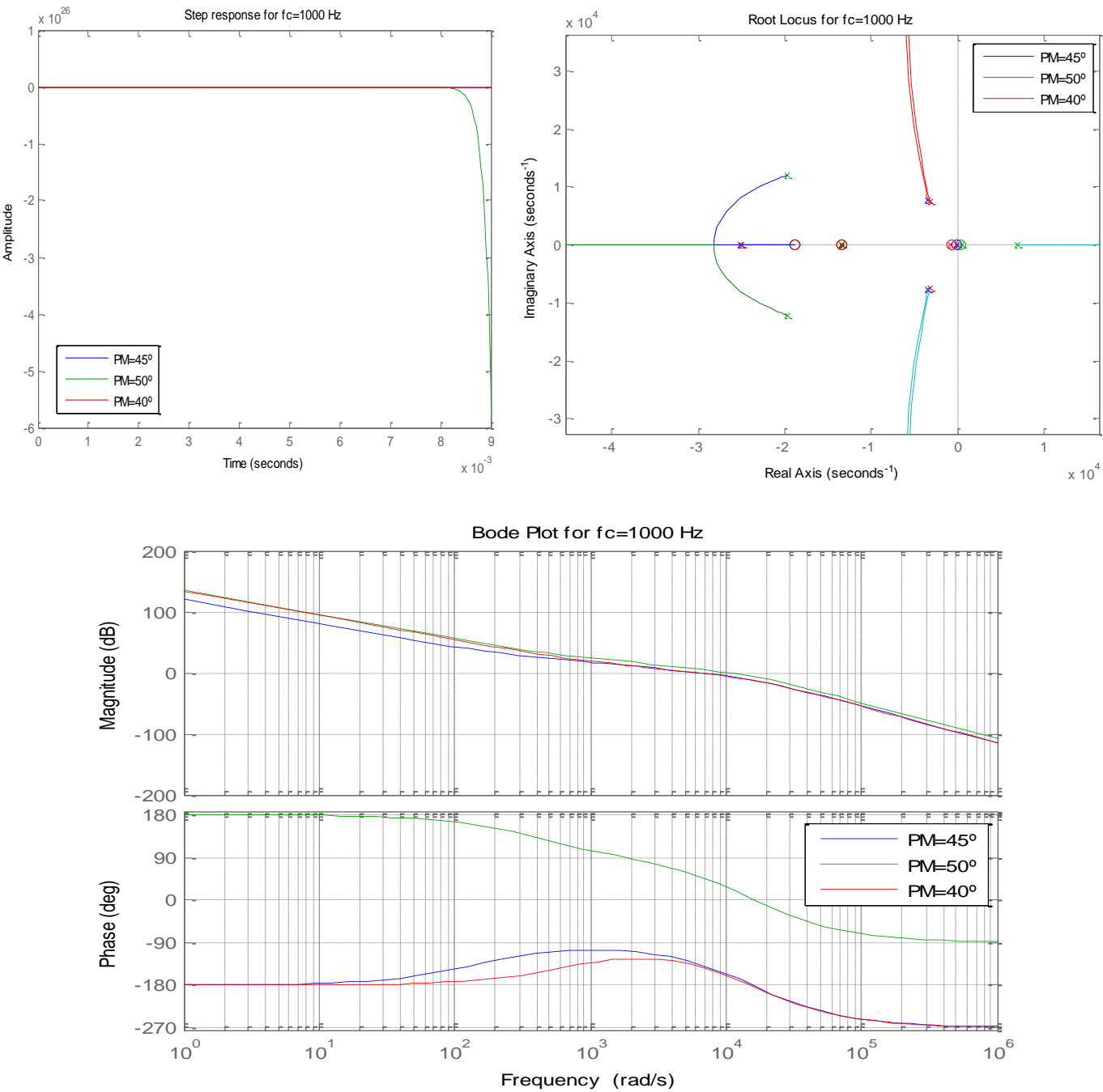


Figure 44. Step response, Root Locus and Bode Plots of the Grid Current control system for different PM and a  $F_c = 1000$  Hz



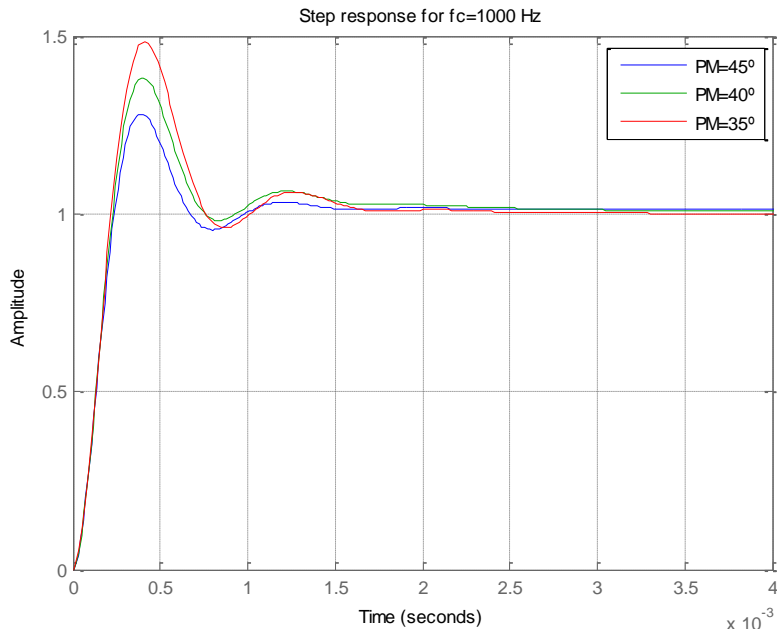


Figure 45. Step response of the Grid Current control system for  $f_c=1000$  Hz and different PM

PM = 45°						
Fc	1000 Hz	900 Hz	800 Hz	700 Hz	600 Hz	500 Hz
Rise Time	<b>0.1626 ms</b>	0.1762 ms	0.1939 ms	0.2187 ms	0.2532 ms	0.3045
Settling Time	<b>1.4 ms</b>	2.7 ms	2.4 ms	2.2 ms	1.9 ms	2 ms
Overshoot	<b>28.08</b>	30.39	31.94	31.81	33.26	33.55
Peak Time	<b>0.3916 ms</b>	0.4311 ms	0.4979 ms	0.5782 ms	0.6869 ms	0.8484 ms

Table 13. Information of the Step response of the Grid Current control system for a PM of 45°

Fc=1000 Hz			
PM	35°	40°	45°
Rise Time	0.1502 ms	0.1552 ms	<b>0.1626 ms</b>
Settling Time	1.6 ms	2.3 ms	<b>1.4 ms</b>
Overshoot	48.27	38.33	<b>28.08</b>
Peak Time	0.4146 ms	0.4071 ms	<b>0.3916 ms</b>

Table 14. Information of the Step response of the Grid Current control system for a cross-over frequency of 1000 Hz

#### 4.1.2. Modeling of the Grid Current control

During this thesis, various controls have been designed and modeled in Matlab/Simulink. For low power applications, the control of the grid current is conducted using the model developed in Figure 46. On the other hand, the model for high power applications, when the system comprises three phases, is seen in Figure 47.

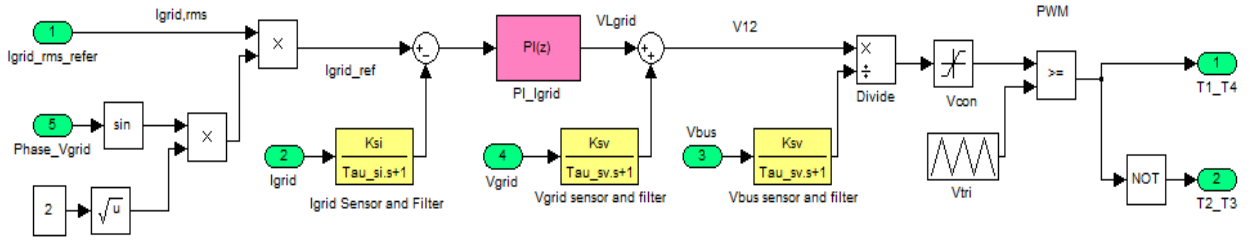


Figure 46. Simulink model of the grid current control for Low Power Applications

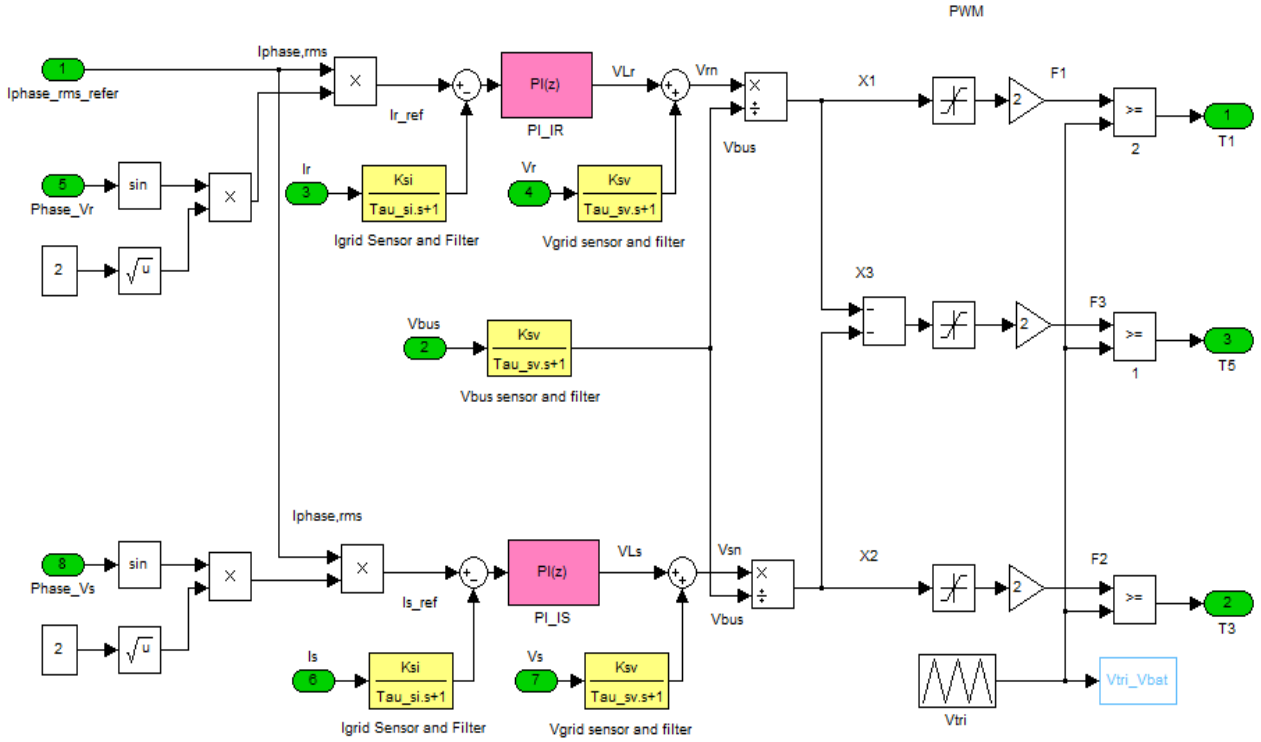


Figure 47. Simulink model of the Grid Current control loops for High Power Applications

#### 4.1.3. PI Parameters Calculation

Given the Phase Margin of  $45^\circ$  and crossover frequency of 1000 Hz, the PI parameters are calculated below. The  $T_n$  parameter is obtained from equation (15), which calculates the PM of the system. Equation (16) expresses the gain of the system, and  $K_p$  can be obtained from it. Finally,  $K_i$  is calculated using equation (17). The values of these parameters are stored in Table 15.

$$PM = 45^\circ = \arctg(T_n \cdot \omega_{ci}) - \arctg(\tau_{si} \cdot \omega_{ci}) - \arctg(1.5 \cdot T_{sam} \cdot \omega_{ci}) \quad (15)$$

$$|L(j\omega_{ci})| = 1 = \frac{K_p \cdot K_{si}}{T_n \cdot L_{grid} \cdot \omega_{ci}^2} \sqrt{\frac{(T_n \cdot \omega_{ci})^2 + 1}{((\tau_{si} \cdot \omega_{ci})^2 + 1) \cdot ((1.5 \cdot T_{sam} \cdot \omega_{ci})^2 + 1)}} \quad (16)$$

$$K_i = \frac{K_p}{T_n} \quad (17)$$

	Low Power Applications	High Power Applications
	Topologies 1 & 2	Topologies 3 & 4
$T_n$	6.8 ms	6.8 ms
$K_p$	36.09	8.05
$K_i$	5277	1177.4

Table 15. Parameters of the Grid Current PI controller

## 4.2. DC-Bus Voltage Control

The DC-Bus Voltage is controlled in two different situations:

- In order to implement CV Charging when the system comprises HV Batteries and only a FB as converter.
- Whenever a DC/DC converter is added to the system, since the DC-Bus is the link between the FB and this second converter. In this case, the control of this voltage is done to assure that all the power that goes through one converter flows as well through the second converter.

As provided in [46], the block diagram of the loop is pictured in Figure 48; the control part can be seen in red, while the real part is in green. This loop operates as follows:

1. Given a certain DC-Bus Voltage reference which is compared to the measured and filtered actual one, the PI controller provides the grid current reference in RMS value. It has to be noted that this value must be constrained to avoid the saturation of the control system. The controller used is digital and modeled as in the grid current control.
2. To obtain the real current reference, the RMS value is multiplied by  $\sqrt{2}$  to obtain the peak value and by a sine wave synchronized with the grid voltage. For this purpose, a Phase Locked Loop (PLL) is used. This synchronization provides a Power Factor (PF) close to 1, which reduces transmission losses and improves the capability of voltage regulation.
3. The DC-Bus voltage is compensated so that its changing value does not affect the control.

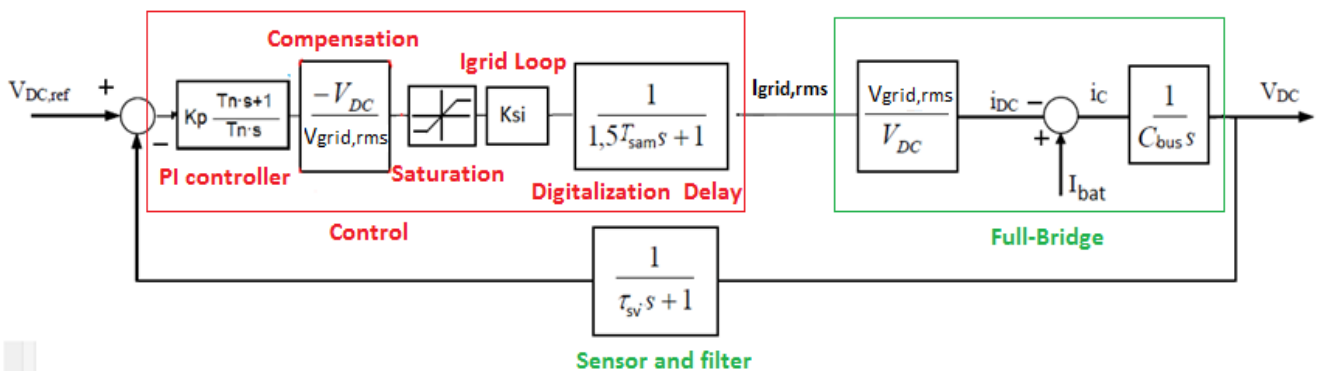


Figure 48. Block diagram of the DC-Bus Voltage Control Loop [46]

As in the previous control, equation (4) shows the transfer function of the PI controller while equation (8) includes the digitalization effect. The DC-Bus Voltage is measured and filtered. The transfer function of the sensor can be seen in equation (18).

$$S(s) = \frac{K_{sv}}{\tau_{sv} \cdot s + 1} \quad (18)$$

Where:

$K_{sv}$  is the voltage sensing constant, which has been taken as 1  
 $\tau_{sv}$  is the voltage sensing time constant. Its value is 53  $\mu$ s for a filter frequency of 3000 Hz, as obtained with equation (6).

The voltage is controlled using the Bus Capacitor, as in [46]. The transfer function of the FB can be seen in equation (19). The transfer function of the whole system, in open loop, is in equation (20).

$$B(s) = \frac{V_{grid,rms}}{V_{bus}} \cdot \frac{1}{C_{bus} \cdot s} \quad (19)$$

$$L(s) = K_p \frac{T_n \cdot s + 1}{T_n \cdot s} \cdot \frac{1}{C_{bus} \cdot s} \cdot \frac{K_{sv}}{\tau_{sv} \cdot s + 1} \cdot \frac{1}{1.5 \cdot T_{sam} \cdot s + 1} \quad (20)$$

#### 4.2.1. Stability and Velocity Study

As done for the grid current control loop, different cross-over frequencies have been tested. It is important to remember that since these loops are cascade controlled, the outer voltage loop must be at least 10 times slower than the inner grid current loop [51]. That way, the voltage loop sees the current control as instantaneous.

For a PM of 45°, Figure 49 shows the system's Bode Plots, Root Locus and Step Response for cross-over frequencies going from 1 to 100 Hz. The main information deduced from the step responses is stored in Table 16. From these results, it is deduced that the best option is to take a cross-over frequency of 100 Hz, since its response is the fastest one while its overshoot is the smallest. Moreover, the stability range is big enough, as seen in the Bode Plots.

PM = 45°				
Fc	1 Hz	10 Hz	50 Hz	100 Hz
Rise Time	0.185 s	18.4 ms	3.6 ms	<b>1.7 ms</b>
Settling Time	1.45 s	0.145 s	29.1 ms	<b>14.6 ms</b>
Overshoot	34.86	34.85	34.83	<b>34.77</b>
Peak Time	0.47 s	0.047 s	9.4 ms	<b>4.7 ms</b>

Table 16. Information of the Step response of the DC-Bus control system for a PM of 45°

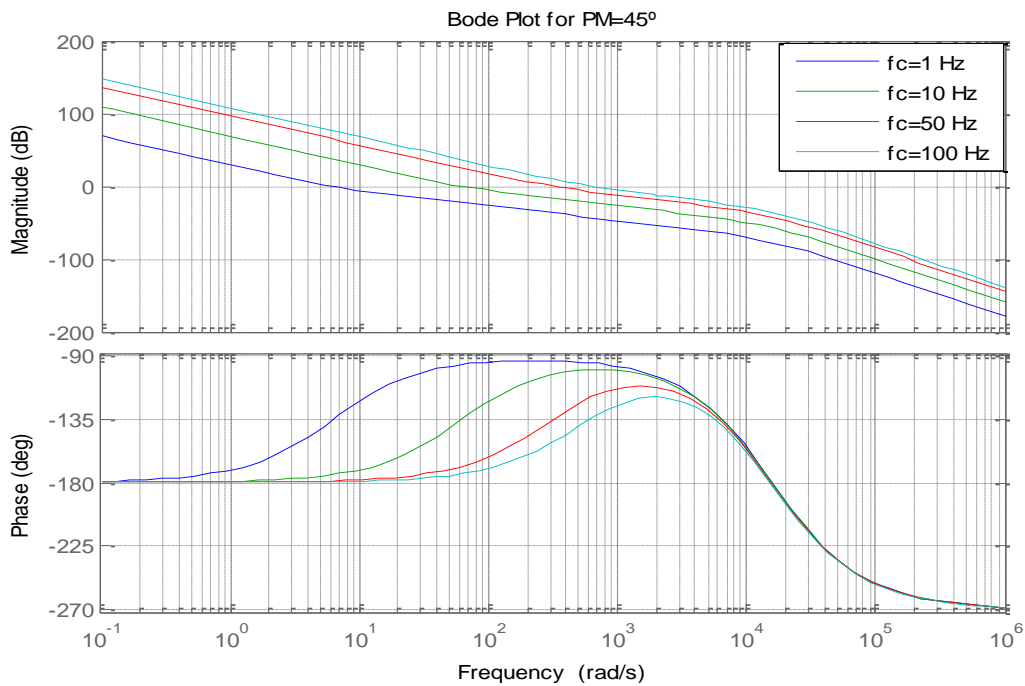
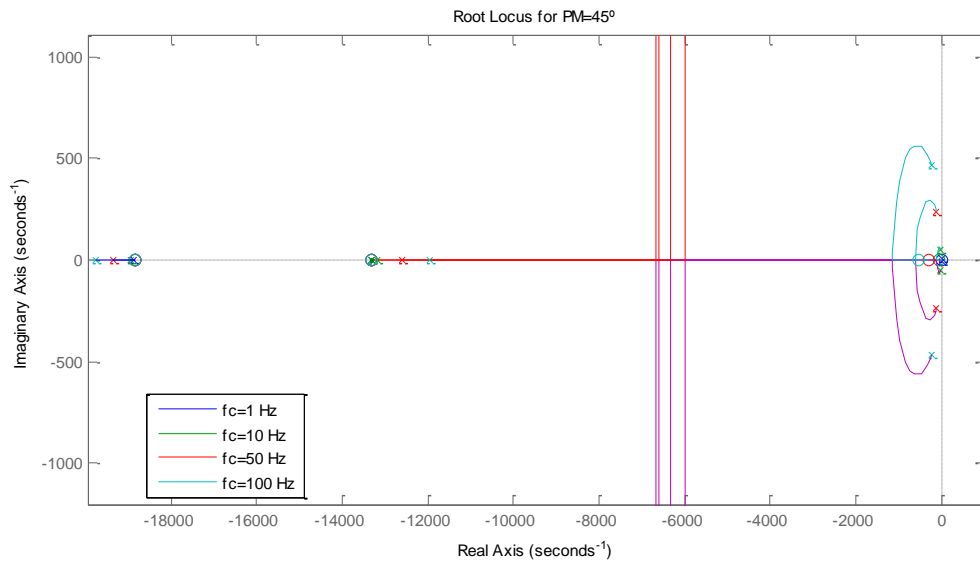
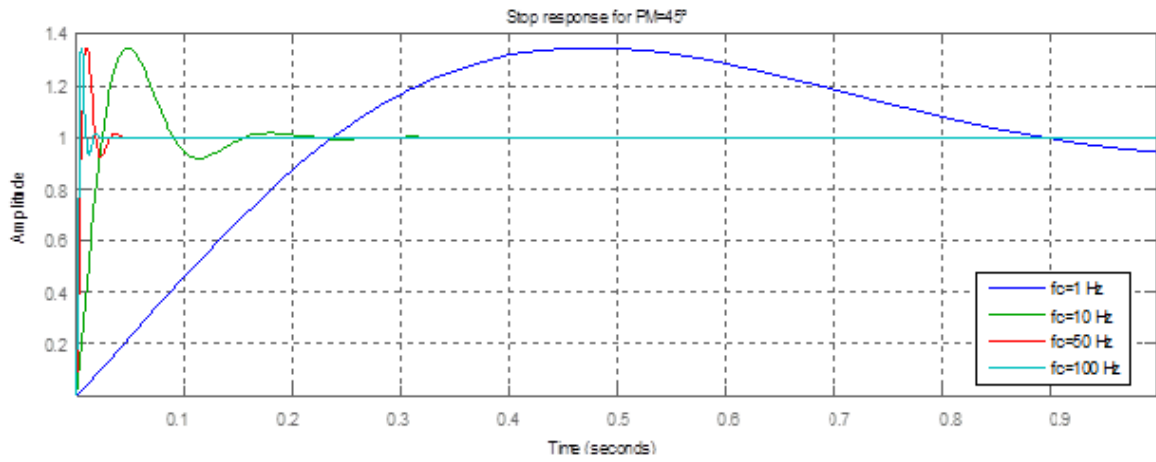


Figure 49. Step response, Root Locus and Bode Plots of the DC-Bus control system for a PM of 45° and cross-over frequencies from 1 to 100 Hz

#### 4.2.2. Modeling of the DC-Bus Voltage control

For low power applications, the control of the DC-Bus voltage is based on the following equation (21), in which an efficiency of 100 % has been considered. The control model developed for this section is shown in Figure 50.

$$P_{DC} = P_{AC} \rightarrow V_{bus} \cdot I_{DC} = I_{grid,rms} \cdot V_{grid,rms} \quad (21)$$

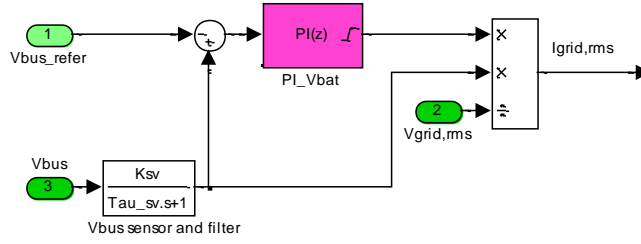


Figure 50. Simulink model of the DC-Bus Voltage Control for Low Power Applications

On the other hand, for three-phase systems, equation (22) is used, and the control model is depicted in Figure 51.

$$P_{DC} = P_{AC} \rightarrow V_{bus} \cdot I_{DC} = 3 \cdot I_{phase,grid,rms} \cdot V_{phase,grid,rms} \quad (22)$$

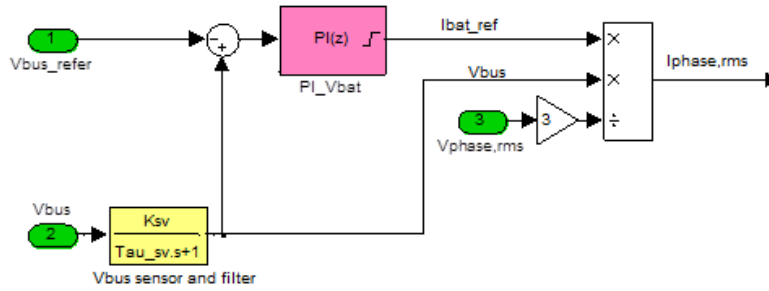


Figure 51. Simulink model of the DC-Bus Voltage Control for High Power Applications

#### 4.2.3. PI Parameters Calculation

The stability and velocity assessment resulted in choosing a PM of 45° and a cross-over frequency of 100 Hz for this control loop. Topology 2 used a lower frequency, of 10 Hz, to attenuate the voltage ripple appearing in the DC-Bus. The PM of the system is obtained in equation (23), from which  $T_n$  can be calculated. The  $K_p$  parameter is obtained using equation (24), which calculates the gain of the system. Finally,  $K_i$  is obtained using equation (17). The results are stored in Table 17.

$$PM = 45^\circ = \arctg(T_n \cdot \omega_{cv}) - \arctg(\tau_{sv} \cdot \omega_{cv}) - \arctg(1.5 \cdot T_{sam} \cdot \omega_{cv}) \quad (23)$$

$$|L(j\omega_{cv})| = 1 = \frac{K_p \cdot K_{sv}}{T_n \cdot C_{bus} \cdot \omega_{cv}^2} \sqrt{\frac{(T_n \cdot \omega_{cv})^2 + 1}{((\tau_{sv} \cdot \omega_{cv})^2 + 1) \cdot ((1.5 \cdot T_{sam} \cdot \omega_{cv})^2 + 1)}} \quad (24)$$

	Low Power Applications		High Power Applications	
	Topology 1	Topology 2	Topology 3	Topology 4
$T_n$	1.9 ms	16.2 ms	1.9 ms	1.9 ms
$K_p$	1.57	0.147	11.95	11.95
$K_i$	841.19	9.0897	6391	6391

Table 17. Parameters of the DC-Bus Voltage PI controller

### 4.3. Grid Power Control

The grid power control consists of generating the grid current reference based on a power reference introduced by the user. For low power applications, where the grid comprises a single phase, the current reference is obtained using equation (25). On the contrary, for three-phase systems, equation (26) is employed. Figure 52 and 53 show the designed models used to implement this control, based on the mentioned equations.

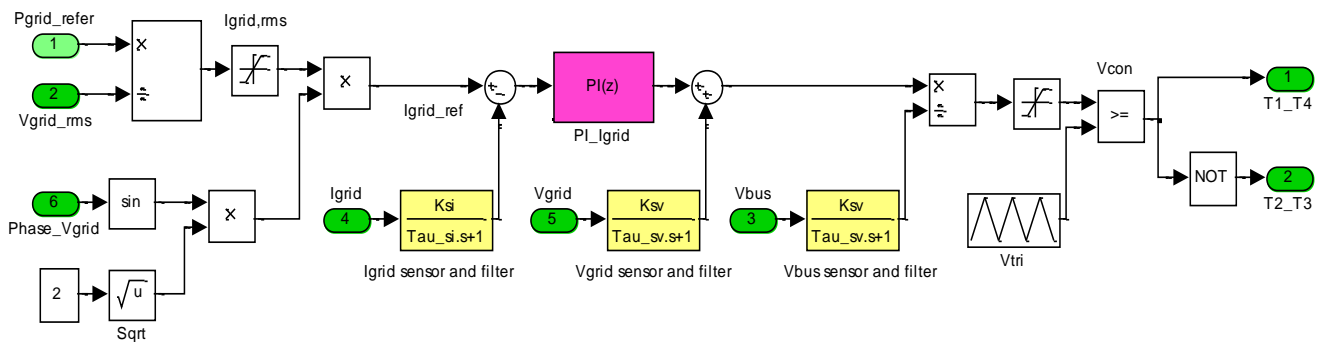


Figure 52. Simulink model for the Grid Power control for Low Power Applications

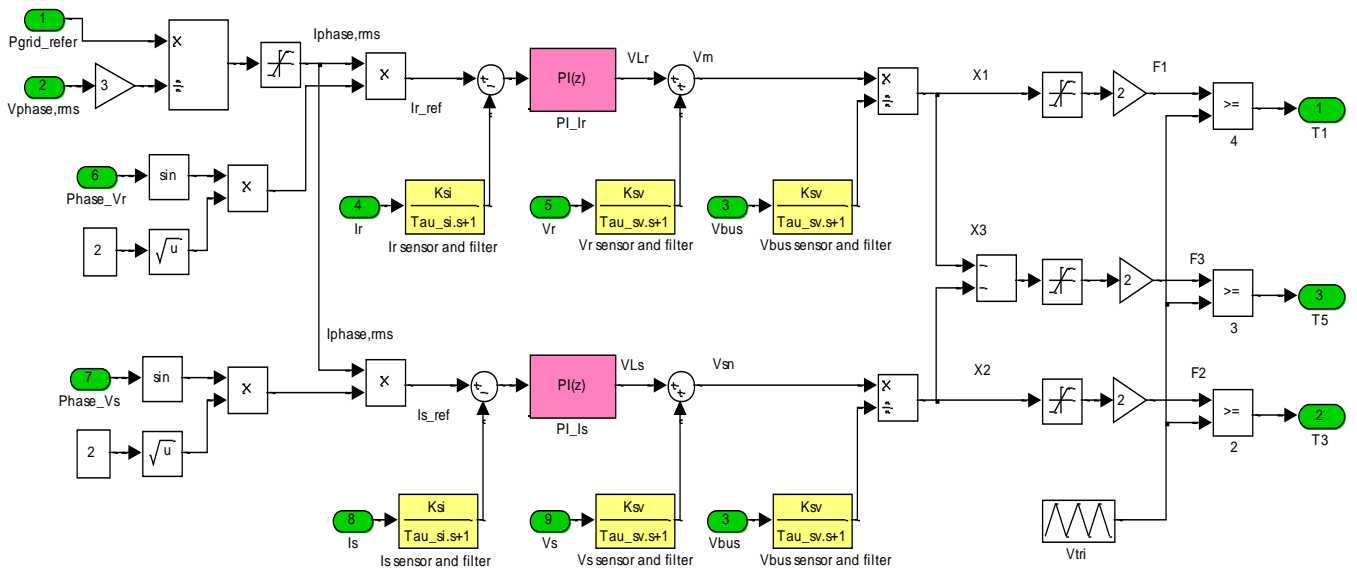


Figure 53. Simulink model for the Grid Power control for High Power Applications

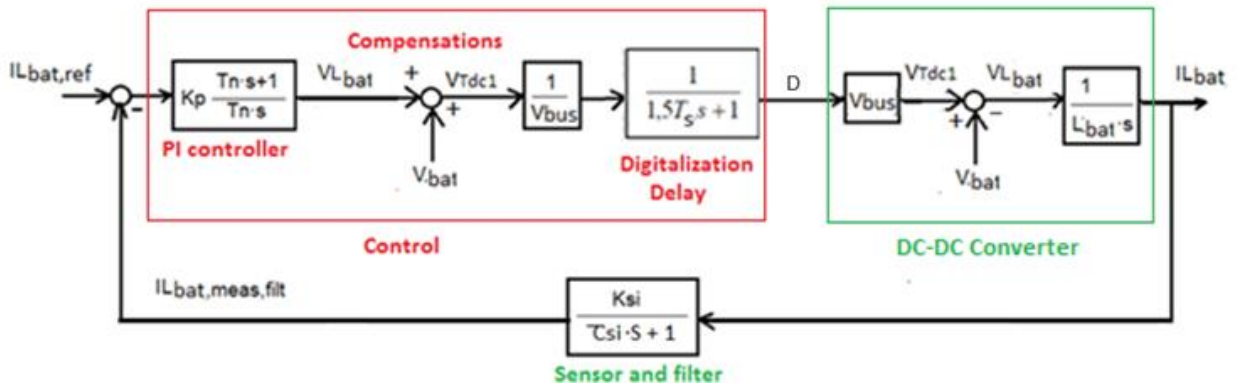
$$I_{grid,rms,ref} = \frac{P_{grid,ref}}{V_{grid,rms}} \quad (25)$$

$$I_{grid,rms,ref} = \frac{P_{grid,ref}}{3 \cdot V_{grid,rms}} \quad (26)$$

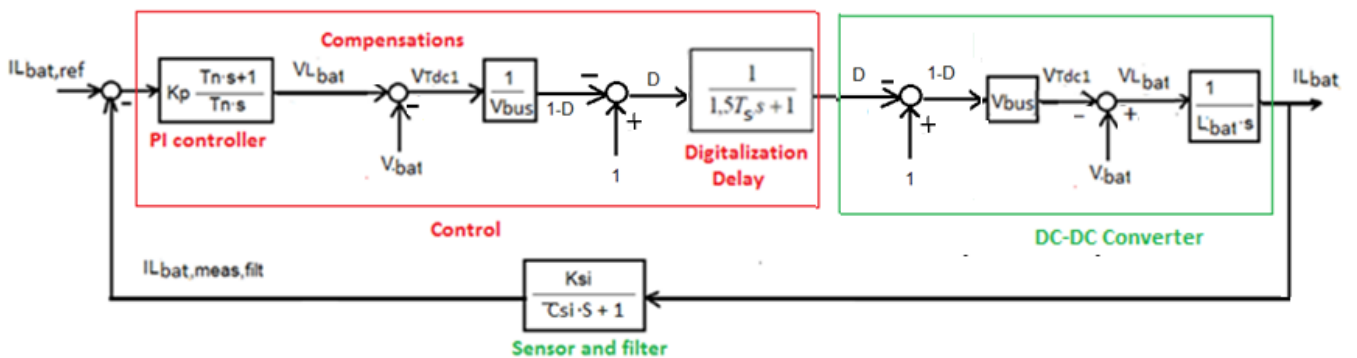
#### 4.4. Battery Current Control

When the system comprises LV-Batteries, it is necessary to add a DC/DC Converter. This converter works in a different way depending on the direction of the power flow. If the batteries are being charged, it becomes a Buck converter and it is controlled by a current loop that provides the switching patterns for IGBT 2. On the contrary, when the batteries are being discharged, the converter becomes a Boost and another current control loop provides the switching patterns for IGBT 1.

Based on the controls performed to Buck and Boost converters in [51], the block diagrams of the loops are depicted in Figure 54, where the control part is colored in red and the real part in green. It can be seen that the same transfer function is obtained for both models, as presented in equation (28).



(a) Charging mode working as a Buck converter



(b) Discharging mode working as a Boost converter

Figure 54. Block diagram of the Battery Current Control Loop [51]



The charging mode's loop operates as follows:

1. Given a certain battery current reference, which is compared to the measured and filtered actual current, a digital PI controller provides the battery side inductor's voltage.
2. The battery voltage is added to obtain the voltage in the IGBT 1. This way, the compensation of the  $V_{bat}$  introduced in the plant of the system performed, so a better response and tracking is achieved.
3. The voltage in IGBT 1 is divided by the DC-Bus Voltage to obtain the control signal for the PWM. The advantage of dividing the signal by the DC-Bus voltage is that the loop will not be affected by its changing value because it does not appear in the transfer function of the loop.

The operation of the discharging mode's loop is explained below:

1. The battery current reference is compared to the measured and filtered actual current, and the digital PI controller provides the battery side inductor's voltage.
2. The battery voltage is subtracted to obtain the voltage in the IGBT 1. This way, the compensation of the  $V_{bat}$  introduced in the plant of the system is carried out.
3. The IGBT voltage is divided by the DC-Bus Voltage, obtaining  $1-D$ , where  $D$  is the control signal. Thus, after operating with this signal to obtain  $D$ , the PWM can be performed.

The transfer functions used to model the controller, sensor and digitalization's delay are the same as in the Grid Current Control, so they can be seen in equations (4), (5) and (8), respectively.

As reported in [51], the transfer function of the DC-DC converter with its modulation is shown in equation (27). The PWM of this converter is performed with a triangular wave that goes from 0 to 1 V at a commutation frequency of 20 kHz. The sensor and filter used are the same than the used for the grid current, with a sensing constant of 1 and a frequency of 3000 Hz. In conclusion, the transfer function of the whole system, in open loop, can be seen in equation (28).

$$DC(s) = V_{bus} \cdot \frac{1}{L_{bat} \cdot s} \quad (27)$$

$$L(s) = K_p \frac{T_n \cdot s + 1}{T_n \cdot s} \cdot \frac{1}{L_{bat} \cdot s} \cdot \frac{K_{si}}{\tau_{si} \cdot s + 1} \cdot \frac{1}{1.5 \cdot T_s \cdot s + 1} \quad (28)$$

#### 4.4.1. Modeling of the Battery Current control

In this case, the control models designed for high and low power applications are the same except for the value of the battery side inductor  $L_{bat}$ .

The modeling of the battery current control during charging mode can be seen in Figure 55. It should be noted that the control signal  $d$  is constrained between 0 and 1, lower and higher limits of the triangular wave, in order to avoid the saturation of the controller. It is also worth noticing that the IGBT controlled in this case is the number 2, so the switching signal for the IGBT 1 is 0.

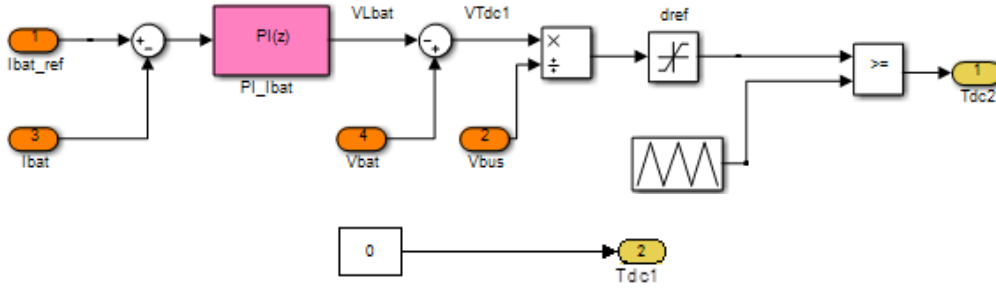


Figure 55. Simulink model of the battery current control during charging mode

On the other hand, the designed model for the battery current control during discharging mode is depicted in the following Figure 56. In this case, the IGBT controlled is the number 1, so the switching signal for the IGBT 2 is 0.

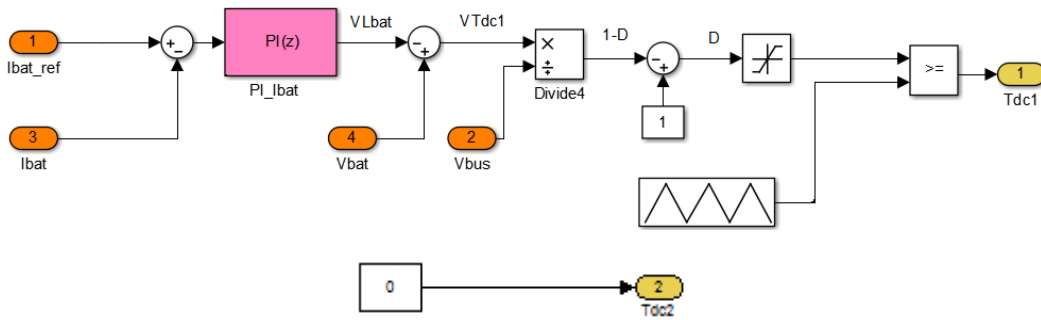


Figure 56. Simulink model of the battery current control during discharging mode

#### 4.4.2. PI Parameters Calculation

The transfer function of these control loops is equivalent to the one for the grid current control, shown in equation (9). The only difference is the value of the inductance. Thus, the stability and velocity study performed in section 4.1.1 is equally valid for this control loop and the values chosen for the cross-over frequency and phase margin are 1000 Hz and 45°, respectively.

Equation (15) is used to obtain  $T_n$ ,  $K_p$  is calculated using equation (29) and  $K_i$  using equation (17). The results are stored in Table 18.

$$|L(j\omega_{ci})| = 1 = \frac{K_p \cdot K_{Si}}{T_n \cdot L_{bat} \cdot \omega_{ci}^2} \sqrt{\frac{(T_n \cdot \omega_{ci})^2 + 1}{((\tau_{Si} \cdot \omega_{ci})^2 + 1) \cdot ((1.5 \cdot T_{sam} \cdot \omega_{ci})^2 + 1)}} \quad (29)$$

	Low Power Applications	High Power Applications
	Topology 2	Topology 4
$T_n$	6.8 ms	6.8 ms
$K_p$	8.3	8.68
$K_i$	1213.8	1269.5

Table 18. Parameters of the Battery Current PI controller

## 4.5. Battery Voltage Control

In order to achieve Constant Voltage charging mode when a DC/DC converter is added to the FB, a voltage loop has to be implemented. This loop generates the battery current reference for the current inner loop, so a cascaded control is implemented. The block diagram of this voltage control, as described in [51], is depicted in Figure 57. The same loop can be used for both charging and discharging modes as long as the currents are considered and measured in the same direction, regardless the direction of the power flow. In this thesis, they were considered positive when exiting the battery.

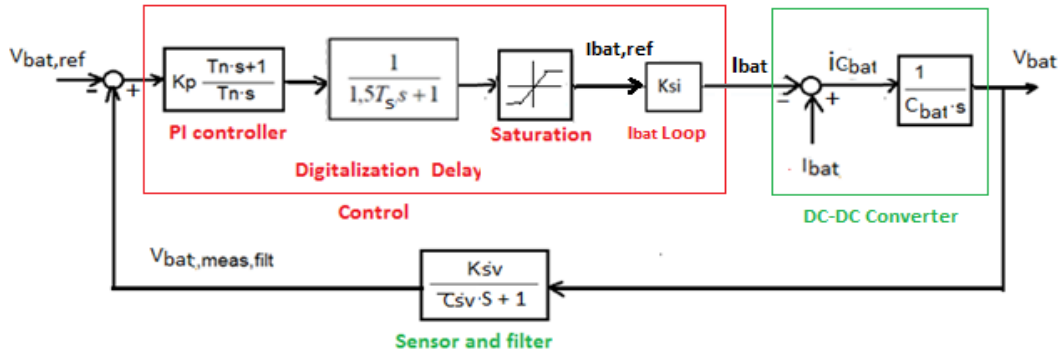


Figure 57. Block diagram of the Battery Voltage Control Loop [51]

The behavior of this loop is explained in the following lines:

1. A certain Battery Voltage Reference is provided by the user, and compared to the measured and filtered actual voltage.
2. Their difference enters a digital PI controller that supplies the Battery Current Reference for the inner current loop. This current has to be restrained in order to avoid saturation.
3. The plant of the converter is based on the currents of the battery and through the capacitor. This capacitor is what enables the voltage control.

The transfer functions used to model the controller, sensor and digitalization's effect are the same than in the DC-Bus Voltage Control, so they can be expressed with equations (4), (18) and (8), respectively. The sampling frequency is 20 kHz, the sensing constant is 1 and the sensing frequency 3000 Hz. The transfer function of the DC/DC Converter was developed in [51], and it can be expressed as in equation (30). The overall transfer function, in open loop, is shown in equation (31).

$$DC(s) = \frac{1}{C_{bat} \cdot s} \quad (30)$$

$$L(s) = K_p \frac{T_n \cdot s + 1}{T_n \cdot s} \cdot \frac{1}{C_{bat} \cdot s} \cdot \frac{K_{sv}}{\tau_{sv} \cdot s + 1} \cdot \frac{1}{1.5 \cdot T_{sam} \cdot s + 1} \quad (31)$$

### 4.5.1. Modeling of the Battery Voltage control

The model developed for the battery voltage's control is shown in Figure 58. It can be noted that the PI controller provides the current reference, constrained due to the power limit of the charger.

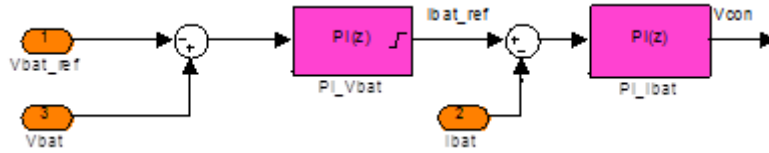


Figure 58. Simulink model of the Battery Voltage Control

#### 4.5.2. PI Parameters Calculation

Given the Phase Margin of  $45^\circ$  and crossover frequency of 100 Hz, the PI parameters are calculated. The equations utilized are equivalent to those for the DC-Bus Voltage control loop, except for the values of the capacitor. Therefore,  $T_n$  is calculated using equation (23),  $K_p$  using equation (32) and  $K_i$  using equation (17). The resulting values are stored in Table 19.

$$|L(j\omega_{cv})| = 1 = \frac{K_p \cdot K_{sv}}{T_n \cdot C_{bat} \cdot \omega_{cv}^2} \sqrt{\frac{(T_n \cdot \omega_{cv})^2 + 1}{((\tau_{sv} \cdot \omega_{cv})^2 + 1) \cdot ((1.5 \cdot T_{sam} \cdot \omega_{cv})^2 + 1)}} \quad (32)$$

	Low Power Applications	High Power Applications
	Topology 2	Topology 4
$T_n$	1.9 ms	1.9 ms
$K_p$	0.2672	0.0638
$K_i$	142.84	34.08

Table 19. Parameters of the Battery Voltage PI controller

#### 4.6. Battery Power Control

The last option to provide the reference battery current consists on generating it from a battery power reference, introduced by the user. For this, the following equation (33), where  $V_{bat}$  is the measured and filtered battery's voltage, is employed.

$$I_{bat,ref} = \frac{P_{bat,ref}}{V_{bat}} \quad (33)$$

The designed model of this control is depicted in Figure 59. The reference current is limited in order not to surpass the maximum power of the charger. Afterwards, the PI controller generates a different control signal depending on the direction of the power flow in the system, as explained before in Section 4.4.

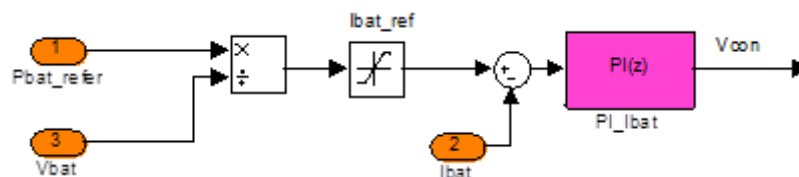


Figure 59. Simulink model of the battery power control

## 5. VERIFICATION AND SIMULATION RESULTS

Once the models of the converters and their controls have been designed and implemented in Matlab/Simulink, some tests have been performed to check their correct operation. First of all, the single-phase systems for low power applications are going to be studied. Afterwards, a similar study is carried on the three-phase systems for high power applications. At the end of this section, some real values measured from a Nissan Leaf are presented and compared to the simulation results.

### 5.1. Topology 1: Full Bridge converter for Low Power applications

The charging and discharging methodology chosen for this test is Constant Voltage. When charging, the reference battery voltage introduced is 400 V; when discharging, the reference voltage is 370V.

In Figure 60, the grid voltage and current are depicted. A current exiting the battery is considered positive, since the battery has been taken as reference of the system. Therefore, the current and voltage are in phase in V2G operation. It can be seen that the Power Factor is 1 for both cases, so the system does not provide reactive power. The charge and discharge is performed at maximum power rate of 3.3 kW. The grid current harmonics are shown in Figure 61. The DC current to the grid is quite high, so introducing a transformer in the charger's structure may be considered.

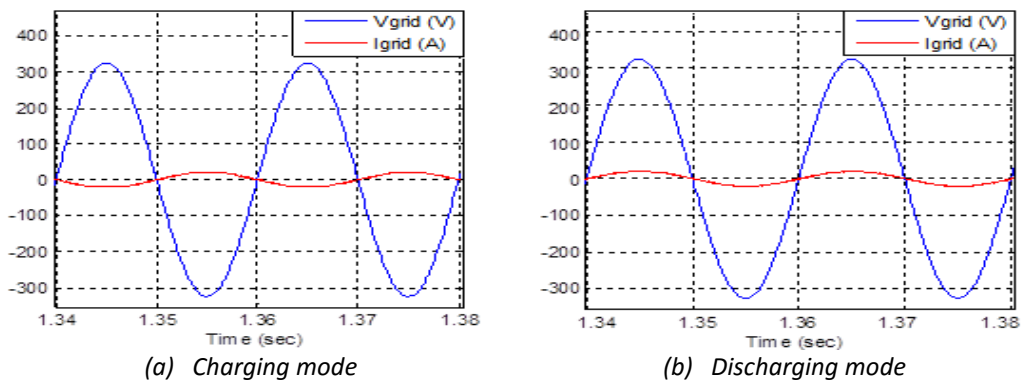
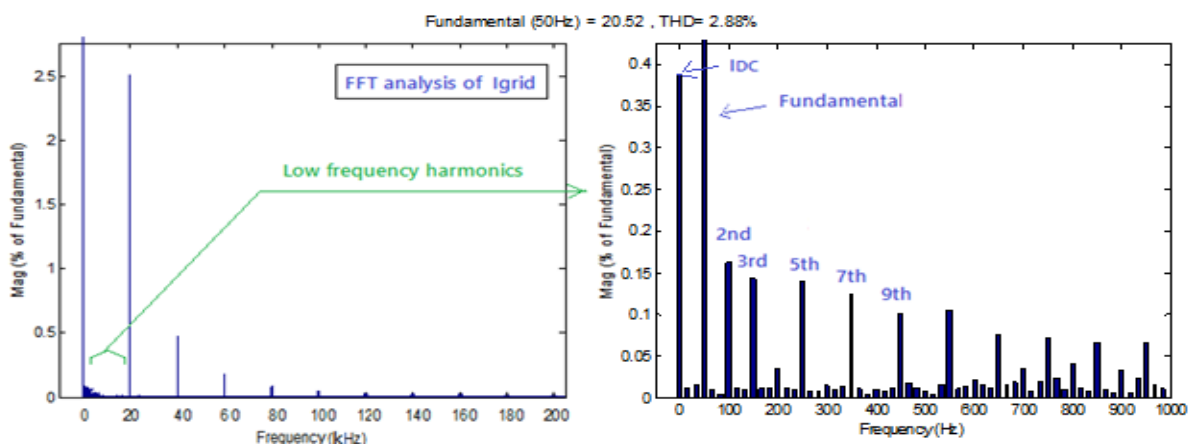
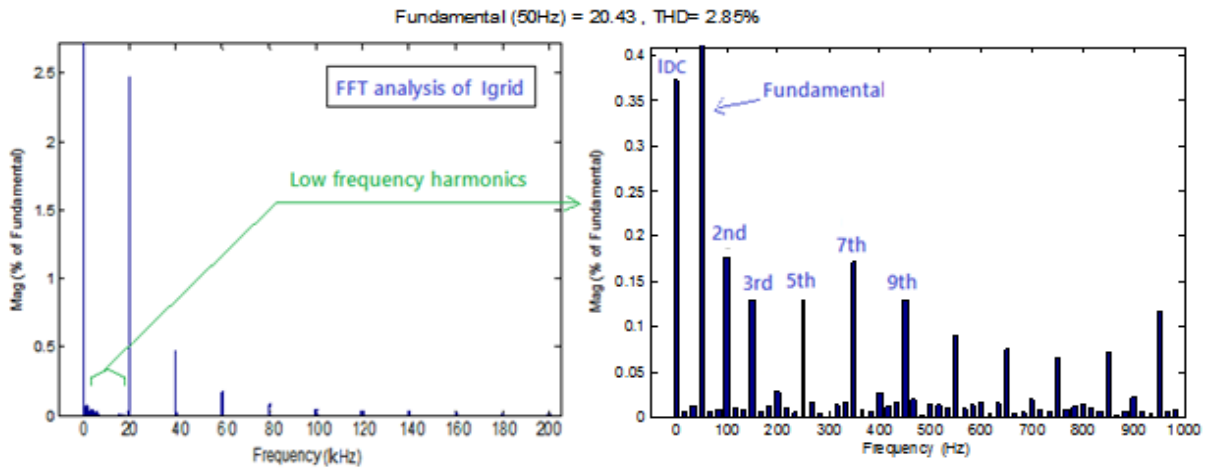


Figure 60. Grid Current and Voltage at maximum power for Bipolar Modulation



(a) Charging mode



(b) Discharging mode

Figure 61. Harmonic content of the grid current for Bipolar Modulation

An option to reduce the current harmonics is the use of unipolar instead of bipolar modulation. The results obtained with it are shown in Figure 62. It can be seen that the THD has been reduced from 2.88 % for bipolar to 0.89% for unipolar, using the same output filter. Moreover the DC current is also reduced significantly.

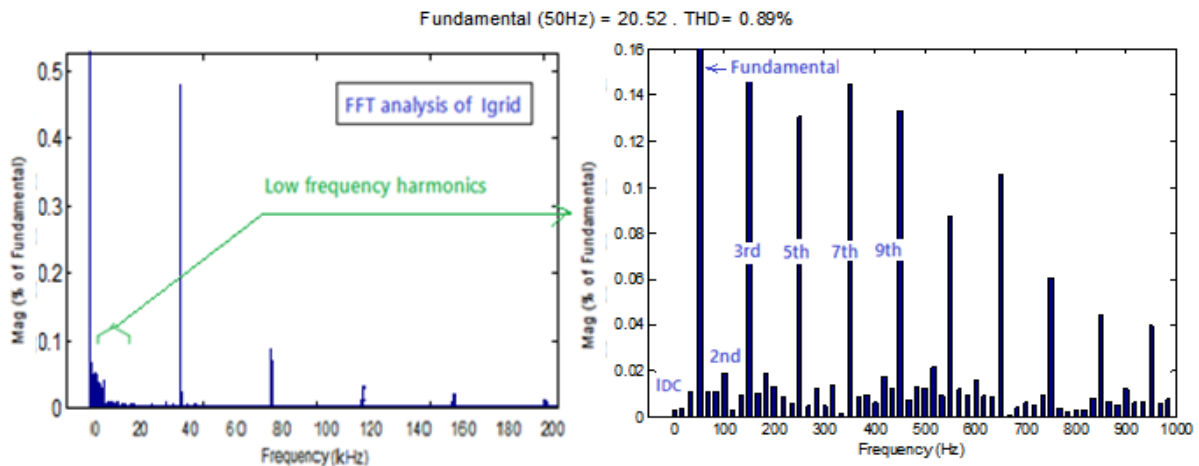


Figure 62. Harmonic content of the grid current in charging mode for Unipolar Modulation

The commutation branches generate a voltage wave  $V_{12}$  whose values, with bipolar modulation, can be  $+V_{bus}$  or  $-V_{bus}$ . After filtering this voltage, the grid voltage is obtained. When the grid voltage's wave reaches high values, the  $V_{12}$  wave is  $V_{bus}$  most of the time. On the contrary, for big negative values, it is  $-V_{bus}$ . This effect can be seen in Figure 63, while Figure 64 shows the harmonics content of  $V_{12}$ . It can be noted that for low frequencies, the odd harmonics are the most present, while for high frequencies the highest harmonics occur as multiples of the commutation frequency of 20 kHz. Moreover, the THD in charging mode is slightly higher than in discharging mode.

When unipolar modulation is used, the  $V_{12}$  wave can take the values  $+V_{bus}$ , 0 and  $-V_{bus}$ , as seen in Figure 65. Thus, the harmonic content in this case is reduced from a THD of 140.89% to 74.60%. It must be noted that the biggest harmonic, at 20 kHz, is eliminated.

The PWM and switching patterns for both bipolar and unipolar modulations are shown in the following Figure 66. Their main difference is that in unipolar modulation, each branch works separately, so two control signals must be used.

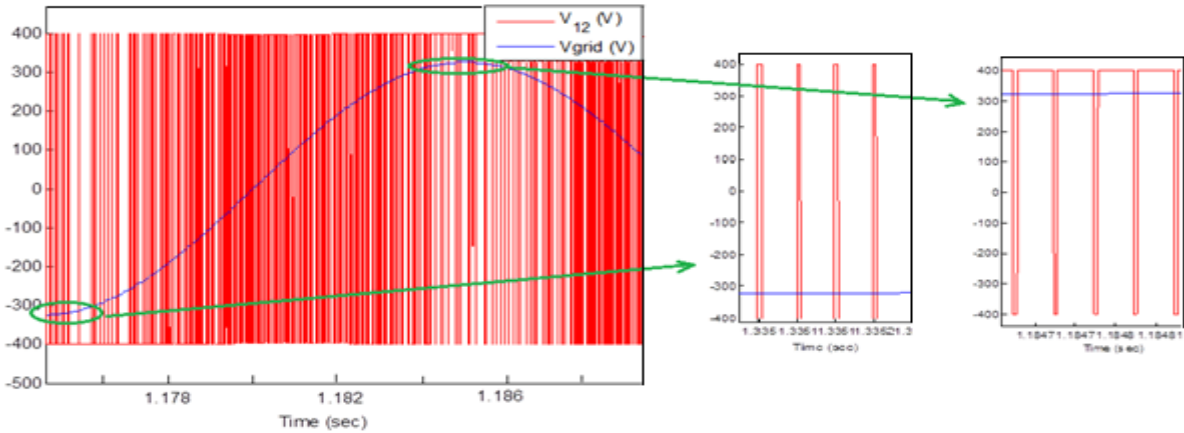
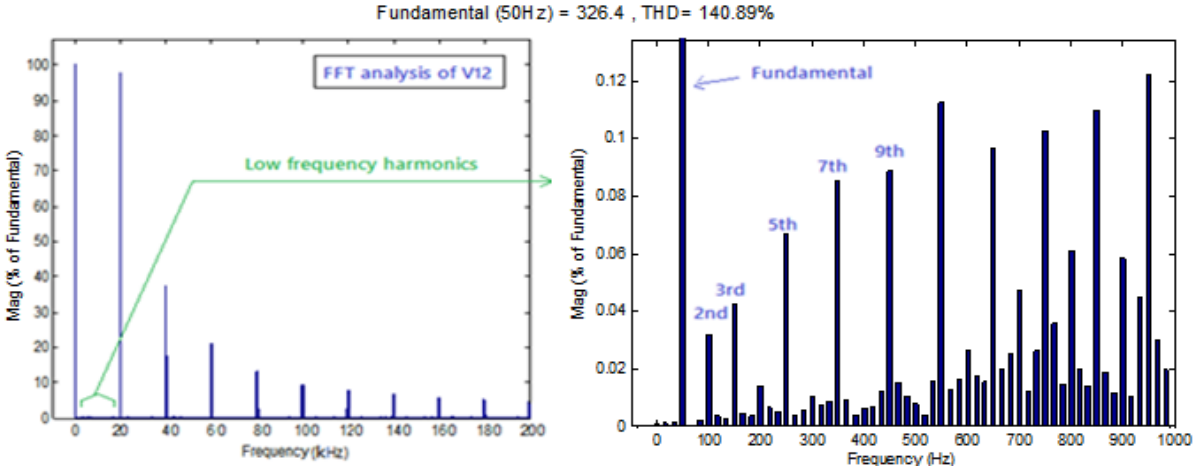
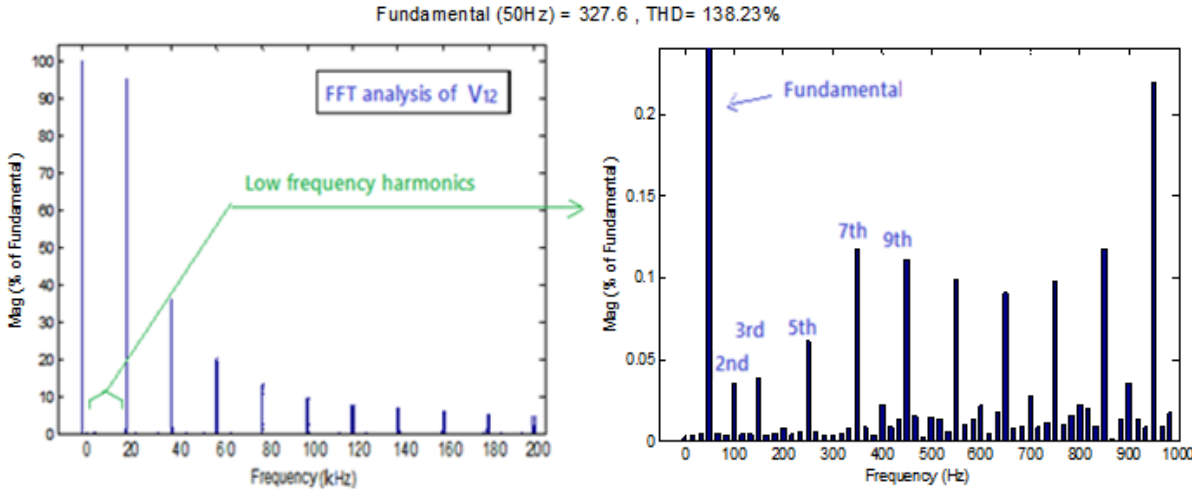


Figure 63. Grid Voltage before and after being filtered for bipolar modulation

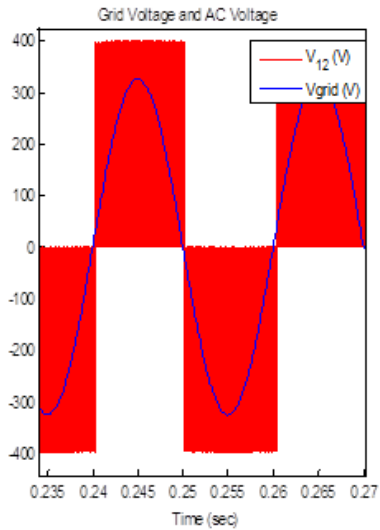


(a) Charging mode

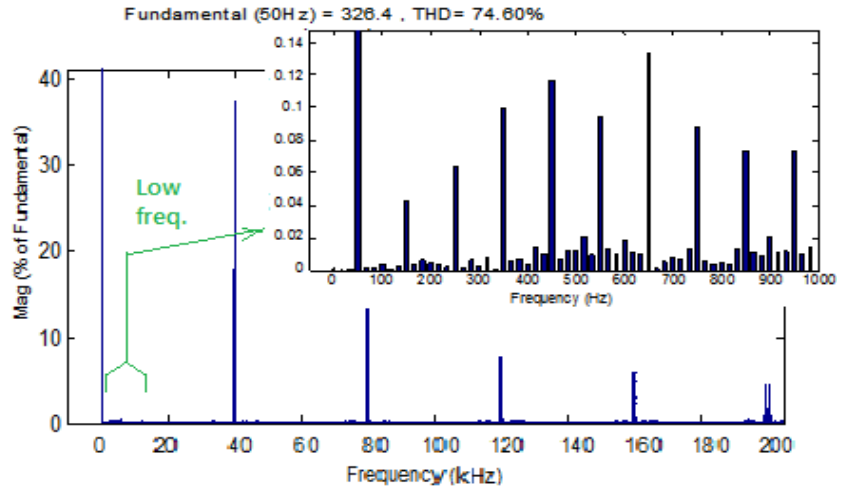


(b) Discharging mode

Figure 64. Harmonic content of the AC Voltage  $V_{12}$  for bipolar modulation

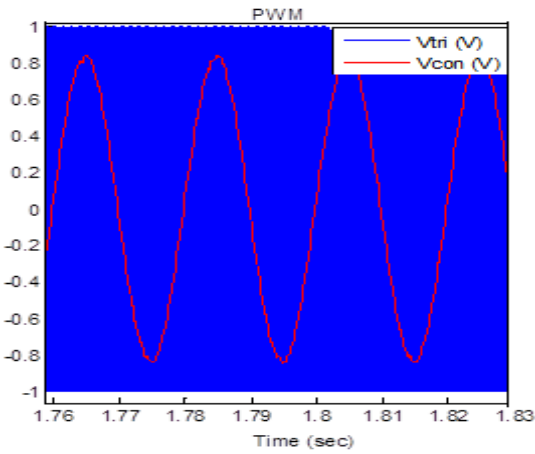


(a) Grid voltage before and after being filtered

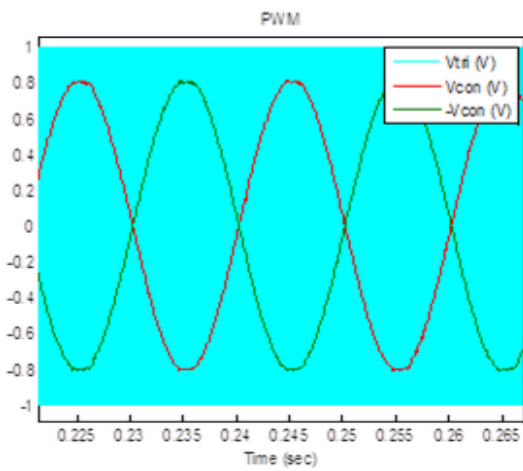
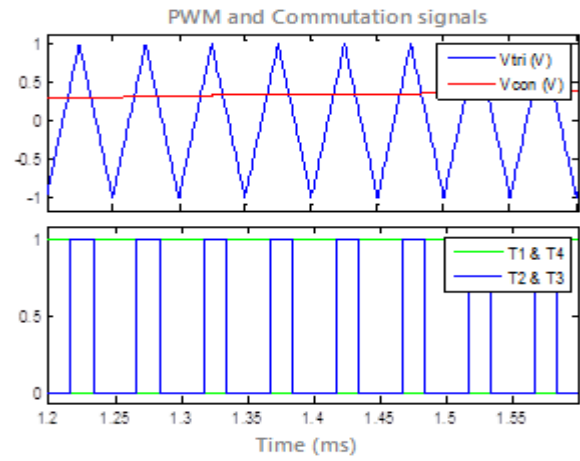


(b) Harmonics content of V12

Figure 65. Grid and AC voltage characteristics for Unipolar Modulation



(a) Bipolar Modulation



(b) Unipolar Modulation

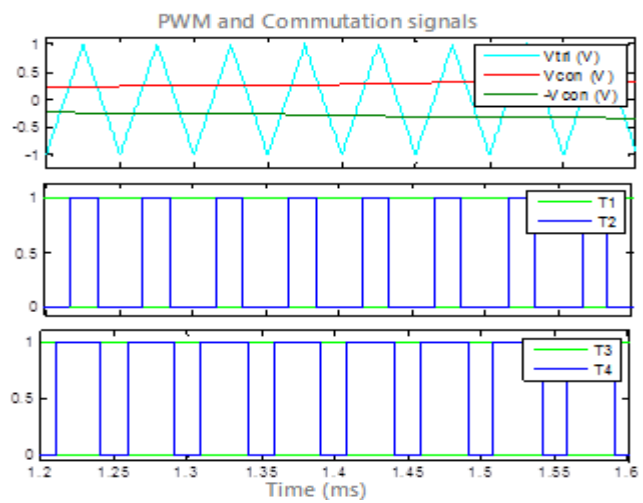


Figure 66. PWM and sitching patterns, at 20 kHz



In Figure 67, the grid and battery powers are depicted. It has no be noted that even if the mean value of both powers is the same, the grid’s power has a very big oscillation at 100 Hz, double the grid’s frequency. This kind of oscillating frequency is characteristic of single-phase systems. In order to attenuate this ripple in the battery side, an LC filter has been installed. Its good behavior is furtherly proved looking at Figure 68, where the DC-Bus voltage and the battery’s voltage during charging mode can be seen. It must be highlighted that the voltage ripple in the battery is much smaller than in the DC-Bus, thanks to the action of the LC filter. It can be noted that as the battery is charging, its voltage increases tending to reach the reference voltage.

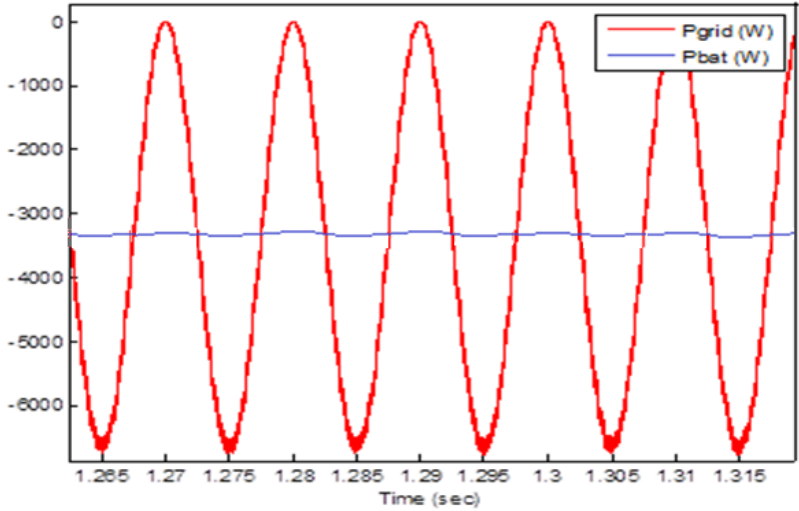


Figure 67. Grid and battery power at charging mode

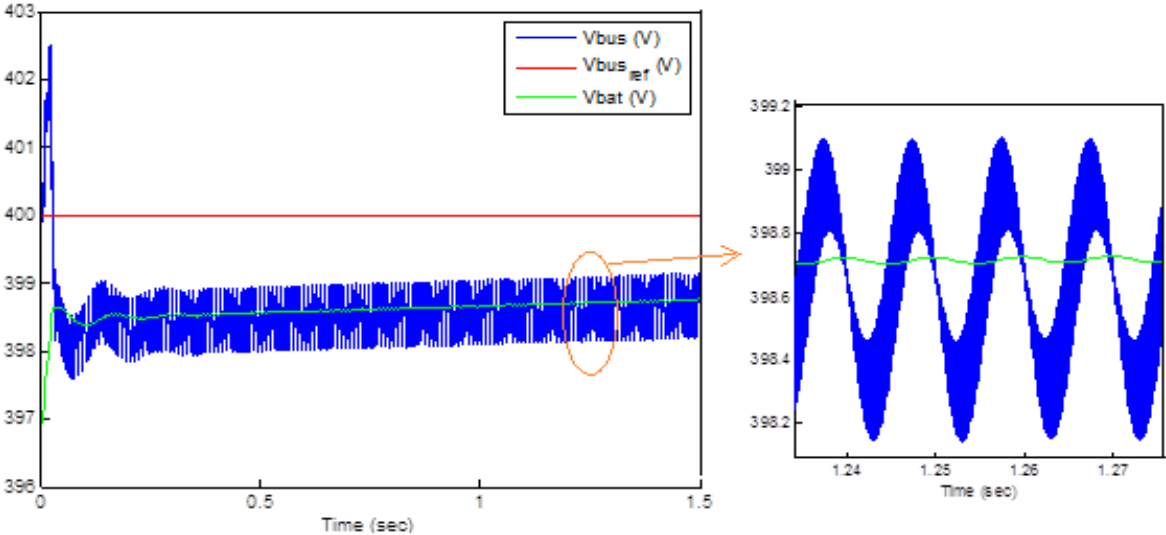
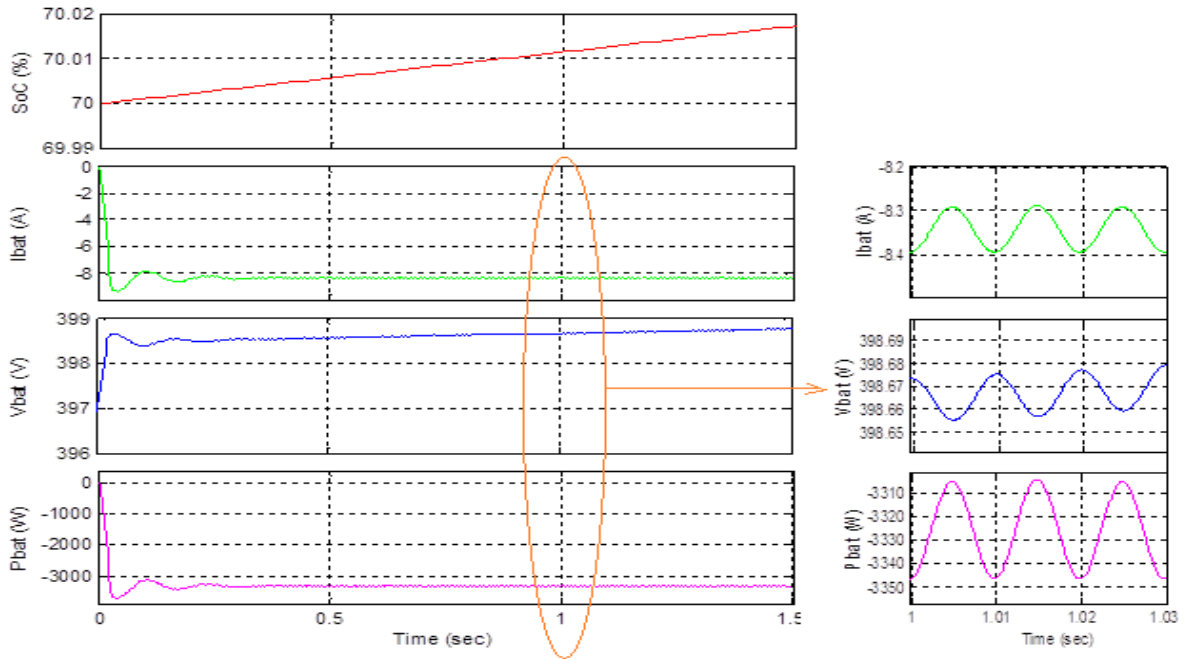
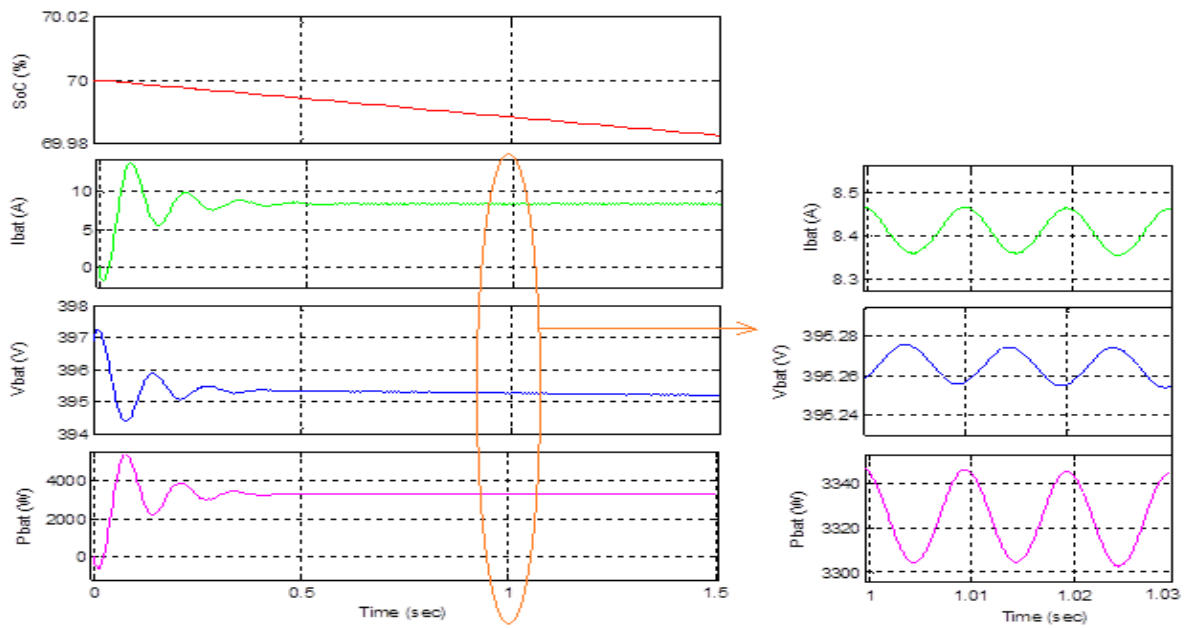


Figure 68. Battery’s voltage evolution for CV Charging

The battery’s State of Charge (SoC), current, voltage and power are depicted in Figure 69, for both charging and discharging modes. The 100 Hz ripple in the current, voltage and power is appreciated, even if its value is not harmful for the battery as its amplitude is small in both operating modes.



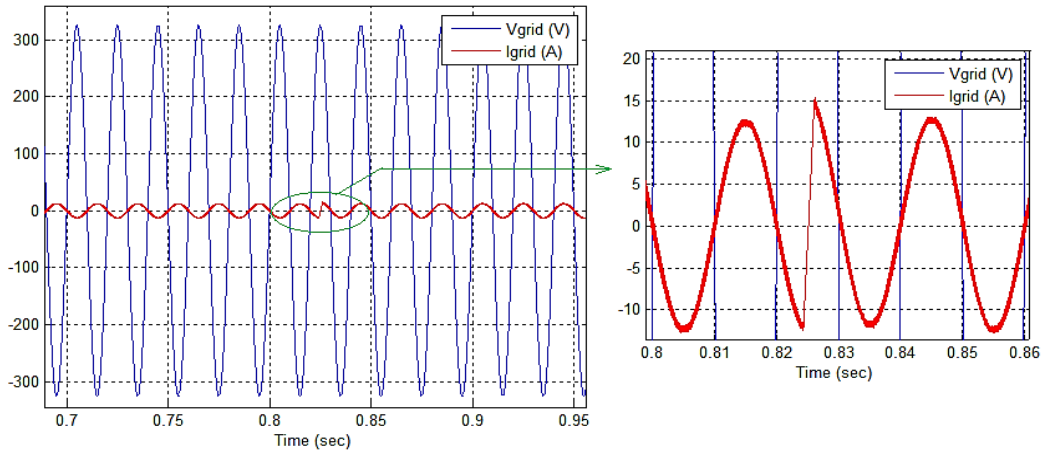
(a) Charging Mode



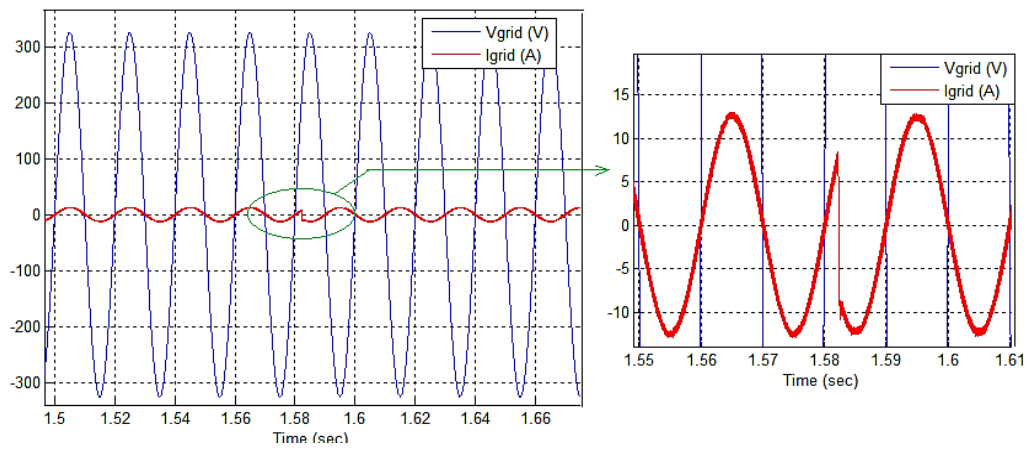
(b) Discharging mode

Figure 69. Battery's SoC, current, voltage and power for CV Charging

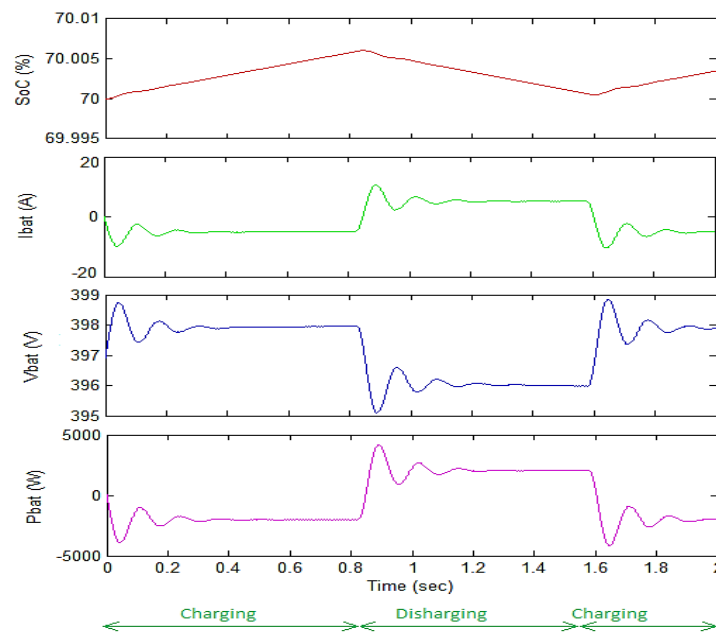
To check the flexibility of the control implemented, Figure 70 shows the transition between charging and discharging modes, while Figure 71 shows a change in the reference power from 3000 W to 1500 W, when Constant Power Charging is being performed. It can be noted that the system reacts very fast in the grid side, whereas the battery side is slower.



(a) Grid current and voltage in the transition from charging to discharging

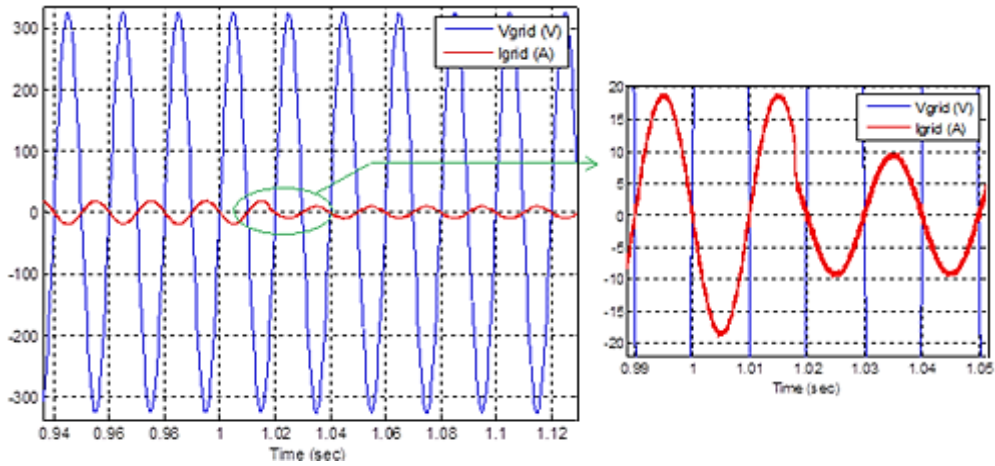


(b) Grid current and voltage in the transition from discharging to charging

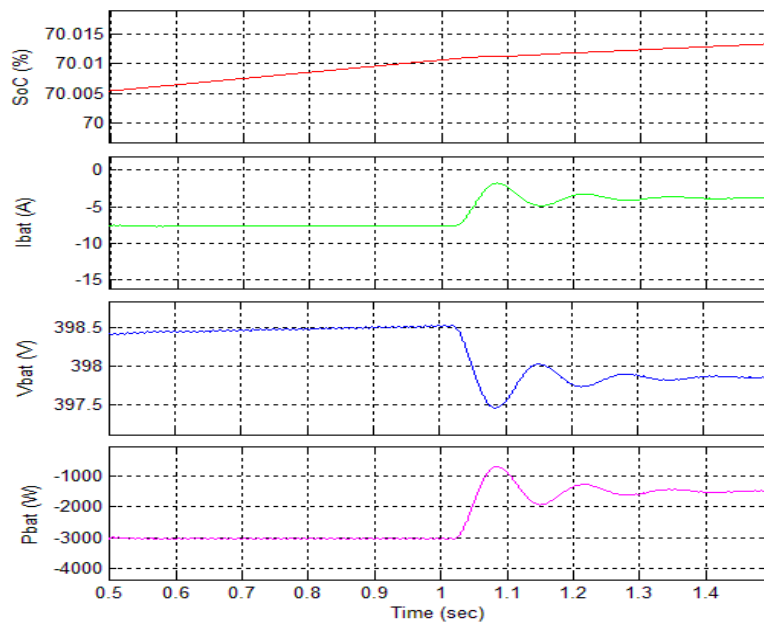


(c) Battery's SoC, current, voltage and power

Figure 70. Transition between charging and discharging modes



(a) Grid current and voltage



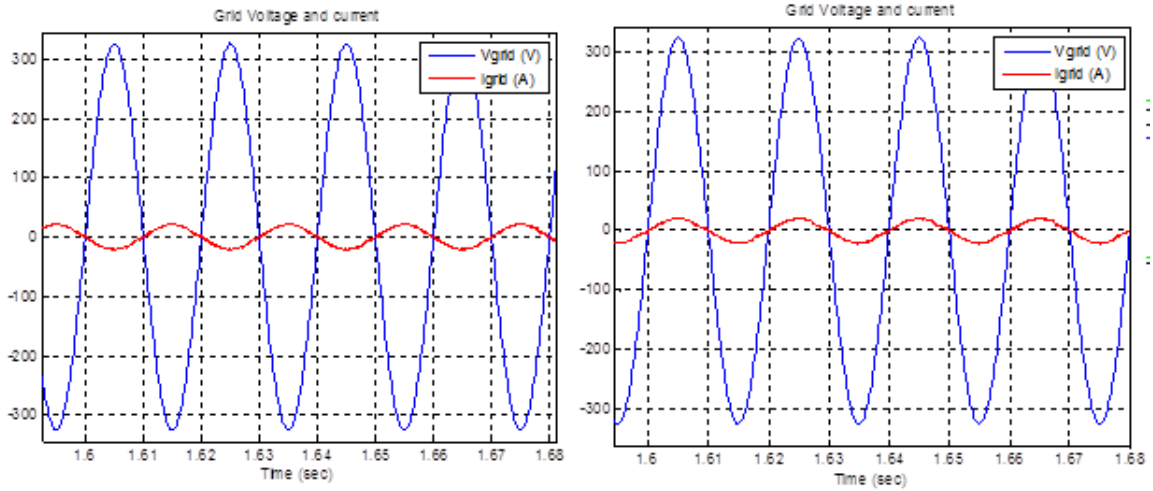
(b) Battery's SoC, current, voltage and power

Figure 71. Change in the reference current during CP Charging

## 5.2. Topology 2: Full Bridge and DC/DC converter for Low Power applications

In this case, a Two-Quadrant Converter is added to the previous topology. In the following lines, the results from simulating this new system for Constant Voltage charging and discharging are shown, provided a reference battery voltage of 150 V and 130 V, respectively.

It is demonstrated that the Full Bridge's control is still working fine: as seen in Figure 72, the grid current and voltage are synchronized, so that there is not any reactive power; furthermore, the DC-Bus voltage is kept at its nominal value, as pictured in Figure 73. As before, the battery is taken as the reference of the system, so the current is positive in V2G mode.



a) Charging mode

(b) Discharging mode

Figure 72. Grid current and voltage for CV methodology

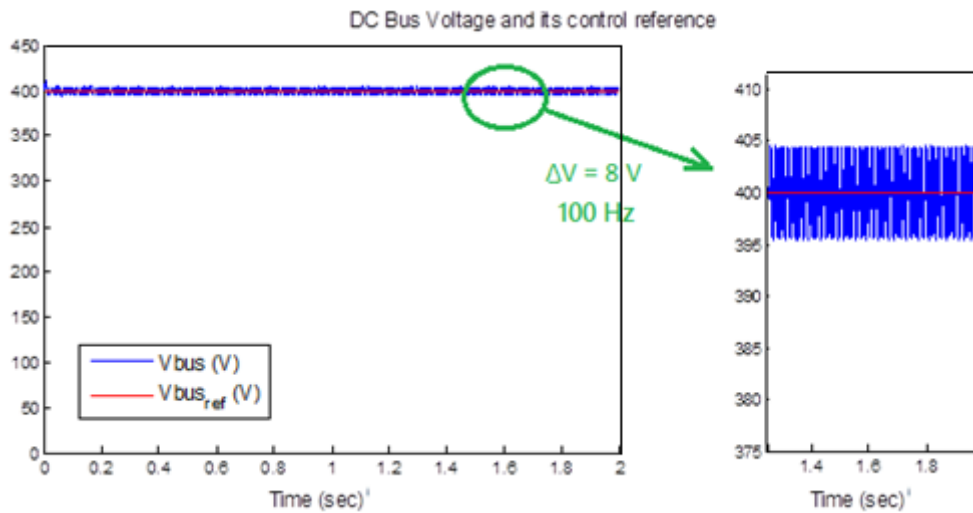


Figure 73. DC-Bus Voltage and its reference for CV Charging

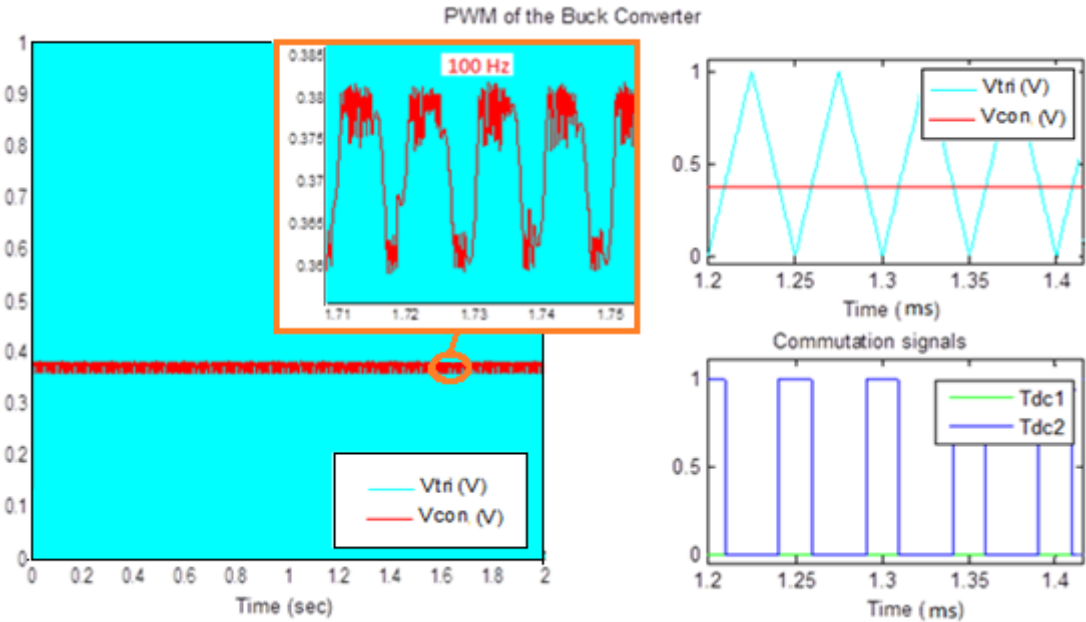
A FFT analysis has been performed, and the results, compared to the previous case, are stored in Table 20. It is worth noting that the addition of the Two-Quadrant converter does not increase the harmonics content of the system.

		Full Bridge		FB + DC/DC	
		Igrid	V12	Igrid	V12
Charging mode	Fundamental (50 Hz)	20.52 A	326.4 V	20.58 A	327.1 V
	THD	2.88 %	140.89 %	2.89 %	141.88 %
Discharging mode	Fundamental (50 Hz)	20.43 A	327.6 V	20.69 A	326 V
	THD	2.85 %	138.23 %	2.67 %	141.34 %

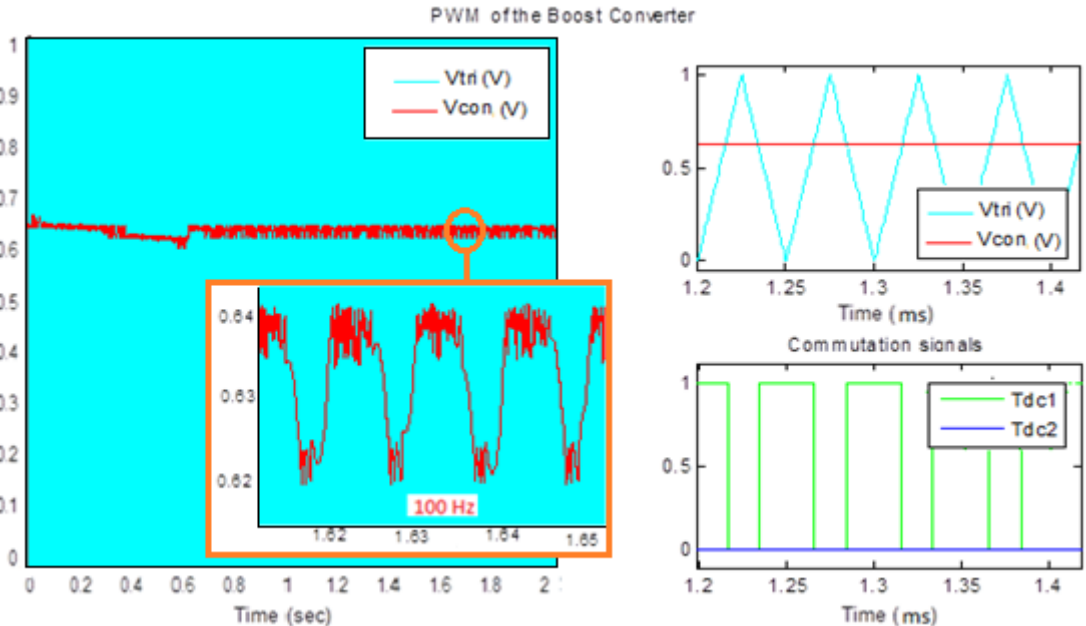
Table 20. FFT Analysis of Igrid and V12 before and after adding a Two-Quadrant converter

Depending on the power flow in the system, the Two-Quadrant converter is working as a Buck or as a Boost converter, so different switches are controlled in each case. The switching patterns for these switches, as well as the PWM for both charging and discharging modes, can be seen in Figure 74. In Figure 75, the reference and actual values of the battery's current and voltage are plotted in order to check that the control is being performed correctly.

The battery's SoC, current, voltage and power in charging mode are shown in Figure 76. It can be noted that now, except for a ripple at the commutation frequency, these parameters are constant. Therefore, the 100 Hz oscillation appearing in the previous case has been eliminated.



(a) Charging mode



(b) Discharging mode

Figure 74. PWM and switching orders for the Two-quadrant converter

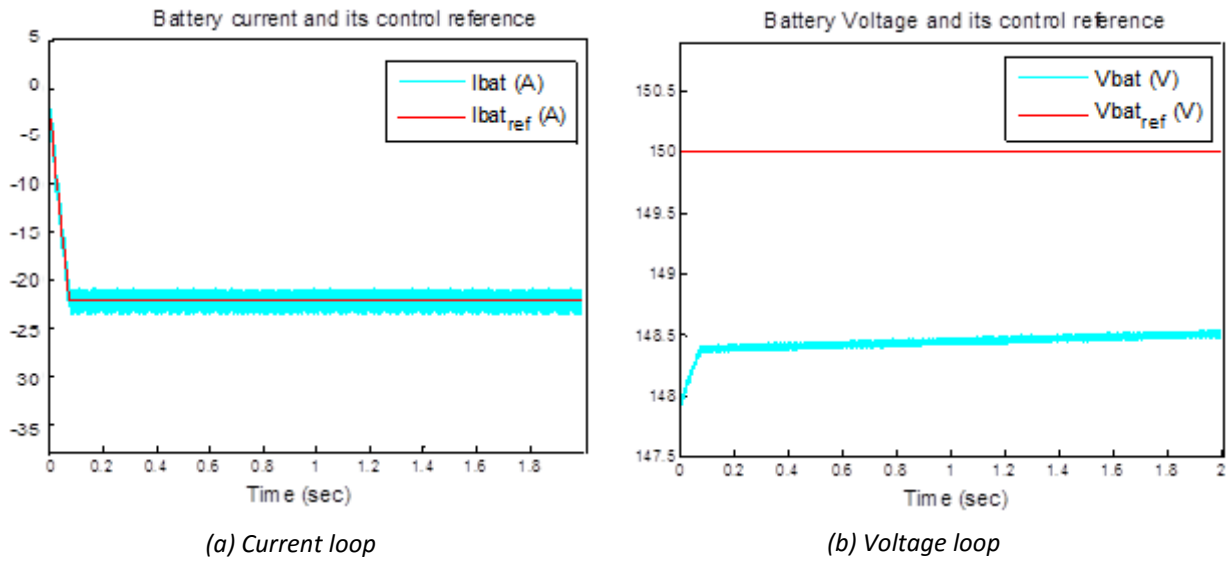


Figure 75. Behaviour of the Two-Quadrant converter's control loops for CV charging mode

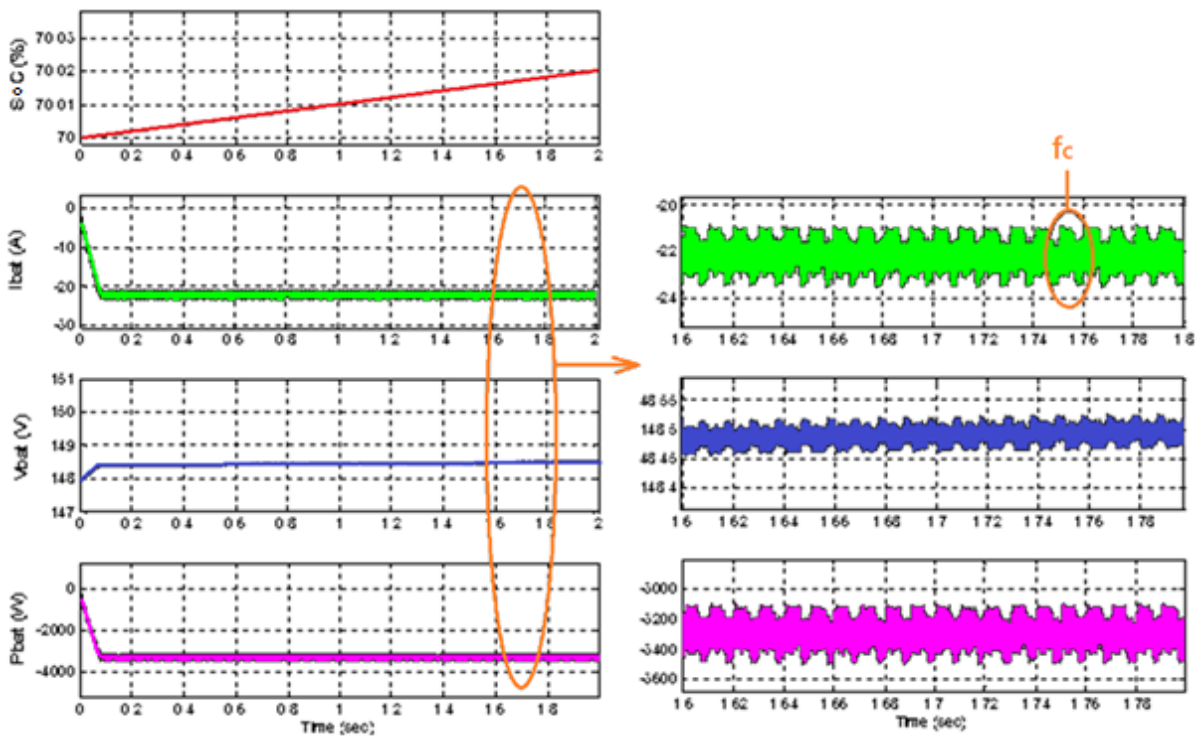


Figure 76. Battery's SoC, current, voltage and power adding a Two-Quadrant converter for CVC

### 5.3. Topology 3: Full Bridge converter for High Power applications

For high power applications, the grid comprises three phases, whose currents are controlled independently. The PWM, control signals and switching orders of this control are plotted in Figure 77. The first branch, composed by IGBTs 1 and 2, is controlled by signal F1; the second branch, with IGBTs 3 and 4, is controlled by signal F2; and the third branch, with IGBTs 5 and 6, is controlled by F3. Having three control signals makes a difference respect to the single-phase systems' control, since

now the phase voltage is obtained using 5 levels, which minimizes the harmonics, while the line voltage is obtained using 3 levels. These voltage levels are better seen in next Section 5.4.

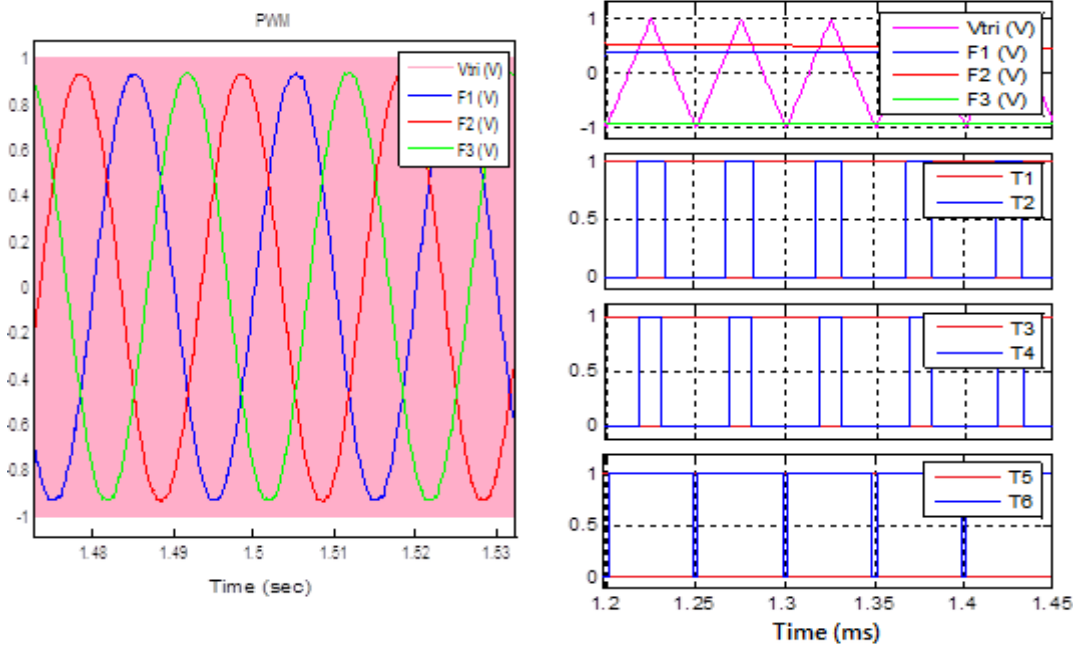
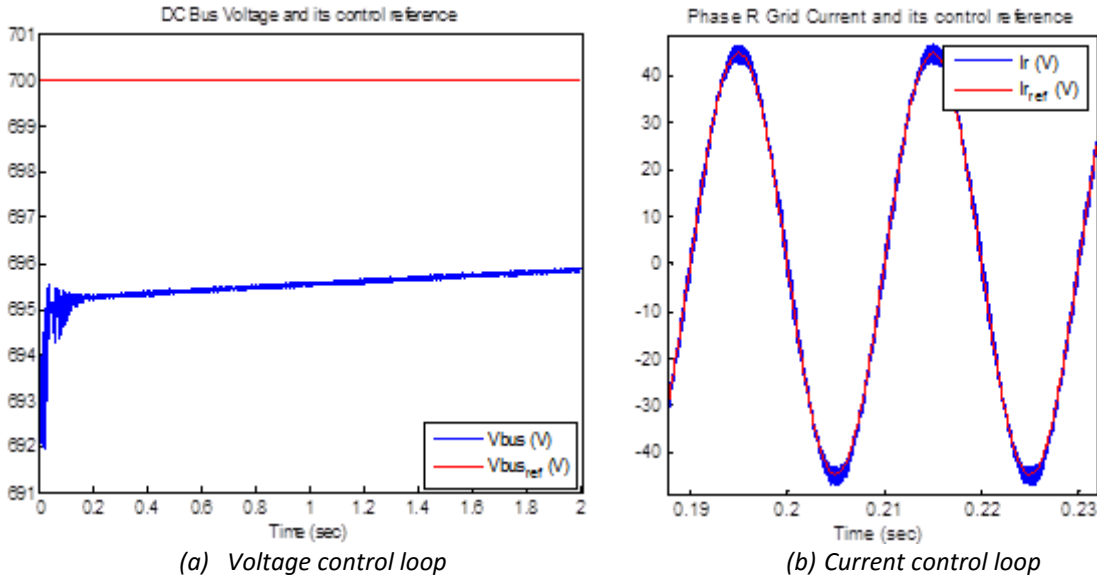


Figure 77. PWM and switching patterns of the 3-phase Full Bridge

In the following lines, some results for Constant Voltage methodology are presented. When charging, the reference voltage introduced is 700 V, whereas it is 670 V when discharging. Figure 78 shows how the actual current and voltage tend to follow their reference, so both the current and voltage control loops are working as expected. Moreover, in Figure 79, the grid currents and voltages are depicted. As in the previous models, the current is considering positive when exiting the battery. It is worth noticing that the current and voltage are synchronized so that the reactive power is zero.



(a) Voltage control loop (b) Current control loop

Figure 78. Behaviour of the Full Bridge's control loops for charging mode



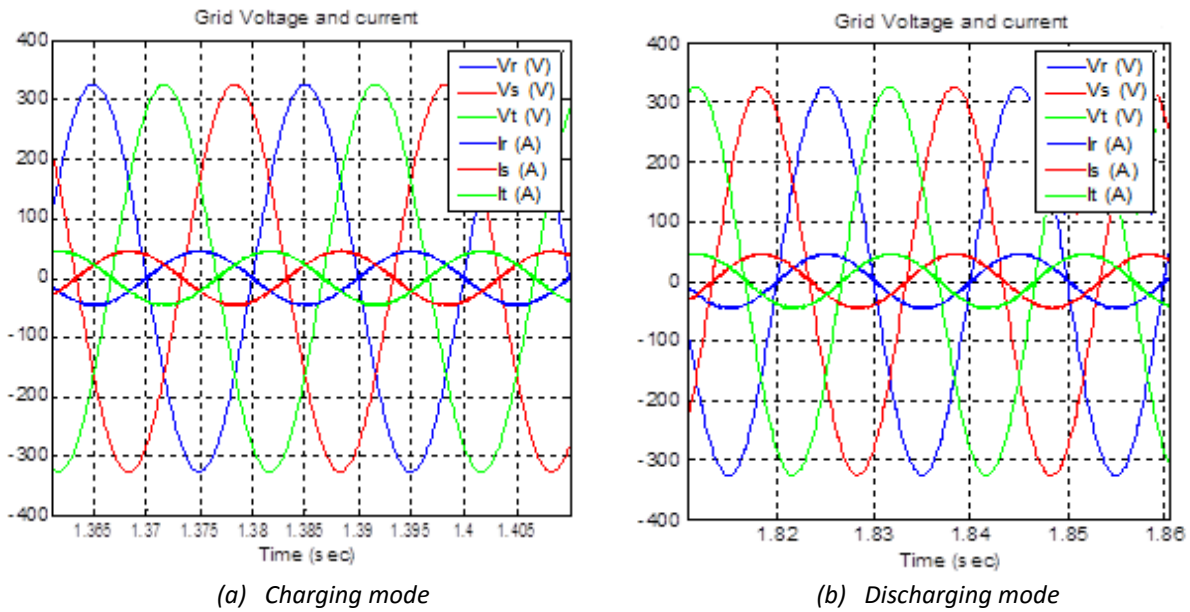


Figure 79. Grid's currents and voltages for CV methodology

In three-phase systems, the power is constant except for a ripple at the commutation frequency. Thus, the 100 Hz oscillation existing in single-phase systems is not present neither in the grid's power nor in the battery's voltage, current or power, as it can be seen in the following Figure 80.

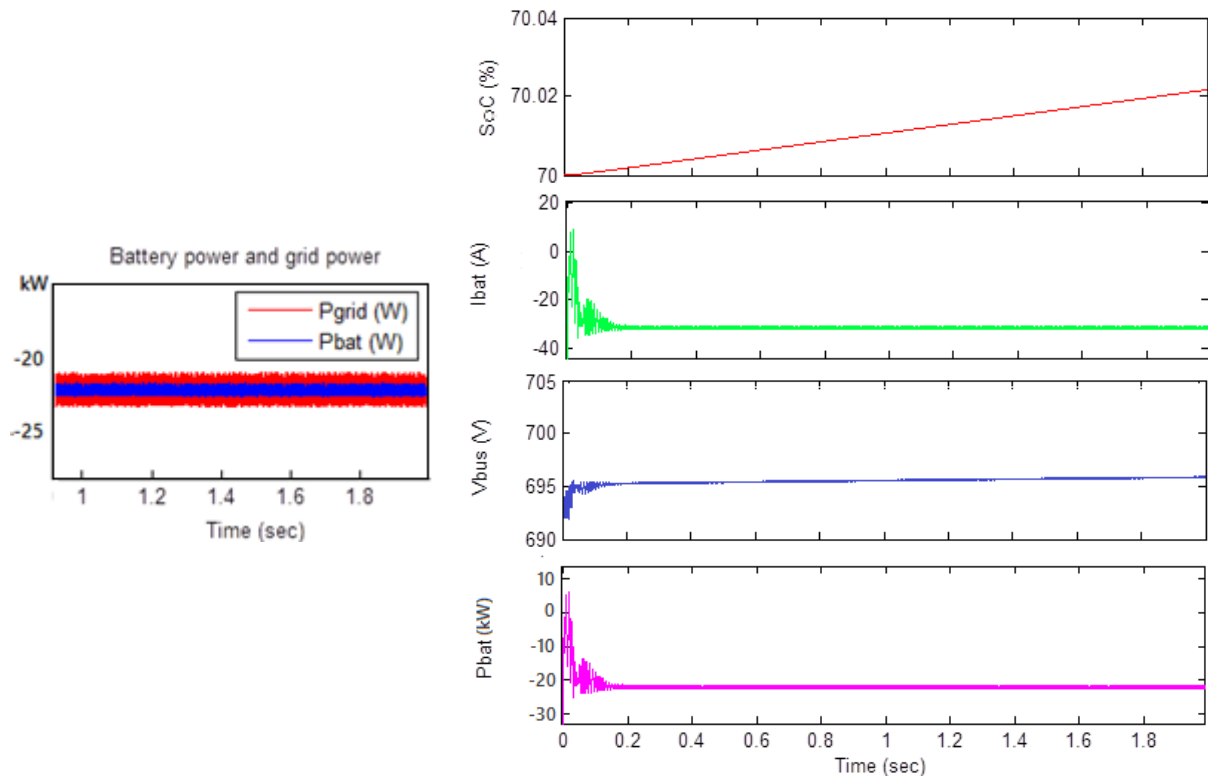


Figure 80. Battery's SoC, current, voltage and power for the 3-phase system for CVC

A FFT analysis has been performed and its results are stored in Table 21. It can be noted that the THD of the AC voltages are similar to those of the single-phase system with unipolar modulation, since in

that case the voltage was also obtained using 3 voltage levels. On the other hand, the harmonics content in the grid currents has increased. For both charging and discharging modes the results obtained are very similar.

		Ir	Is	It	V1n	V2n	V3n	V12	V23	V31
Charging Mode	Fundamental (50 Hz)	45.12 A	45.12 A	45.11 A	326.9 V	326.9 V	326.9 V	566.1 V	566.1 V	566.1 V
	THD	2.65 %	2.63 %	2.66 %	75.16 %	75.16 %	75.16 %	75.16 %	75.16 %	75.16 %
Discharging Mode	Fundamental (50 Hz)	45.18 A	45.18 A	45.16 A	327.5 V	327.5 V	327.5 V	567.2 V	567.2 V	567.2 V
	THD	2.63 %	2.64 %	2.63 %	74.06 %	74.07 %	74.06 %	74.07 %	74.07 %	74.06 %

Table 21. FFT Analysis of the grid currents and AC Voltages for CV methodology

### 5.4. Topology 4: Full Bridge and DC/DC converter for High Power applications

For the purpose of proving the good behaviour of the different charging methodologies implemented in the models, in this case the Constant Current strategy is analysed. As before, the battery is taken as the reference of the system, so that the current is positive in V2G operation. Consequently, when charging, the reference battery current introduced was -120 A; when discharging, it was 120 A.

The grid’s voltage and current for each mode are depicted in Figure 81, where it is visible that they are synchronized so that the PF is 1. The grid current harmonics for charging mode are shown in Figure 82. It has to be noted that the DC currents are high, so that a transformer should be added to the system to avoid the saturation of the grid’s transformers.

For discharging mode, the value of the fundamental of the grid currents is 36.02 A instead of 36.62 A, while the THD is 3.31% instead of 3.26%. This proves that the V2G mode is not more harmful to the grid than the G2V operation.

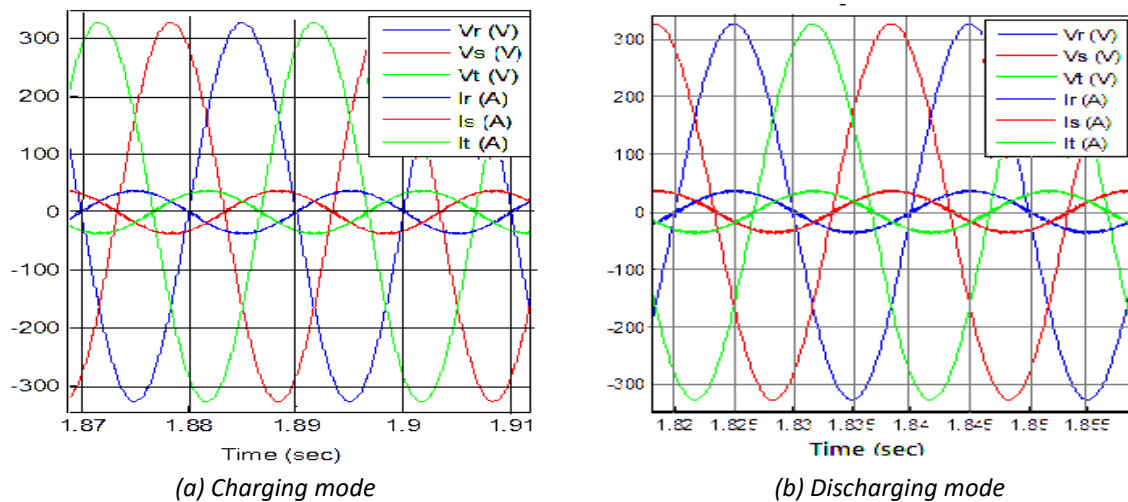
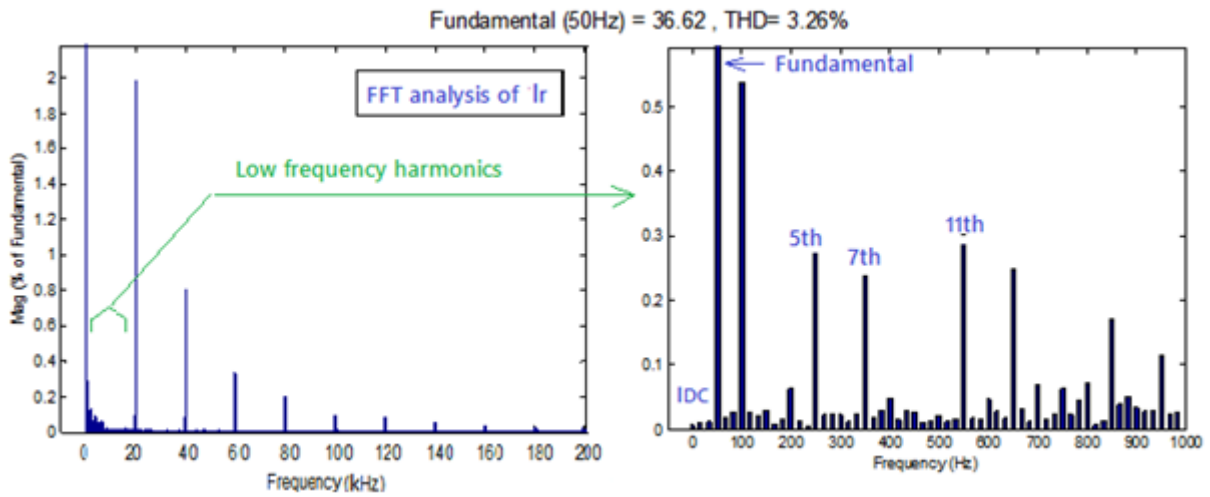
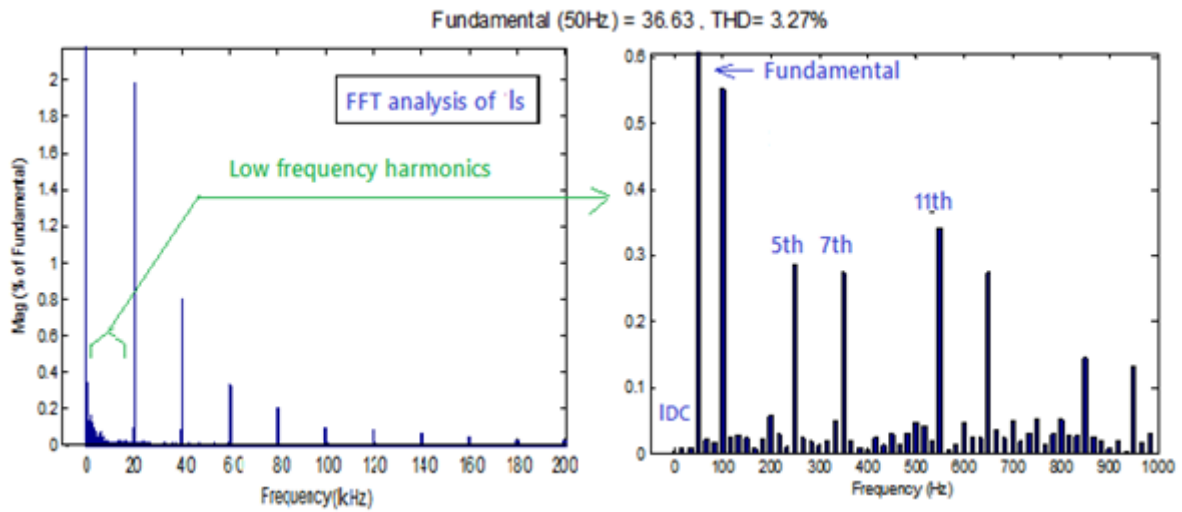


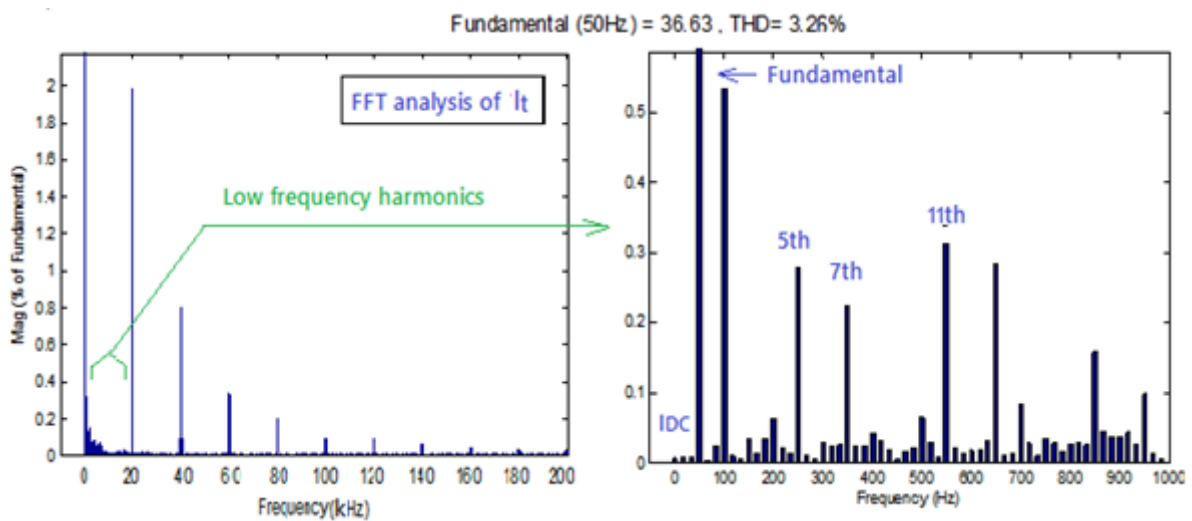
Figure 81. Grid voltages and currents for CC methodology



(a) R-Phase Current



(b) S-Phase Current



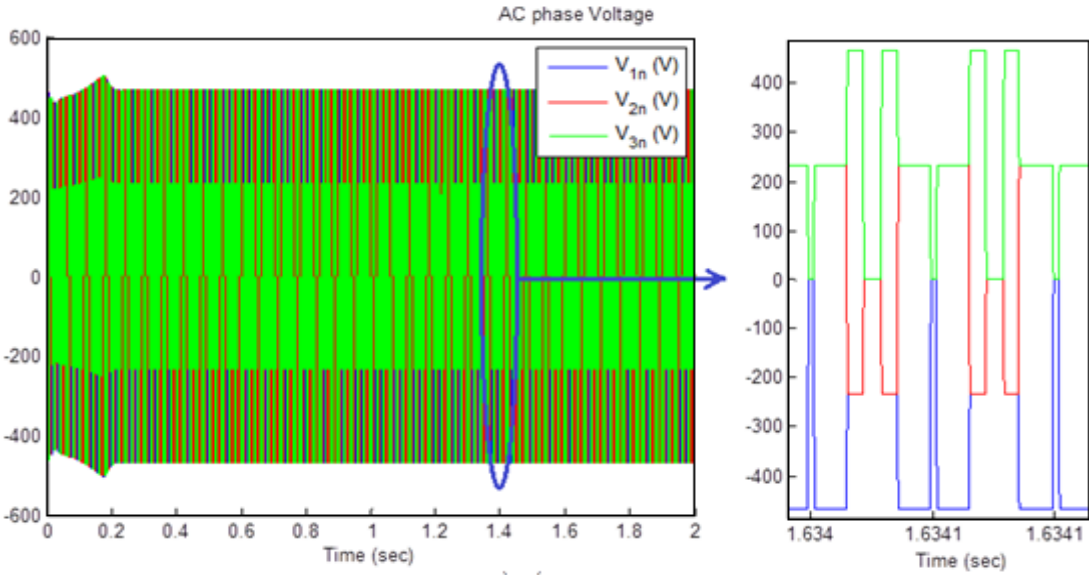
(c) T-Phase Current

Figure 82. Harmonics content of the grid's phase currents for CC charging mode

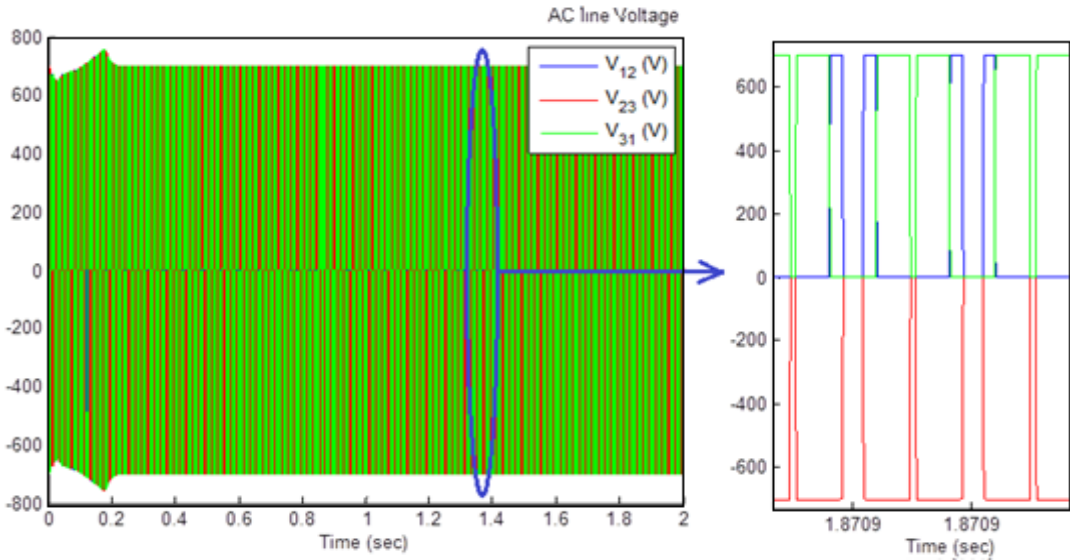
In order to see the influence of adding the Two-Quadrant converter to a three-phase system, a simulation has been carried out using the same charging and discharging properties than in the previous section 5.3. This means that constant voltage methodology has been implemented again.

Afterwards, a FTT Analysis has been performed and its results are stored in Table 22. It can be highlighted that they are very similar to the previous ones, but with a slightly higher THD.

The phase and line AC voltages can be seen in the following Figure 83, where the levels of voltage they can achieve are clearly distinguishable.



(a) Phase Voltage



(b) Line Voltage

Figure 83. Phase and Line AC Voltages for 3-Phase systems

		Ir	Is	It	V1n	V2n	V3n	V12	V23	V31
Charging Mode	Fundamental (50 Hz)	44.77 A	44.78 A	44.77 A	326.9 V	326.9 V	326.9 V	566.2 V	566.2 V	566.2 V
	THD	2.68 %	2.68 %	2.69 %	75.80 %	75.79 %	75.79 %	75.80 %	75.79 %	75.80 %
Discharging Mode	Fundamental (50 Hz)	43.96 A	43.97 A	43.96 A	327.4 V	327.4 V	327.4 V	567.1 V	567.1 V	567.1 V
	THD	2.70 %	2.70 %	2.70 %	75.56 %	75.56 %	75.57 %	75.56 %	75.56 %	75.56 %

Table 22. FFT Analysis of the grid currents and AC Voltages for CV when adding the Two-Quadrant Converter

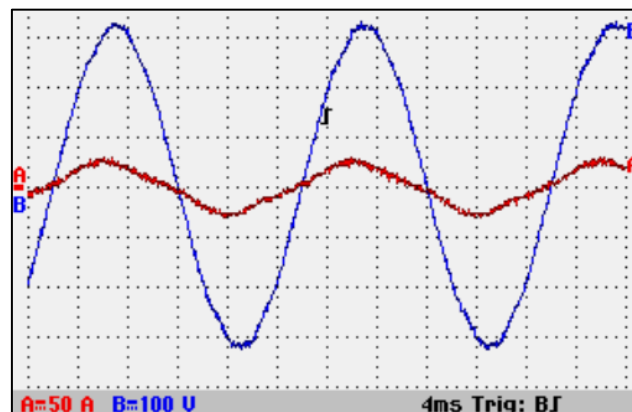
## 5.5. Experimental Analysis of Commercial Vehicle Charger

The last part of the present study consists on showing some real results from a Nissan Leaf in order to show how the G2V technology operates in a real environment. Three different measurements of the State of Charge (SoC), Power, Voltage, Current, Power Factor (PF) and Deformation Factor (DF) were taken while the vehicle was charging. This data is stored in Table 23.

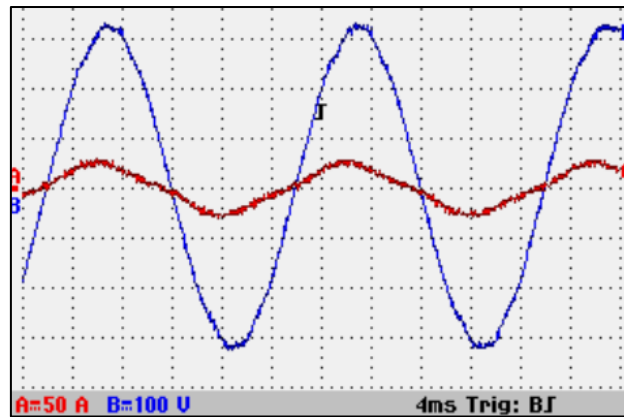
SoC (%)	P (W)	S (VA)	W (Var)	Vrms (V)	Irms (A)	PF	DF	Time
17	3797	3855	-648	225	17	0,985 capacitive	1,25	12:50
31	3661	3715	-631	225,6	16,44	0,985 capacitive	1,1	13:15
42	3741	3797	-655	226,1	16,77	0,985 capacitive	1,1	13:35

Table 23. Measured data from a Nissan Leaf while charging

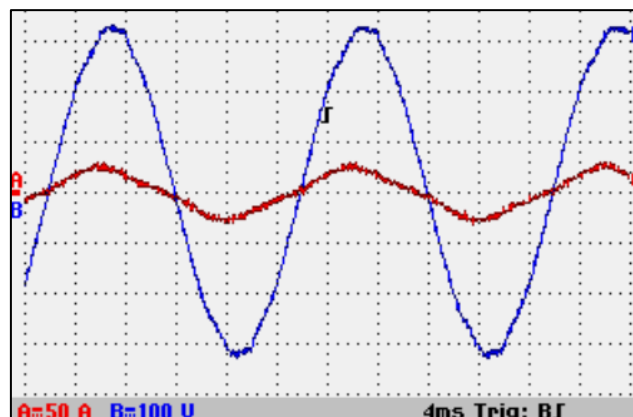
Furthermore, the current and voltage provided at the moment of the measurements are depicted in Figure 84, where signal A is the current and signal B the voltage. It must be noted that the reference in this case, as a difference from the simulations, is the electricity grid. Therefore, the current is considered positive in G2V operation, when it exits the grid.



(a) First measurement at SoC=17%



(b) Second measurement at SoC=31%



(c) Third measurement at SoC=42%

Figure 84. Current and voltage supplied to the Nissan Leaf at various SoC

In all cases, the power factor is capacitive; that means that the current leads the voltage. The value of this PF is very good, very close to 1, independently to the value of the SoC. This means that the Power Factor Correction (PFC) has been implemented correctly.

It can be noted that as the SoC increases, the voltage does, too. This always happens in this kind of electrochemical systems, where the voltage is higher as the system is more charged.

Moreover, it has to be highlighted that for G2V operation, the results from the simulations are very similar to the real ones. Therefore, as positive results were obtained for the V2G operation in the simulation, it can be concluded that the results in a real environment would also be favorable.

## 6. CONCLUSION

The main research topics of this thesis were the design and assessment of four topologies with which the G2V and V2G concepts have been tested. The first two topologies are intended for low power applications, up to 3.3 kW. Topology 1 comprises a Full Bridge converter connected to High Voltage Batteries, whereas Topology 2 counts with the addition of a Two-Quadrant converter and Low Voltage Batteries. On the other hand, the other two topologies are prepared for high power applications, up to 22 kW. Topology 3 comprises a Full Bridge converter while Topology 4 has a Two-Quadrant converter, too. The design of each model included the proper sizing of their elements and the implementation of different control strategies to charge and discharge the batteries.

The simulations have shown that every topology's grid current present too high THD. Following IEC-61000, which regulates Electro-Magnetic Compatibility, the grid side filter proposed is not enough. The suggested solution is to install an LC or LCL filter instead.

Bipolar modulation was utilized for its easy implementation and almost constant common mode voltage, which enables a transformer-less system. Nevertheless, simulations have shown that the DC currents are very high, so that the installation of a transformer is mandatory to avoid the saturation of the grid's transformers. Once the use of a transformer is obligatory, unipolar modulation should be used instead; common mode currents are not a problem having a transformer in the charger's structure, and the DC currents and harmonic content using unipolar modulation are highly reduced. Consequently, a smaller grid side filter could be used.

In Topology 1, a 100 Hz ripple appears at the battery side. This ripple is not beneficial for the battery, since it could be seen as using a pulsing charging methodology, which may affect the State of Health and life span of the battery. The addition of a DC/DC converter, as in Topology 2, eliminates this ripple.

The results for high power applications have shown that obtaining the AC voltage from a higher amount of voltage levels reduces its THD. Thus, the use of multilevel converters could be contemplated.

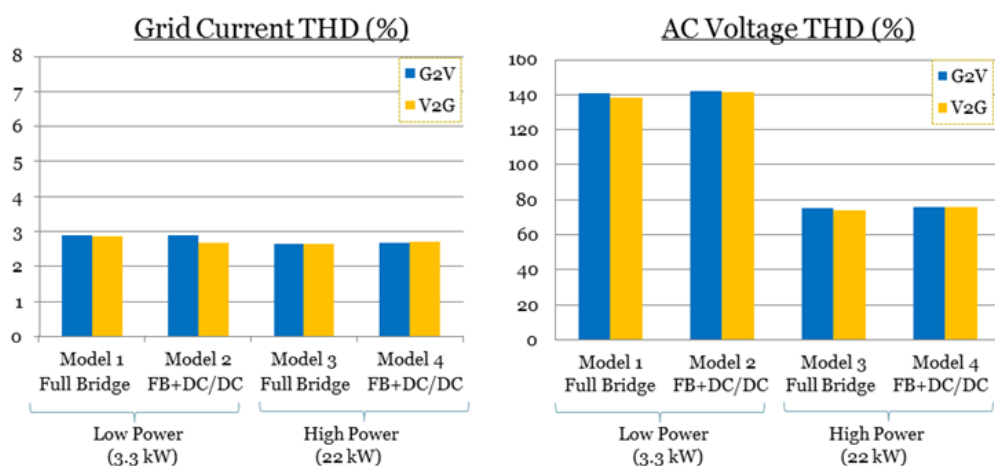


Figure 85. Harmonic content of the grid voltage and current for all the designed topologies

Paying attention to the harmonic content, as stored in Figure 85, it can be concluded that the addition of a DC/DC converter, which provides better control options and enables the use of LV Batteries, does not affect the quality of the power given to or taken from the grid.

Finally, the results of the simulations have been compared to some measurements taken from a real Plug-in Electric Vehicle while charging. As the parameters and waves obtained are very similar for G2V mode, it can be concluded that they will also be very similar for V2G mode. The simulations proved that both G2V and V2G operations have the same affection on the electricity grid. Therefore, since G2V is nowadays being implemented, we conclude that V2G mode could also be implemented and provide its inherent benefits to the grid.



## **7. FUTURE PERSPECTIVE**

In this thesis some models, comprising two different charger's topologies for an Electric Vehicle, were implemented in Matlab/Simulink Platform. Nevertheless, more complicated topologies counting also with a HF Transformer should be studied in the future. This addition would provide a safer environment for the user, thanks to the galvanic isolation achieved, and the overall efficiency of the system could be increased by implementing soft-switching techniques with the help of resonant structures. Furthermore, common mode and DC currents would not be a concern anymore.

On the other hand, the harmonics study carried on these simulated topologies has proved that the calculation and implementation of an LC or LCL filter should be investigated. Another solution for reducing the harmonic content could be using multilevel converters.

In the future, it could be worthy to make an assessment of the system's losses and efficiency.

Moreover, only PI controllers were used in the different controls performed on the systems. However, it would be interesting to check the behaviour of other kind of controllers, such as the HCC and the PRC, and compare the results obtained with each of them.

Finally, after evaluating the most beneficial topology and control simulated, the real implementation of the V2G concept could be realized.



## 8. REFERENCES

- [1] C. C. Chan and K. T. Chau, "An overview of power Electronics in electric vehicles," *IEEE Trans. Ind. Electron.*, vol. 44, no. 1, pp. 3–13, 1997.
- [2] Z. Darabi and M. Ferdowsi, "Aggregated Impact of Plug-In Hybrid Electric Vehicles on Electricity Demand Profile," *IEEE Trans. Sustain. Energy*, vol. 2, no. 4, pp. 319–349, 2011.
- [3] S. G. Wirasingha and A. Emadi, "Pihef: Plug-in hybrid electric factor," *IEEE Trans. Veh. Technol.*, vol. 60, no. 3, pp. 1279–1284, 2011.
- [4] S. Habib, M. Kamran, and U. Rashid, "Impact analysis of vehicle-to-grid technology and charging strategies of electric vehicles on distribution networks - A review," *J. Power Sources*, vol. 277, pp. 205–214, 2015.
- [5] A. Faiz, C. S. Weaver, and M. P. Walsh, "Air pollution from motor vehicles. Standards and Technologies for Controlling Emissions," *Int. Bank Reconstr. Dev.*, vol. 136, pp. 277–301, 1966.
- [6] D. B. Sandalow, *Plug-In Electric Vehicles: What Role for Washington?*, 1st ed. Brookings Institution Press, 2009.
- [7] G4V, "G4V Project - Session II - Impact of Electro-Mobility Electro Mobility on Electricity Networks," pp. 1 – 57, 2011.
- [8] S. Chakraborty, W. Kramer, B. Kroposki, G. Martin, P. McNutt, M. Kuss, T. Markel, and A. Hoke, "Interim Test Procedures for Evaluating Electrical Performance and Grid Integration of Vehicle-to-Grid Applications," *NREL/TP-5500-51001*, no. June, 2011.
- [9] M. Yilmaz and P. T. Krein, "Review of benefits and challenges of vehicle-to-grid technology," *2012 IEEE Energy Convers. Congr. Expo. ECCE 2012*, pp. 3082–3089, 2012.
- [10] E. Keane and D. Flynn, "Potential for electric vehicles to provide power system reserve," *2012 IEEE PES Innov. Smart Grid Technol. ISGT 2012*, no. 09, pp. 1–7, 2012.
- [11] T. Markel, "Plug-in Electric Vehicle Infrastructure: A Foundation for Electrified Transportation," *NREL/CP-540-47951*, no. April, pp. 1–10, 2010.
- [12] E. Barrios, "Unit 3: Conversion stage in single-phase photovoltaic systems." UPNA, Pamplona, 2015.
- [13] P. Denholm and W. Short, "An Evaluation of Utility System Impacts and Benefits of Optimally Dispatched Plug-In Hybrid Electric Vehicles," *NREL Rep. noTP-620-40293*, no. October, p. 41, 2006.
- [14] M. C. Kisacikoglu, B. Ozpineci, and L. M. Tolbert, "Examination of a PHEV bidirectional charger system for V2G reactive power compensation," *Conf. Proc. - IEEE Appl. Power Electron. Conf. Expo. - APEC*, pp. 458–465, 2010.
- [15] M. Yilmaz and P. T. Krein, "Review of battery charger topologies, charging power levels and infrastructure for plug-in electric and hybrid vehicles," *2012 IEEE Int. Electr. Veh. Conf. IEVC 2012*, vol. 28, no. 5, pp. 2151–2169, 2012.
- [16] B. Singh, B. N. Singh, A. Chandra, K. Al-Haddad, A. Pandey, and D. P. Kothari, "A review of three-phase improved power quality ac-dc converters," *IEEE Trans. Ind. Electron.*, vol. 51, no. 3, pp. 641–660, 2004.

- [17] I. Singh, Bhim Senior Member, B. N. Singh, I. Chandra, Ambrish Senior Member, I. Al-haddad, Kamal Senior Member, A. Pandey, and I. Kothari, Dwarka P Senior Member, "A Review of Single-Phase Improved Power Quality AC – DC Converters," *Ieee Trans. Ind. Electron.*, vol. 51, no. 3, pp. 641–660, 2004.
- [18] X. Zhou, S. Lukic, S. Bhattacharya, and A. Huang, "Design and control of grid-connected converter in bi-directional battery charger for plug-in hybrid electric vehicle application," *5th IEEE Veh. Power Propuls. Conf. VPPC '09*, pp. 1716–1721, 2009.
- [19] T. Thiringer, M. Grenier, and M. G. H. Aghdam, "Design of on-board charger for plug-in hybrid electric vehicle," *5th IET Int. Conf. Power Electron. Mach. Drives*, pp. 152–152, 2010.
- [20] L. Solero, "Nonconventional on-board charger for electric vehicle propulsion batteries," *IEEE Trans. Veh. Technol.*, vol. 50, no. 1, pp. 144–149, 2001.
- [21] C. Botsford and A. Szczepanek, "Fast Charging vs . Slow Charging : Pros and cons for the New Age of Electric Vehicles," *Evs24*, no. May, pp. 1–9, 2009.
- [22] L. Tang and G.-J. Su, "A low-cost, digitally-controlled charger for plug-in hybrid electric vehicles," *2009 IEEE Energy Convers. Congr. Expo. ECCE 2009*, pp. 3923–3929, 2009.
- [23] W. Shireen and S. Patel, "Plug-in hybrid electric vehicles in the smart grid environment," *IEEE PES Transm. Distrib. Conf. Expo.*, pp. 1–4, 2010.
- [24] S. Chopra, "Contactless Power Transfer for Electric Vehicle Charging Application," Delft University of Technology, 2011.
- [25] Mennekes, "The solution for Europe : Type 2 charging socket with or without shutter." pp. p1–10, 2013.
- [26] P. Bauer, "Contactless Power Transfer : Inductive charging of EV," *Delf University of Technology*. 2010.
- [27] R. M. Miskiewicz, A. J. Moradewicz, and M. P. Kazmierkowski, "Contactless battery charger with bi-directional energy transfer for plug-in vehicles with vehicle-to-grid capability," *Proc. - ISIE 2011 2011 IEEE Int. Symp. Ind. Electron.*, pp. 1969–1973, 2011.
- [28] C. Mi, "Safely Charging EV and PHEV from the Electricity Grid," no. 313. University of Michigan-Dearborn, Dearborn.
- [29] O. Hegazy, J. Van Mierlo, R. Barrero, P. Lataire, N. Omar, and T. Coosemans, "A comparative study of different control strategies of On-Board Battery Chargers for Battery Electric Vehicles," *2013 Eighth Int. Conf. Exhib. Ecol. Veh. Renew. Energies*, pp. 1–6, 2013.
- [30] O. Hegazy, M. El Baghdadi, J. Van Mierlo, and P. Lataire, "Modeling and analysis of different control techniques of conductive battery chargers for electric vehicles applications," *COMPEL - Int. J. Comput. Math. Electr. Electron. Eng.*, vol. 34, no. 1, pp. 151–172, 2015.
- [31] D. C. Erb, O. C. Onar, and A. Khaligh, "Bi-directional charging topologies for plug-in hybrid electric vehicles," *Conf. Proc. - IEEE Appl. Power Electron. Conf. Expo. - APEC*, pp. 2066–2072, 2010.
- [32] B. Lin, I. Member, D. Chen, and H. Tsay, "Bi-Directional AC/DC Converter based on neutral point clamped," *Sci. Technol.*, pp. 1–6, 2001.
- [33] P. S. Chawda, D. Ahirrao, B. Gaware, P. Kakade, and P. Kharade, "Analysis Of Single Phase

- Matrix Converter,” vol. 4, no. 3, pp. 856–861, 2014.
- [34] H. R. Karshenas, H. Daneshpajooch, A. Safaee, P. Jain, and A. Bakhshai, “Bidirectional DC-DC Converters for Energy Storage Systems,” *Energy Storage Emerg. Era Smart Grids*, pp. 161–178, 2011.
- [35] B. Bell, “Introduction to push-pull and cascaded power converter topologies,” *Natl. Semicond. Online Semin.*, pp. 1–44, 2003.
- [36] Y. Du, S. Lukic, B. Jacobson, and A. Huang, “Review of high power isolated bi-directional DC-DC converters for PHEV/EV DC charging infrastructure,” *IEEE Energy Convers. Congr. Expo. Energy Convers. Innov. a Clean Energy Futur. ECCE 2011, Proc.*, pp. 553–560, 2011.
- [37] H. Li, S. Member, F. Z. Peng, S. Member, J. S. Lawler, and S. Member, “A Natural ZVS High-Power Bidirectional DC – DC Converter With Minimum Number of Devices,” vol. 39, no. 2, pp. 525–535, 2003.
- [38] Focus Group on European Electro-Mobility, “Standardization for road vehicles and associated infrastructure - Report in response to Commission Mandate M/468 concerning the charging of electric vehicles,” *October*, no. October, p. 155, 2011.
- [39] M. Garcés and M. Alonso, “Resonant Power Converter for Fuel Cells: Analysis, Design and Simulation,” Public University of Navarra, 2014.
- [40] B. Koushki, A. Safaee, P. Jain, and A. Bakhshai, “A Bi-Directional Single-Stage Isolated AC-DC Converter for EV charging and V2G,” pp. 36–44, 2015.
- [41] A. Damiano, G. Gatto, I. Marongiu, M. Porru, and A. Serpi, “Vehicle-to-Grid Technology: State-of-the-Art and Future Scenarios,” *J. Energy Power Eng.*, vol. 8, no. 1, pp. 152–165, 2014.
- [42] A. . Fallis, “Honda Joins Vehicle-to-grid Technology Demonstration Project in Partnership with University of Delaware and NRG Energy,” *J. Chem. Inf. Model.*, vol. 53, no. 9, pp. 1689–1699, 2013.
- [43] A. Ursua, “Unit C: Electrochemical systems: Basic aspects about batteries.” UPNA, Pamplona, 2015.
- [44] C.-C. H. C.-C. Hua and M.-Y. L. M.-Y. Lin, “A study of charging control of lead-acid battery for electric vehicles,” *ISIE’2000. Proc. 2000 IEEE Int. Symp. Ind. Electron. (Cat. No.00TH8543)*, vol. 1, pp. 135–140, 2000.
- [45] R. Marschalko and C. Elöd, “PWM AC-to-DC Converter Performances Improvement with the Help of Hysteresis Control,” *Acta Electroteh.*, vol. 45, no. 5, pp. 561–567, 2004.
- [46] E. Barrios, “Unit 4: Control of the photovoltaic conversion stage.” UPNA, Pamplona, 2015.
- [47] N. Weise, “DQ current control of a bidirectional, isolated, single-stage AC-DC converter for vehicle-to-grid applications,” *IEEE Power Energy Soc. Gen. Meet.*, pp. 0–4, 2013.
- [48] O. Hegazy, J. Van Mierlo, and P. Lataire, “Design and Control of Bidirectional DC/AC and DC/DC Converters for Plug-In Hybrid Electric Vehicles,” *Proc. 2011 Int. Conf. Power Eng. Energy Electr. Drives*, no. May, pp. 1–7, 2011.
- [49] M. Bhardwaj, “Modeling Bi-Directional Bcuk/Boost Converter for Digiteal Control Using C2000 Microcontrollers,” *Texas Instruments Inc. Appl. Rep. SPRABX5*, no. January, pp. 1–12, 2015.

- [50] L. Marroyo, "Three-Phase Inverter: Sizing and Scalar Control." UPNA, Pamplona, 2015.
- [51] L. Marroyo and J. Marcos, "Unit 4. DC/DC Converters." UPNA, pp. 87–176, 2015.
- [52] L. Marroyo, "Unit 4. Digital Control." UPNA, Pamplona, pp. 119–125, 2015.

# APPENDIX

## A. Elements Calculation

### 1. Topology 1: Full Bridge converter for Low Power applications

As the Full Bridge (FB) is a voltage reducer, in order to introduce power in the electricity grid the minimum  $V_{bus}$  permitted is calculated using equation (1.1), as in [12], where the voltage drop in the grid side inductor is negligible.

$$V_{bus,min} = \frac{\sqrt{2} \cdot \sqrt{V_{grid,rms}^2 + (\omega \cdot L_{grid} \cdot I_{grid})^2}}{M_{max}} \cong V_{grid,peak} = 325.27 V \quad (1.1)$$

Thus, the nominal voltage chosen for the DC-Bus is  $V_{bus,nom} = 400 V$ .

The maximum current ripple allowed is 10%. In order to calculate it, firstly the peak value of the grid current has to be calculated using equation (1.2). Afterwards, the value of the maximum ripple is calculated with equation (1.3).

$$I_{grid,peak} = \sqrt{2} \cdot I_{grid,max,rms} = \sqrt{2} \cdot \frac{P_{max}}{V_{grid,rms}} = 20.29 A \quad (1.2)$$

$$\Delta i_{grid,max} = 0.1 \cdot I_{grid,peak} = 2.03 A \quad (1.3)$$

Provided the constraint of the maximum current ripple, the minimum grid side's inductor needed, using bipolar modulation, is obtained by equation (1.4), as in [12].

$$L_{grid} \geq \frac{V_{bus}}{2 \cdot \Delta i_{grid} \cdot f_c} = 4.93 mH \quad (1.4)$$

Single phase systems provide a very oscillating power at 100 Hz. Consequently, the battery's current and voltage also have this mentioned ripple. For the purpose of minimizing this oscillation, the investigation team of the ETEC Department at the VUB built a system comprising a battery side's inductor of 10 mF and capacitor pack composed by nine parallel-connected 4.7 mF capacitors. Based on the positive results obtained with this experiment, the previous values were taken for this topology's simulations during this thesis.

The nominal voltage of a battery cell is 3.6 V. In order to have a voltage of 400 V, the number of cells connected in series ( $N_s$ ) to form one string is 102. This value was checked in the simulations.

The maximum current delivered by the battery corresponds to the maximum power of the charger, and it can be calculated using equation (1.5).

$$I_{Lmax} = \frac{P_{max}}{V_{bat}} = 8.25 A \quad (1.5)$$

As the nominal capacity of each battery cell is 10 Ah, only one string is needed to provide the maximum current. Thus,  $N_p$  is equal to 1.

## 2. Topology 2: Full Bridge and DC/DC converter for Low Power applications

In this case, the nominal voltage of the battery is 150 V, while the nominal DC-Bus Voltage is 400 V. As the battery voltage is lower, the number of cells in each string is reduced to  $N_s$  equal to 38. This value has been proved as correct to provide 150 V during simulation.

The maximum current through the inductor in the battery side is constrained by the maximum power of the charger. Using equation (1.5), this maximum value is 22 A. To be able to provide this current, the battery must be composed by at least 3 strings; that is,  $N_p$  is equal to 3.

After adding the DC/DC Converter, the 100 Hz ripple in the bus voltage is not relevant because it is not seen in the battery side. Therefore, the value of the DC-Bus capacitor does not need to be as large as in Topology 1. The criteria used to calculate this value is based on the maximum voltage ripple allowed. Limiting it to 2 %, the minimum capacitor needed is calculated with equation (2.1), as in [12].

$$C_{bus} \geq \frac{P_{AC}}{\Delta V_{bus} \cdot \omega_{grid} \cdot V_{bus}} = 3.28 mF \quad (2.1)$$

Equation (2.2) expresses the calculation of the maximum current ripple in the battery side, which is 20%. Given this value, the battery side's inductor is obtained using equation (2.3), as in [12].

$$\Delta i_{Lmax} = 0.2 \cdot I_{Lmax} = 4.4 A \quad (2.2)$$

$$L_{bat} \geq \frac{V_{bus}}{4 \cdot f_c \cdot \Delta i_{Lmax}} = 1.136 mH \quad (2.3)$$

The value of the battery side capacitor can be obtained with two different considerations, as explained in [51]: taking into account the maximum voltage ripple permitted, as calculated using equation (2.4), or considering the battery side LC filter's frequency, as done using equation (2.5).

$$C_{bat} \geq \frac{\Delta i_{Lmax}}{8 \cdot \Delta V_{max} \cdot f_c} = 55 \mu F \quad (2.4)$$



$$\omega_{filterLC} = \frac{1}{\sqrt{L_{bat} \cdot C_{bat}}} = \frac{2\pi \cdot f_c}{100} = 400\pi \text{ rad/s} \rightarrow C_{bat} = 0.5574 \text{ mF} \quad (2.5)$$

The most restrictive value is the obtained with equation (2.5), so the capacitor must be bigger than 0.5574 mF.

### 3. Topology 3: Full Bridge converter for High Power applications

Now that the power of the charger has increased and the system comprises three phases, the maximum current of the grid can be calculated using equation (3.1).

$$I_{phase,peak} = \sqrt{2} \cdot I_{phase,rms} = \sqrt{2} \cdot \frac{P_{3\phi}}{3 \cdot V_{phase,rms}} = 45.09 \text{ A} \quad (3.1)$$

The maximum ripple allowed for this current is 10 %. Using equation (1.3), this value is 4.51 A. As in [50], the biggest ripple occurs when the grid voltage crosses the zero, moment at which the duty cycles of the three branches can be expressed as in equations (3.2), (3.3) and (3.4):

$$\alpha_1 = \frac{T_{on1}}{T_c} = \frac{V_{tri} + v_{con1}}{2V_{tri}} = \frac{V_{tri} + M_{max} \text{sen}(0)}{2V_{tri}} = 0,5 \quad (3.2)$$

$$\alpha_2 = \frac{T_{on2}}{T_c} = \frac{V_{tri} + v_{con2}}{2V_{tri}} = \frac{V_{tri} + M_{max} \text{sen}\left(-\frac{2\pi}{3}\right)}{2V_{tri}} \approx 0,086 \quad (3.3)$$

$$\alpha_3 = \frac{T_{on3}}{T_c} = \frac{V_{tri} + v_{con3}}{2V_{tri}} = \frac{V_{tri} + M_{max} \text{sen}\left(+\frac{2\pi}{3}\right)}{2V_{tri}} \approx 0,911 \quad (3.4)$$

Another way of obtaining the maximum current ripple is using equation (3.5), as presented in [50]. Operating this equation, the grid side inductor can be calculated using equation (3.6).

$$\Delta i_{max} = \frac{2}{3} V_{bus} \frac{1}{L_{grid}} \Delta T = \frac{2}{3} V_{bus} \frac{1}{L_{grid}} \frac{T_c}{2} (\alpha_1 - \alpha_2) = \frac{\sqrt{3} M_{max}}{12} \frac{V_{bus}}{V_{tri}} \frac{1}{6.9 \cdot L_{grid} \cdot f_c} \quad (3.5)$$

$$L_{grid} \geq \frac{V_{bus}}{6.9 \cdot \Delta i_{max} \cdot f_c} = 4.93 \text{ mH} \quad (3.6)$$

The minimum voltage needed in the DC-Bus in order to provide power to the grid can be calculated using equation (3.7), developed in [50].

$$V_{bus,min} = \frac{\sqrt{8} \cdot V_{tri} \cdot \sqrt{V_{phase}^2 + (\omega \cdot L \cdot I_r)^2}}{M_{max}} = 651.28 \text{ V} \quad (3.7)$$

The nominal voltage chosen for the DC bus is 700 V.

The next step consists on choosing the appropriate value for the DC-Bus capacitor, which is the one that limits the variations in the Bus Voltage. This variation can be caused by three different reasons [50]:

1. High frequency harmonics due to the commutation of the converter;
2. Low frequency harmonics due to the battery;
3. Load changes, when the current changes hastily.

Normally the third cause produces the biggest variation of voltage, so if the capacitor is big enough to limit this variation, it will satisfactorily limit the other two variations. This third variation is dependent to the DC-Bus voltage control loop velocity; the faster it reacts to charges in the Bus Voltage, the smaller the capacitor can be. However, this fastness is limited by the velocity of the outer current loop.

The transfer function between the measured and filtered Bus Voltage ( $V_{DC,mf}$ ) and the DC Current is obtained in equation (3.8), developed in [50], after considering  $V_{DC,ref}$  equal to 0. It is a second order system.

$$\frac{V_{DC,mf}}{I_{DC}} = \frac{1}{\left( \frac{Cs}{K_{sv}} + \left( K_p + \frac{K_i}{s} \right) \frac{1}{K_{si}} \right)} = \frac{K_{sv} K_{si} s}{(K_{si} C s^2 + K_p K_{sv} s + K_{sv} K_i)} = \frac{K_{sv} s}{\left( C s^2 + K_p \frac{K_{sv}}{K_{si}} s + \frac{K_{sv}}{K_{si}} K_i \right)} \quad (3.8)$$

In [50], the PM and Kp of the PI controller are expressed as a function of the cross-over frequency and the Bus Capacitor, as seen in equations (3.9) and (3.10):

$$T_n = \frac{tg(PM)}{\omega_{cv}} \quad (3.9)$$

$$K_p = \frac{T_n K_{si} C \omega_{cv}^2}{K_{sv} \sqrt{(T_n \omega_{cv})^2 + 1}} \quad (3.10)$$

In [50], a Phase Margin of 60° is introduced in the previous equations, even if another value does not affect the results significantly. The PI parameters can be consequently expressed as in equations (3.11), (3.12) and (3.13).

$$T_n = \frac{1.73}{\omega_{cv}} \quad (3.11)$$

$$K_p = \frac{\frac{K_{si}}{K_{sv}} C \omega_{cv}}{1,154} \quad (3.12)$$

$$K_i = \frac{\frac{K_{si}}{K_{sv}} C \omega_{cv}^2}{2} \quad (3.13)$$

Including these parameters on equation (3.8), the transfer function between  $V_{bus}$  and  $I_{DC}$ , obtained in [50], is seen in equation (3.14):

$$\frac{V_{DC\ m,f}}{I_{DC}} = \frac{K_n V_{DC}}{I_{DC}} = \frac{K_n s}{\left( C s^2 + \frac{C \omega_{cv}}{1,154} s + \frac{C \omega_{cv}^2}{2} \right)} \rightarrow \frac{V_{DC}}{I_{DC}} = \frac{s}{\left( C s^2 + \frac{C \omega_{cv}}{1,154} s + \frac{C \omega_{cv}^2}{2} \right)} = \frac{s}{\frac{C \omega_{cv}^2}{2} \left( \frac{2C}{\omega_{cv}^2} s^2 + \frac{1,73}{\omega_{cv}} s + 1 \right)} \quad (3.14)$$

Taking into account the typical time response of a second order system, the maximum overvoltage that occurs for a load change of  $\Delta I_{DC}$  is presented in [50] as in equation (3.15).

$$\Delta V_{DC\_max} = \Delta I_{DC} \frac{0,494}{C \omega_n} = \Delta I_{DC} \frac{0,698}{C \omega_{cv}} \quad (3.15)$$

Limiting this maximum variation to 2% of the nominal Bus Voltage (that is 14 V) and considering a load variation from 0 to 100 %, as calculated in equation (3.16), the minimum value of the bus capacitor is obtained using equation (3.17), as presented in [50].

$$\Delta I_{DC} (0 \rightarrow 100\%) = I_{DC} (100\%) = 31.43 A \quad (3.16)$$

$$C_{bus} \geq \frac{0,698 \cdot \Delta I_{DC}}{\Delta V_{bus,max} \cdot \omega_{cv}} = 2.494 mF \quad (3.17)$$

In order to divide the DC-Bus Voltage in two equal voltages, in [50] the DC-Bus capacitor is divided by two and each of the resulting capacitors have a resistor  $R_{bus}$  in parallel. The value of these resistors, as calculated in equation (3.18), is very high so that the current through them is minimal.

$$R_{bus} (M\Omega) = \frac{2V_{max} - V_{bus}}{1500 \cdot C_{bus} \cdot V_{bus}} = 0.2864 M\Omega \quad (3.18)$$

On the other hand, in order to provide the maximum DC current obtained in equation (3.16), the minimum number of strings needed in the battery is 4. Moreover, it can be noted that to provide 700 V, the number of cells of each string of the battery must be higher than in Topology 1 and 2. It has been proved in the simulations that the proper number of cells composing each string is 178.

#### **4. Topology 4: Full Bridge and DC/DC converter for High Power applications**

As the battery's nominal voltage is the same than for Topology 2, the number of cells  $N_s$  of each string is again 38. Nevertheless, as the power has increased, the maximum DC current that the battery has to provide is bigger. Using equation (1.5), the value obtained is 147.6 A. In this case the number of strings  $N_p$  needed in parallel is 17, as proved with the simulations.

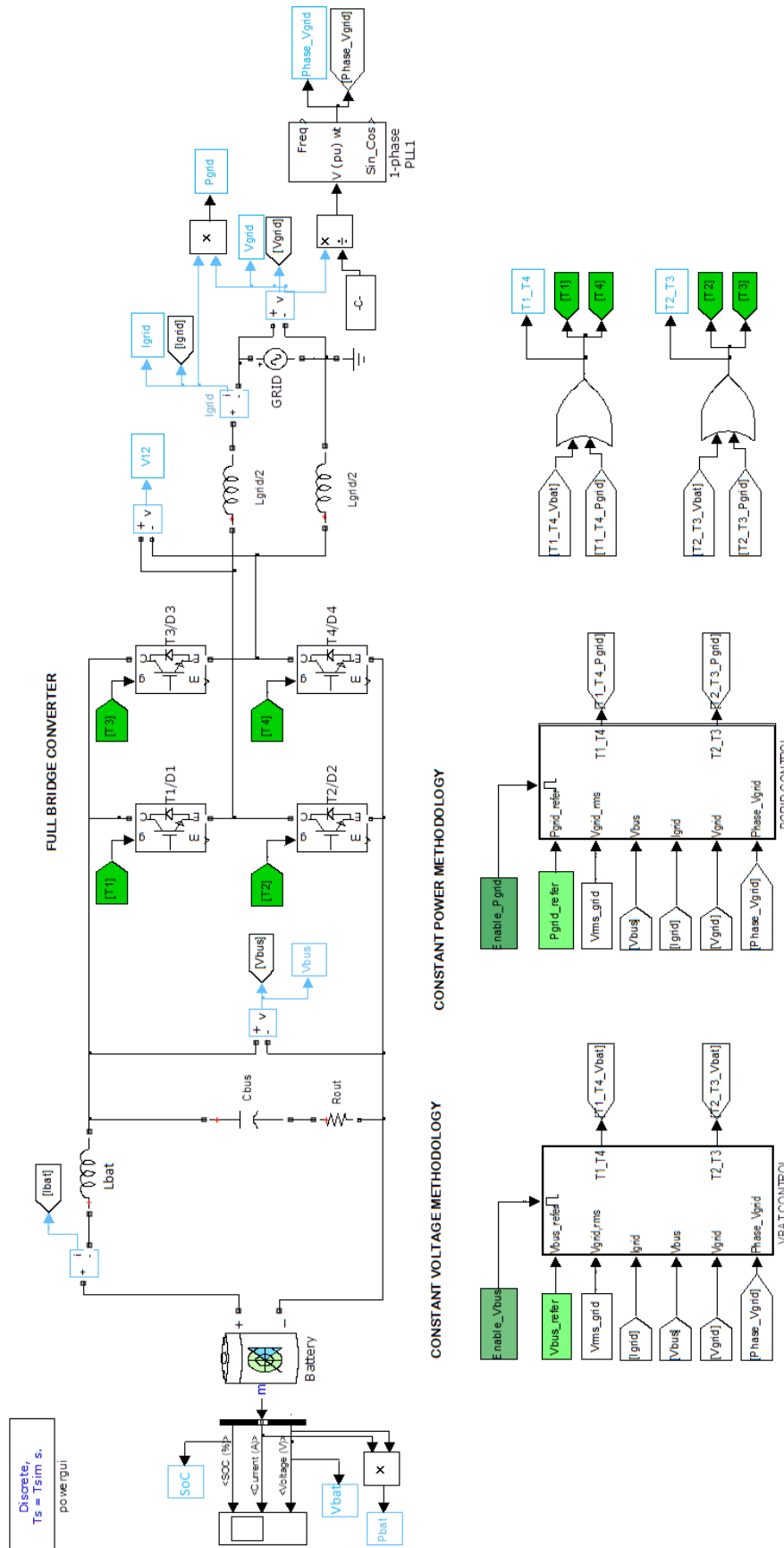
The maximum current ripple in this model is 5%, which corresponds to 7.38 A. This value can be obtained adapting equation (2.2) to this new percentage. The battery side inductor is 1.186 mH, calculated using equation (2.3).

As in Topology 2, the battery side capacitor can be obtained in two different ways. Regarding the maximum voltage ripple permitted and using equation (2.4), the capacitor must be bigger than 92.25  $\mu\text{F}$ . On the other hand, based on the battery side's LC filter, using equation (2.5), the value calculated is 133  $\mu\text{F}$ . As the most restrictive value is the obtained with the second consideration, the value taken for the capacitor is 133  $\mu\text{F}$ .

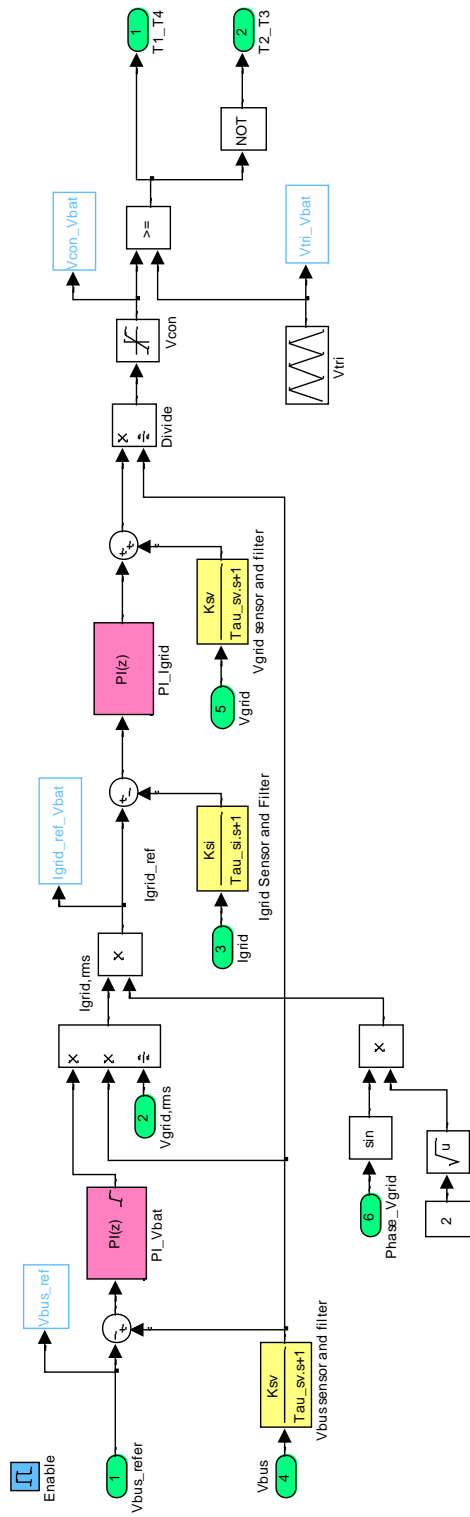
### **B. Modeling of V2G and G2V systems**

The four models of the topologies implemented during this thesis are shown below. Both the converters and the control strategies can be observed.

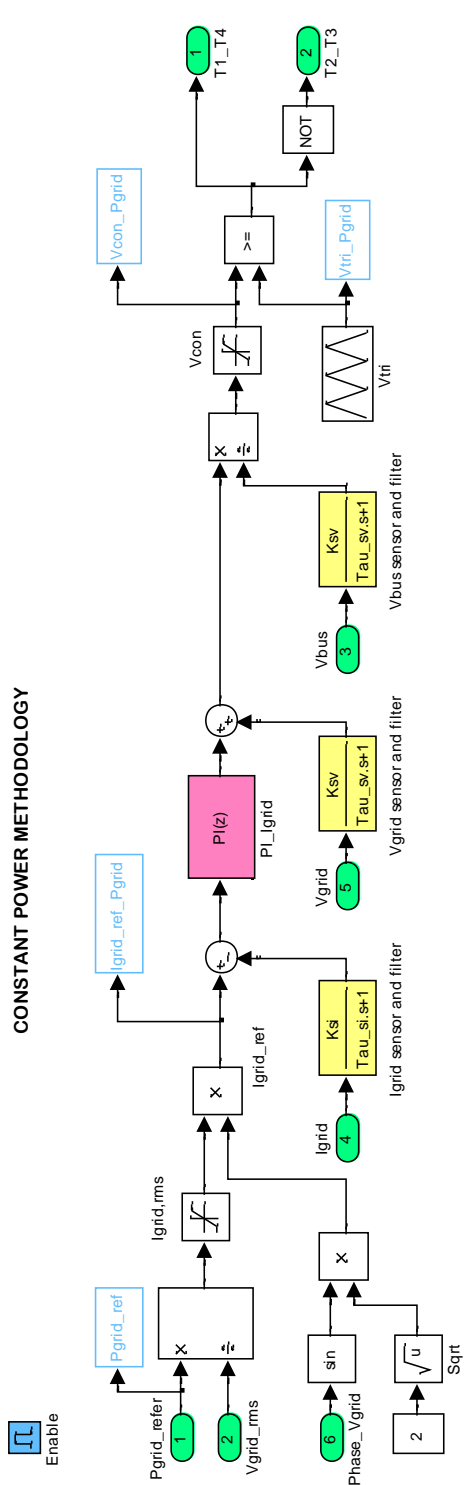
# Topology 1: Modeling of Full Bridge converter for Low Power applications



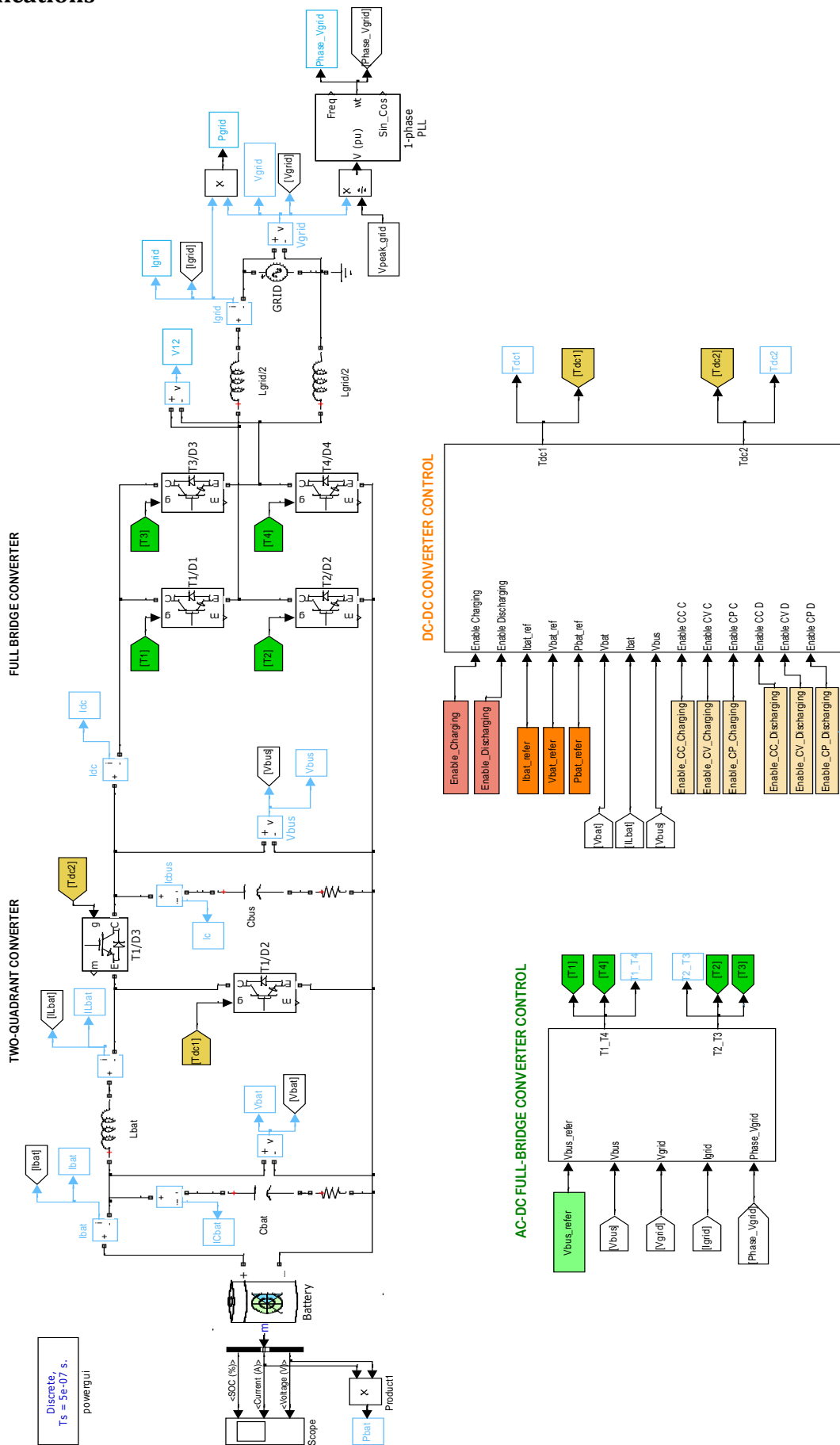
### CONSTANT VOLTAGE METHODOLOGY



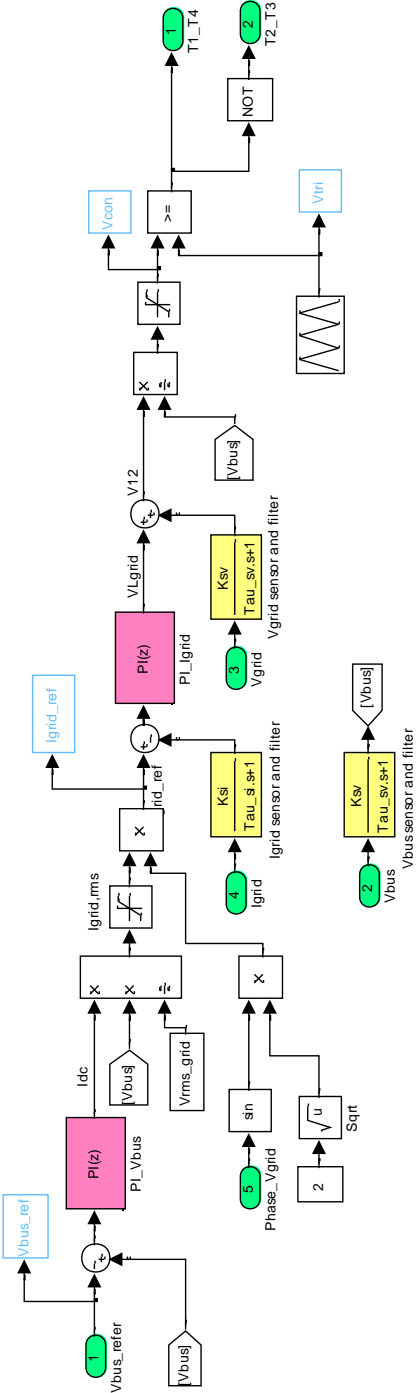
### CONSTANT POWER METHODOLOGY



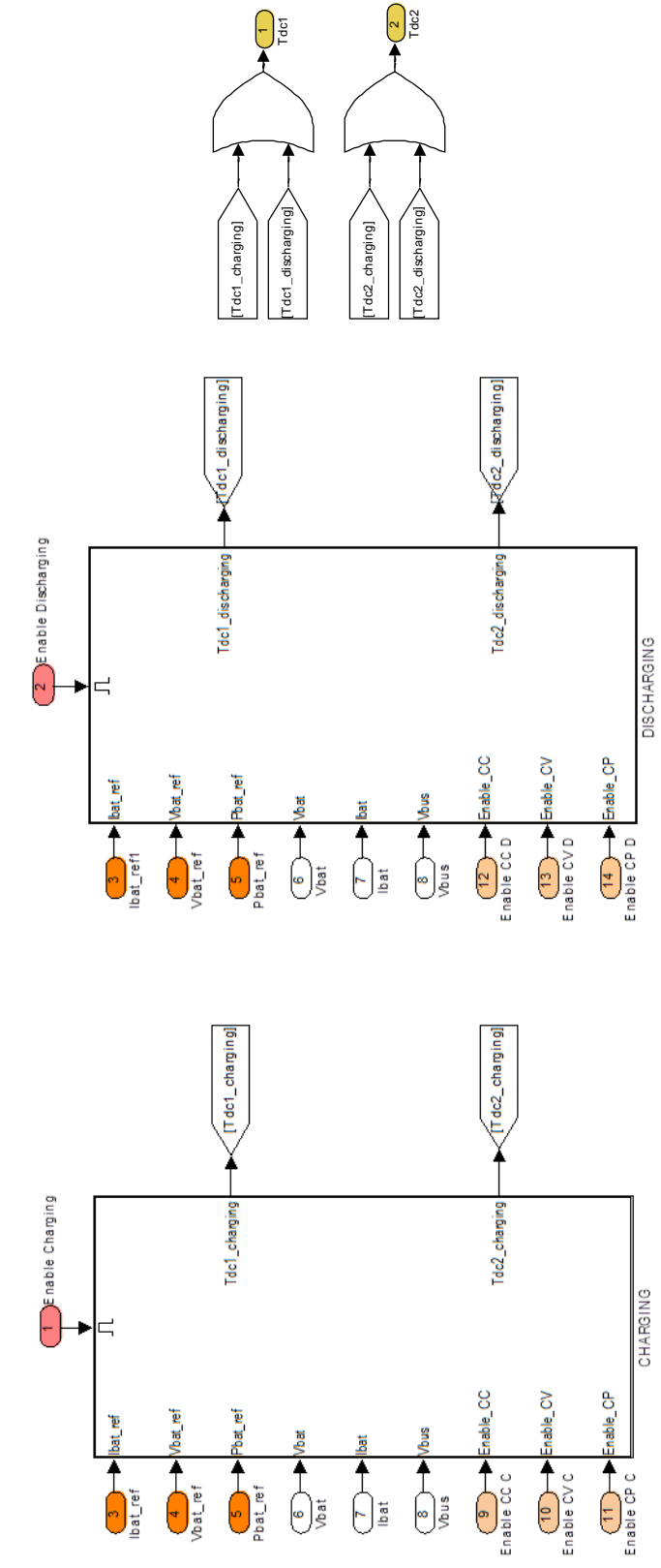
# Topology 2: Modeling of Full Bridge and DC/DC converter for Low Power applications



# AC-DC FULL-BRIDGE CONVERTER CONTROL

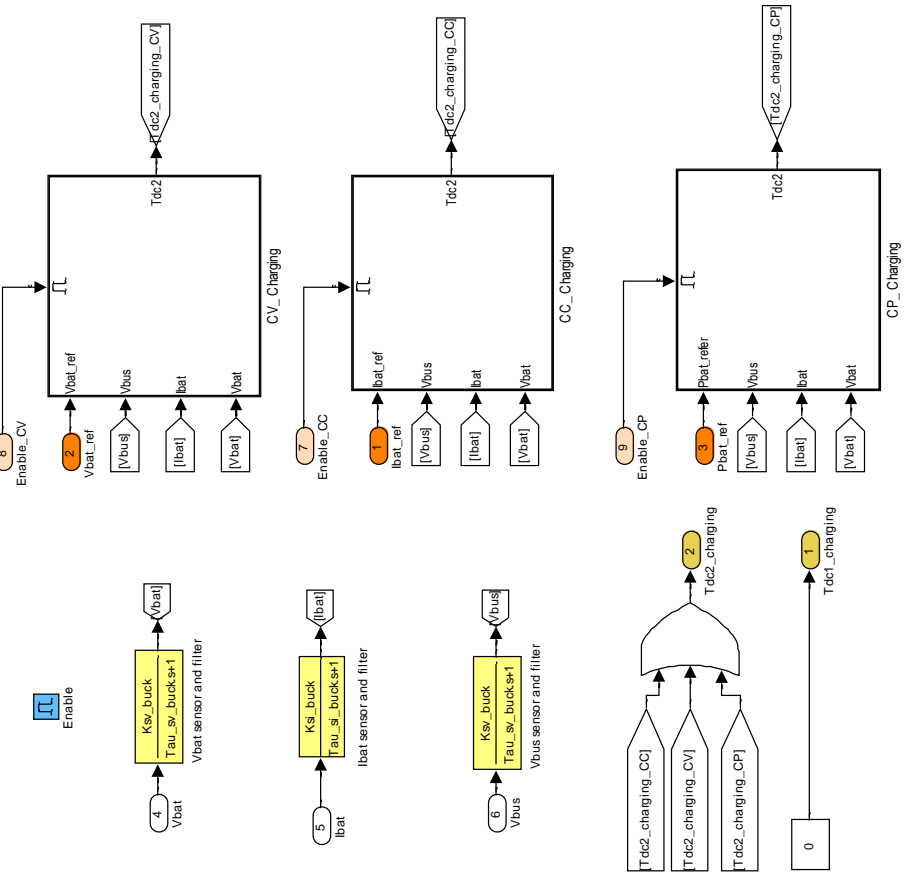


# DC-DC CONVERTER CONTROL

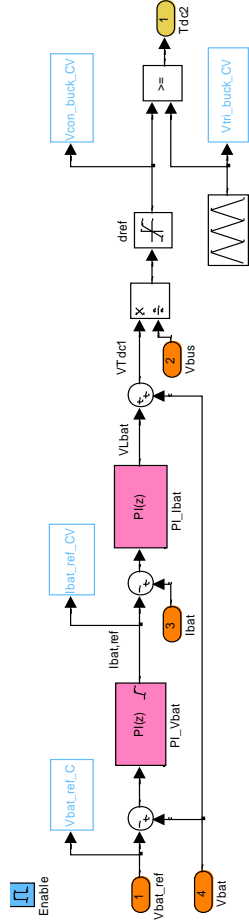




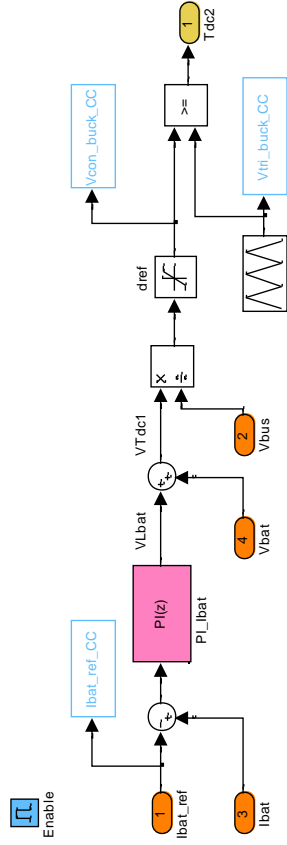
# CHARGING METHODOLOGY



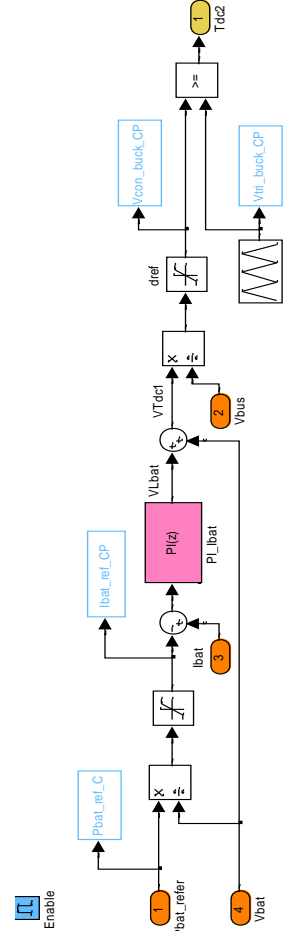
# CV CHARGING



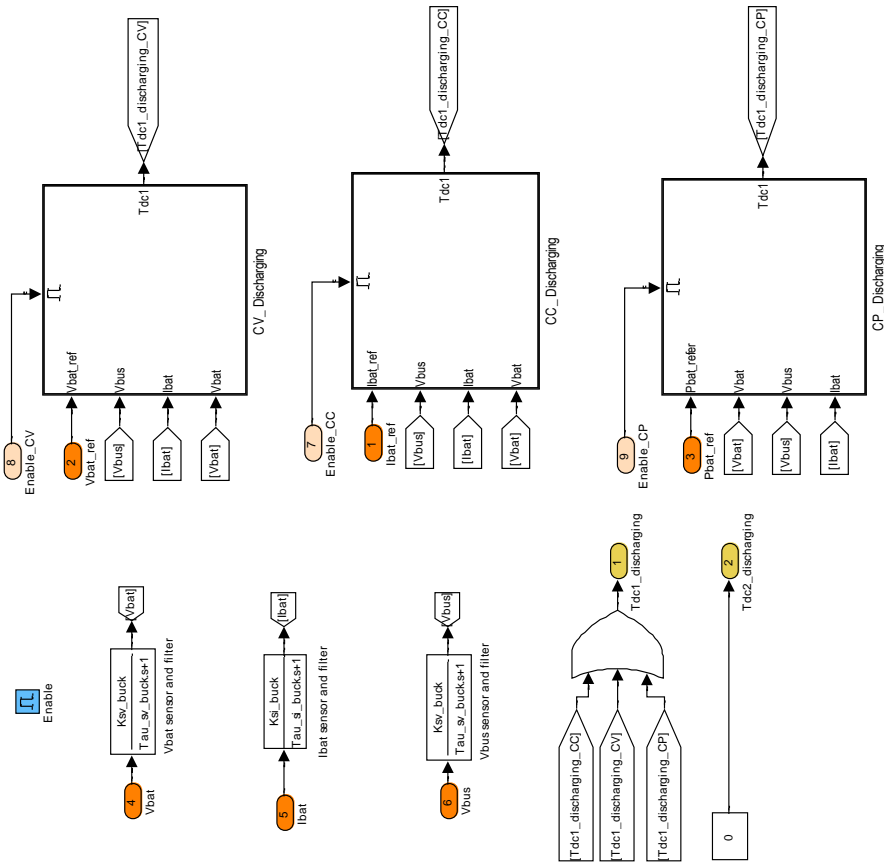
# CC CHARGING



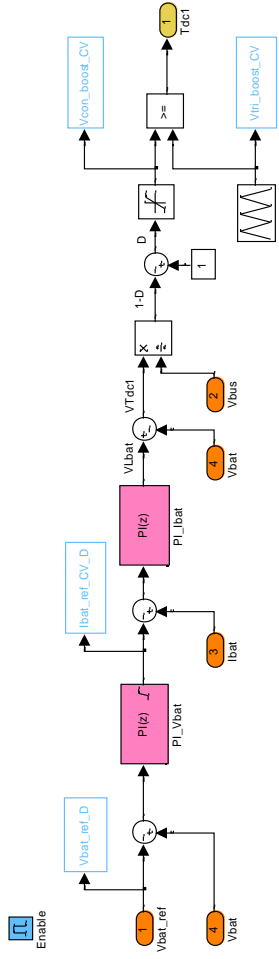
# CP CHARGING



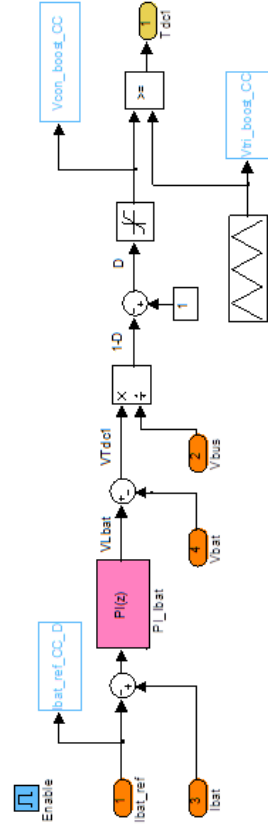
## DISCHARGING METHODOLOGY



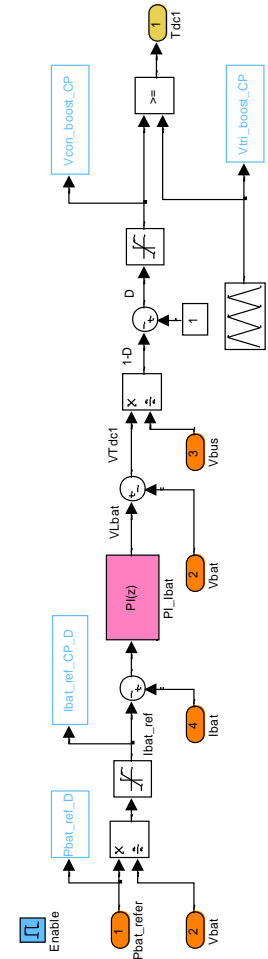
## CV DISCHARGING



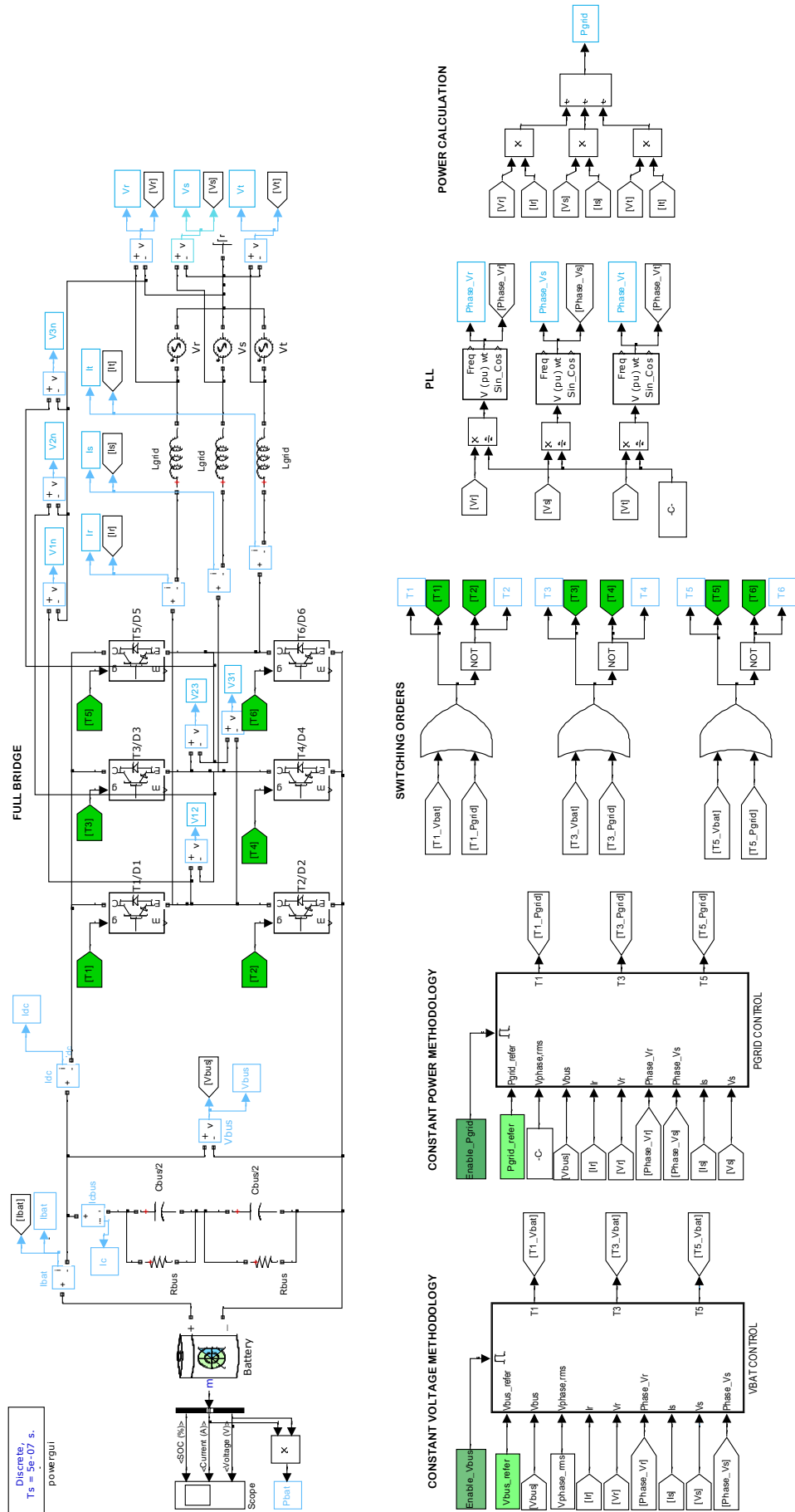
## CC DISCHARGING



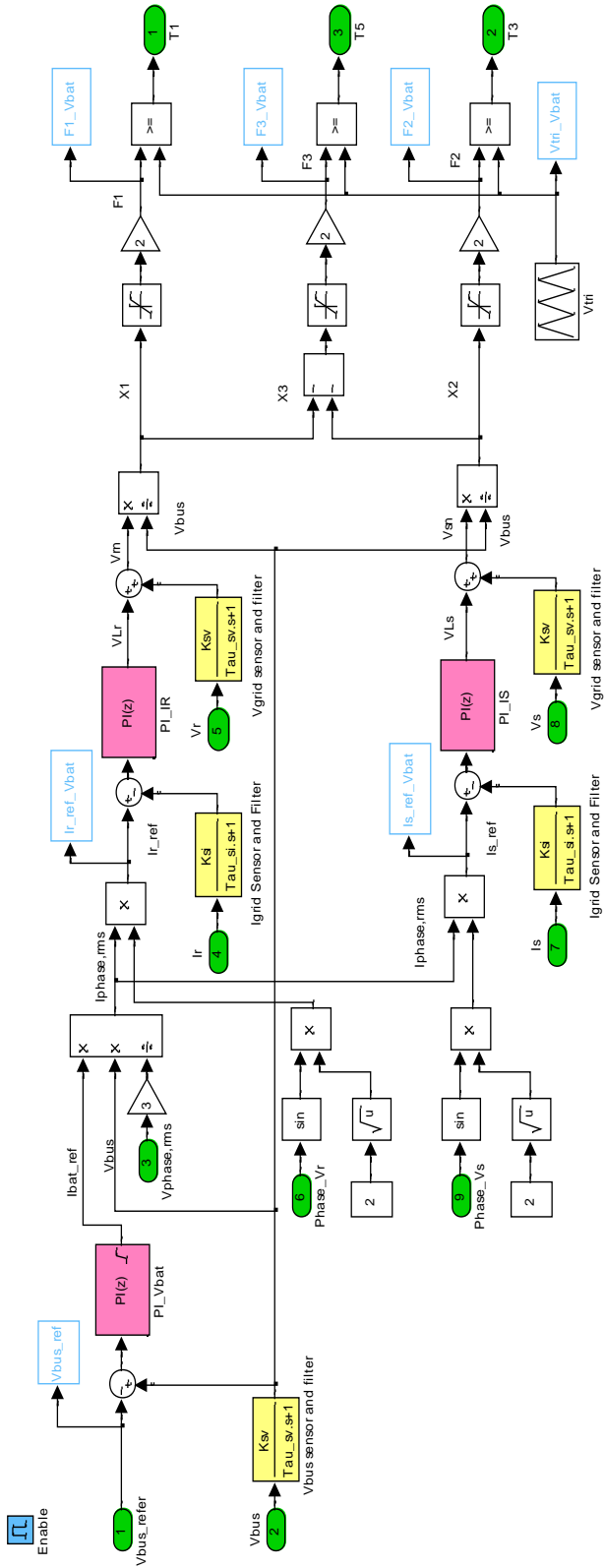
## CP DISCHARGING



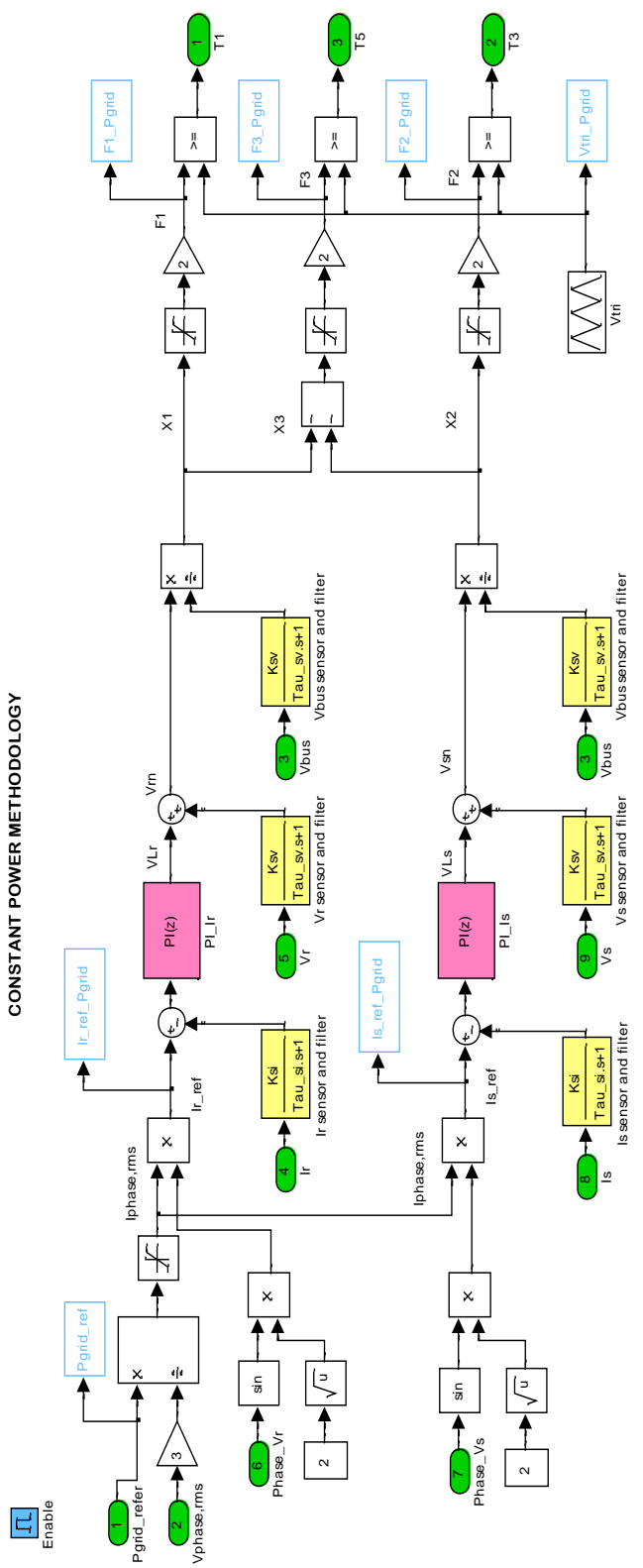
# Topology 3: Modeling of Full Bridge converter for High Power applications



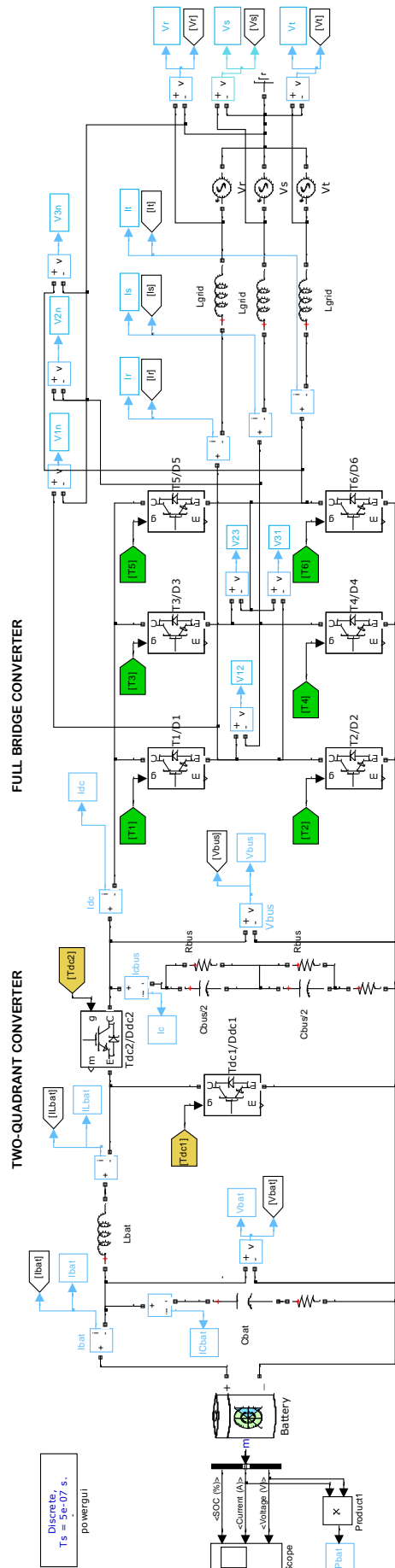
### CONSTANT VOLTAGE METHODOLOGY



### CONSTANT POWER METHODOLOGY

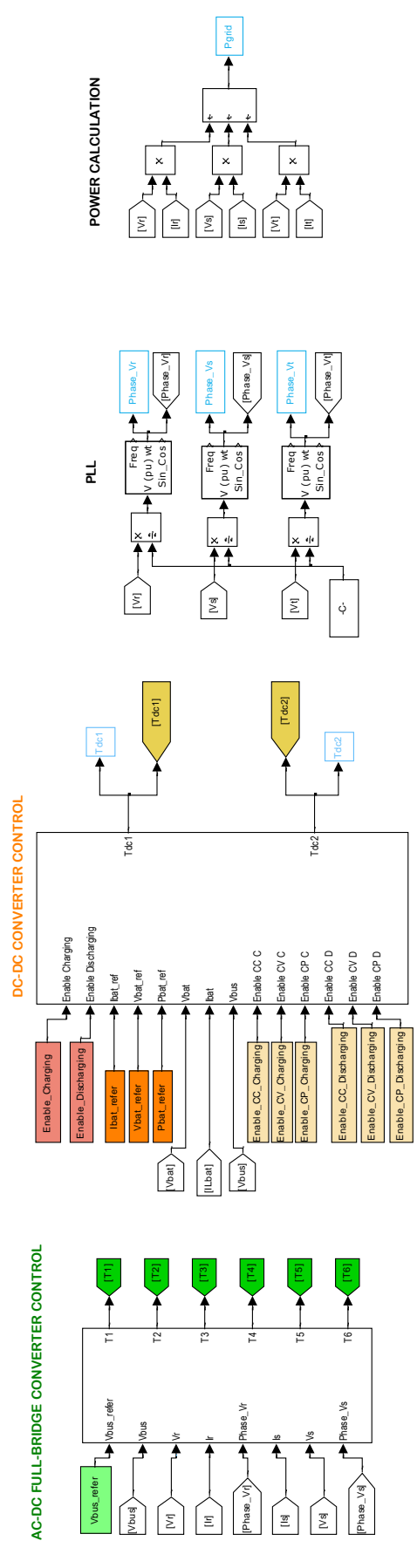


# Topology 4: Modeling of Full Bridge and DC/DC converter for High Power applications



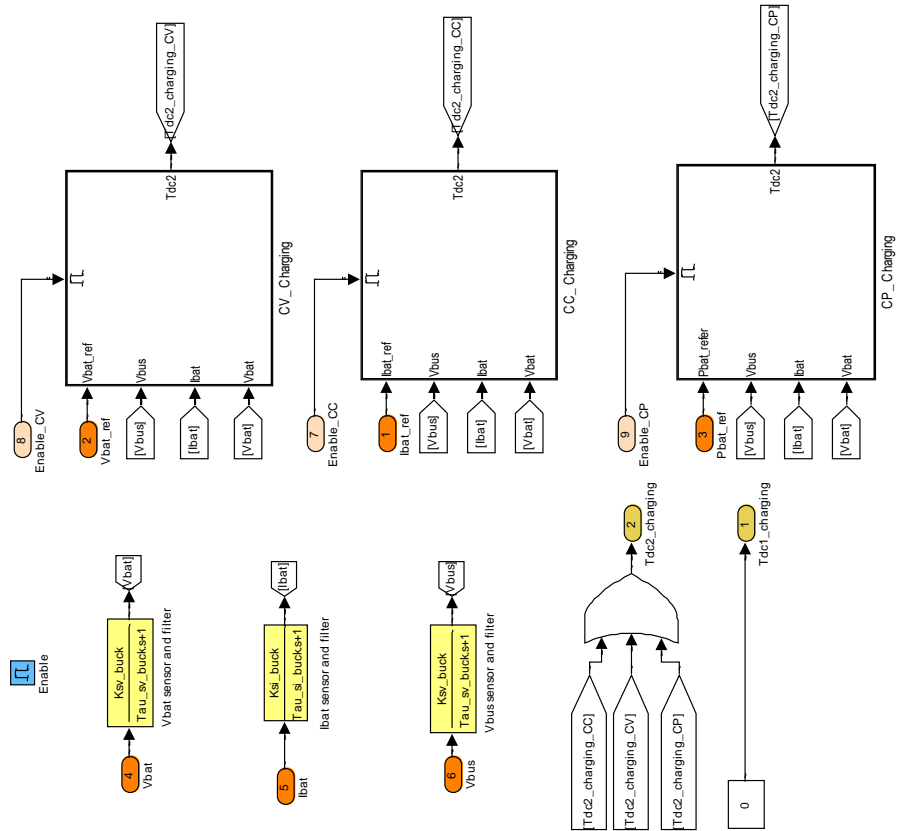
Discrete, Ts = 5e-07 s, powergui

Scope  
Product

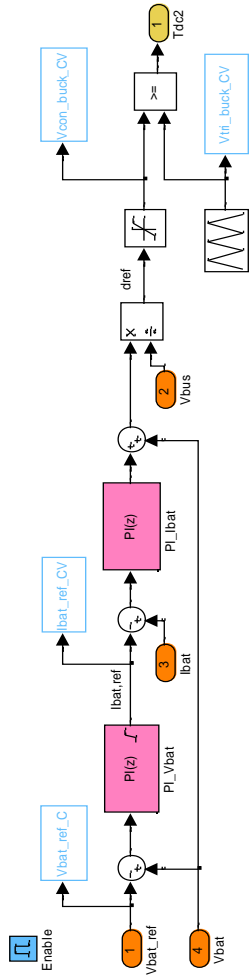




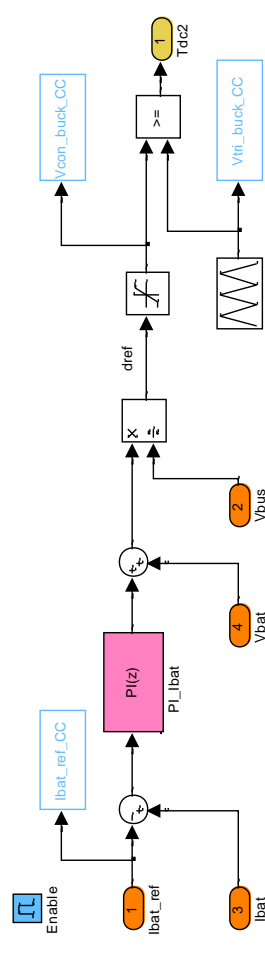
### CHARGING METHODOLOGY



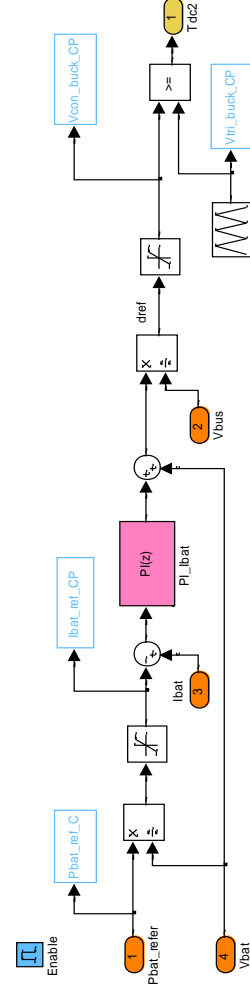
### CV CHARGING



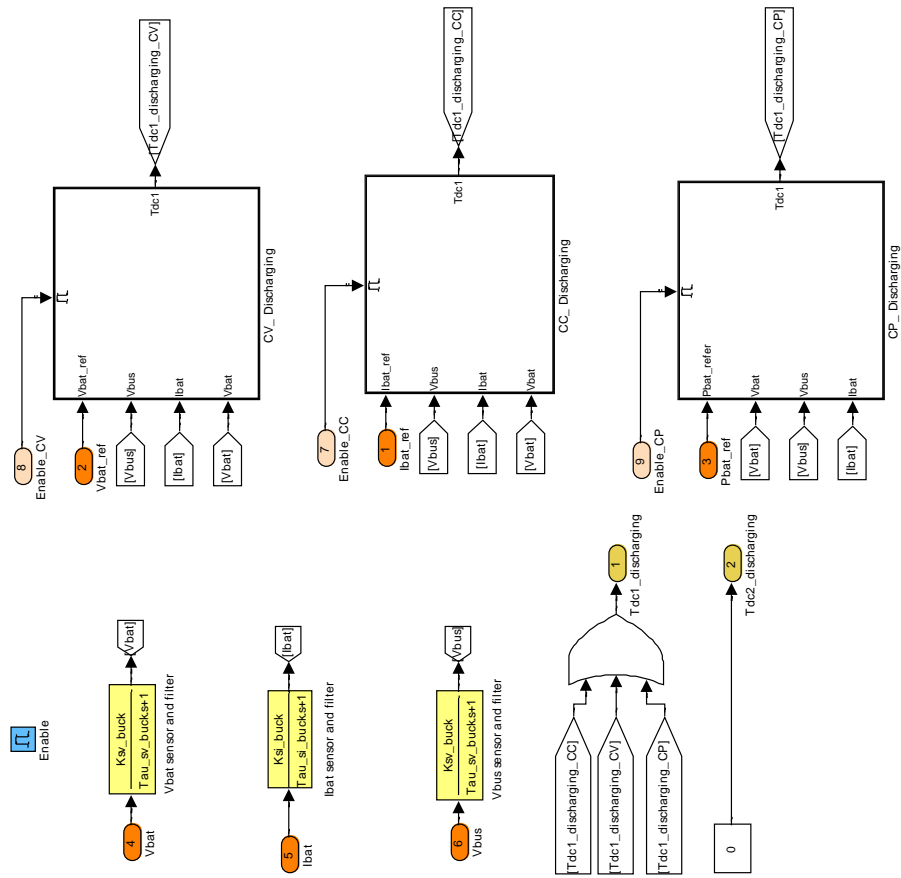
### CC CHARGING



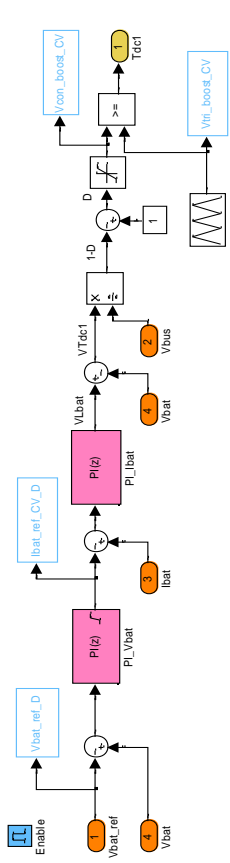
### CP CHARGING



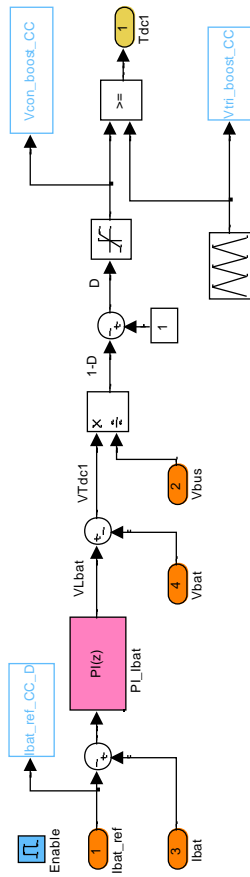
## DISCHARGING METHODOLOGY



## CV DISCHARGING



## CC DISCHARGING



## CP DISCHARGING

